Wave characteristics derived from video

Report

June, 2006

Z3757.00

WL | delft hydraulics

Wave characteristics derived from video

Carline Bos

Supervisors:
prof. dr. ir. M.J.F. Stive
prof. dr. ir. J.A. Roelvink
dr. ir. A.J.H.M. Reniers
dr. ir. S.G.J. Aarninkhof
ir. A.B. Cohen
ir. M.W.J. Smit

Report

June, 2006

Preface

The present M.Sc. thesis study forms the completion of my studies at the Delft University of Technology, faculty of Civil Engineering and Geosciences, Department of Hydraulic Engineering. This thesis study has been carried out at WL | Delft Hydraulics.

I would like to thank my supervising committee, prof. dr. ir. M.J.F. Stive (Delft University of Technology), prof. dr. ir. J.A. Roelvink (UNESCO-IHE and WL | Delft Hydraulics), dr. ir. A.J.H.M. Reniers (Delft University of Technology), dr. ir. S.G.J. Aarninkhof (WL | Delft Hydraulics), ir. A.B. Cohen (WL | Delft Hydraulics) and ir. M.W.J. Smit (Delft University of Technology) for sharing their knowledge and for their help and support during the realization of this thesis.

Furthermore I would like to thank Ap van Dongeren (WL | Delft Hydraulics) for his very useful lectures on wave theory and Robin Morelissen (WL | Delft Hydraulics) for helping me to understand Matlab and the Argus software. Besides I would like to thank Gerben Ruessink (Utrecht University) for the possibility to participate in the field experiment. I am grateful to WL | Delft Hydraulics for the opportunity and facilities they offered me for graduating at their institute. Moreover I would like to thank the other graduate students at WL | Delft Hydraulics for creating a pleasant atmosphere. They were often of great help and support and I enjoyed the funny breaks, lunches and trips we made together.

During these last months, but also throughout my whole study period, my parents and sister, friends and housemates were of great support. I would like to thank them all, but especially my parents who gave me the opportunity to study in Delft and supported me to make a great time of my student days.

Carline Bos

Delft, June 2006

Contents

List of Figures

List of Tables

List of Symbols

Roman symbols

a	moment of spectrum
b	moment of spectrum
c	celerity
cov	covariance
f	focal length
f	frequency
h	water depth
i	imaginary unit = √(-1)
k	wavenumber
m	moment of spectrum
n	step-size
p	pressure
t	time
u	horizontal image coordinate
u	horizontal velocity
v	vertical image coordinate
v	vertical velocity
x	horizontal cross-shore field coordinate
y	horizontal longs-shore field coordinate
z	vertical field coordinate
z	level
C	covariance
E	wave energy
E(X)	expected value of X
H	waveheigth
I	pixel intensity
L	linear function of camera orientation, position and focal length
L	wavelength
O	order
R	correlation coefficient
S	spectrum
T	wave period

Greek symbols

γ	correlatoin coefficient
δ	horizontal field of view

Greek symbols

η	elevation
θ	angle of wave incidence
μ	mean
π	pi = 3,1416
σ	camera roll
σ	standard deviation
τ	camera tilt
Δ	difference
φ	camera azimuth
ω	angular frequency

Subscripts

0	from offshore data
b	bathymetry
c	at camera location
g	group
gt	ground truth
max	maximum
mean	mean
n	number
p	peak
peak	peak
rms	root-mean-square
tide	tide
video	from a video image
x	cross-shore

Summary

Introduction

Collection of long-term data sets of wave characteristics and bathymetry with high resolution in time is a prerequisite to improve our understanding of nearshore coastal dynamics. Advanced video monitoring systems allow to sample these data automatically, on a long-term basis and without the need to deploy in situ instruments in a hostile environment. Recently, a technique was developed to derive wave frequency-direction spectra from time series of pixel intensities (Holman and Chickadel, 2004). A second technique (Stockdon and Holman, 2000) quantifies nearshore bathymetry from video-derived estimates of wave phase speed. Both techniques were successfully tested against field data collected at Duck (NC) and near San Diego (CA); their applicability for typical North Sea conditions as found along the Dutch coast is unknown yet.

The central aim of this work is to apply and assess the applicability of the existing methods to estimate wave characteristics from video imagery with data from the Dutch coast. To achieve this central aim, the Holman and Chickadel (2004) model is used to determine directional wave spectra at Egmond aan Zee (NL) and the accuracy of the results is assessed. Furthermore a new analysis technique is developed to determine wave phase speed and corresponding bathymetry from video using cross correlation analysis, as opposed to the spectral technique developed by Stockdon and Holman (2000). The work described here is part of the ONR funded BeachWizard project (Cohen et al, 2006), which aims at the nowcasting of bathymetrical evolution through assimilation of remote sensing data and model computations of nearshore coastal processes.

The analysis of wave direction, period and celerity from time stack images was performed with data collected at Egmond aan Zee along the Dutch coast. The field experiment was carried out from 20 September 2005 to 29 October 2005 in cooperation with the Utrecht University. During this field campaign data were simultaneously collected by video (half hourly time stack images) and in situ wave instruments in the intertidal zone. During the field campaign mostly mild wave conditions occurred and a complex, highly irregular beach morphology was noticed. The final dataset consists of 2.5 days of good quality time stacks at half hourly intervals and concurrent in situ measurements (water level, wave height, period and direction) at three locations, resulting in 43 time-series for ground-truthing. Wave data sampled from an offshore buoy at 21 m water depth are used for ground-truthing the deeper optical instruments (outside the intertidal area).

Wave period and direction

The pixel intensity time series $I(t, x, y)$ are processed using a Fourier transform followed by a maximum likelihood estimate, resulting in the spectrum $S(f, k, \theta)$. This spectrum is weighted over k^{-2} and integrated in wave number space to estimate at $S(f, \theta)$, supposing that intensity I is proportional to the wave slope. Omitting the weighting over k^{-2} assumes that the intensity is proportional to the surface elevation. As the North Sea wave conditions (broad wave spectrum) differ from the swell-dominated spectra usually found at Duck, the

resulting spectrum is not necessarily single-peaked, hence T_{peak} is not well defined. Therefore T_{m01} is calculated as the video-based indicator for wave period, using the energy density spectrum between 0.11 and 0.5 seconds. A filter is applied to consider only the high frequency part of the signal and ignore the low frequency noise. An example of the optical frequency spectra and in situ spectra for an instrument in the intertidal area is given in Figure 1-1.

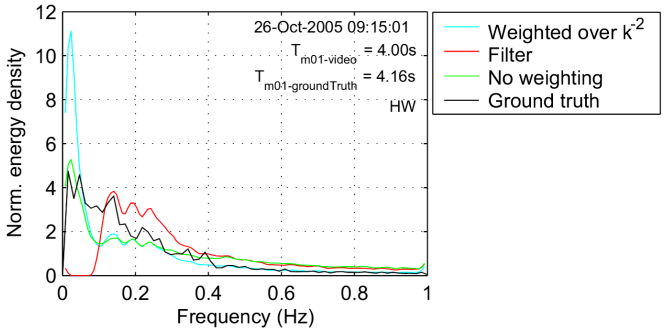

Figure 1-1 Comparison of optical (blue, red, green) and in situ (black) measured scaled frequency spectra. The blue and green lines represents respectively with and without normalization over k^2. For the red line a high pass filter is applied before normalization and integration over k.

The wave period is best estimated from video by T_{m01}, see Figure 1-2. The optical frequency spectrum using the method without weighting over k^{-2} shows the best correlation with the ground-truth data for data in the intertidal area. This means the intensity is proportional to the surface elevation. In the shoaling region further away from the camera the intensity corresponds to the slope of the waves and weighting over k^{-2} have to be applied to receive the best results. The correlation between optical and in situ estimates of wave period increases by only applying the high water data for the wave conditions encountered in this experiment. The wave direction shows a poor correlation which is at least partly attributed to the complex beach topography and limited dataset. A weighted mean wave direction from video best represents the measured wave direction in the field for the wave conditions encountered here.

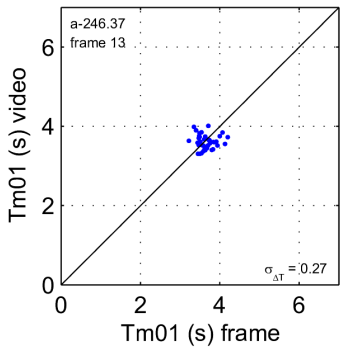

Figure 1-2 T_{mo1} from video plotted against in situ T_{mo1}. $\sigma_{\Delta T}$ represents the standard deviation of the difference between T_{video} and the mean T_{frame}.

Wave celerity and bathymetry

To determine wave celerities from time stacks images, cross shore arrays of pixel intensity time series are used. The original intensity signal from the stack is smoothed with a high-pass filter to remove low-frequency trends and subsequently a low-pass filter is applied to remove noise. The time lag from cross correlation of intensity time series is estimated in neighbouring pixels. Error bands (+/- standard deviation) are determined from recurrent estimates based on sub-sampling of the time stack. A mean of multiple estimates of the time lag using increasing values of the step-size between neighbouring pixels, weighted with the correlation, will give an estimate of the celerity. A running mean (filter with several meters cross-shore) was used to arrive at robust estimates of local bathymetry.

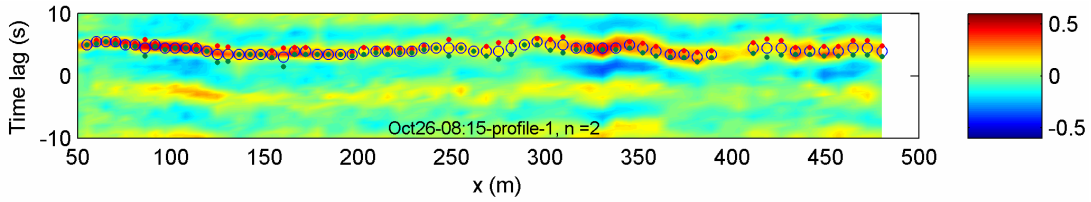

Figure 1-3 Time lag and correlation from cross-correlation between pixel intensity time series over a cross shore array from x=50 to x=500 m.

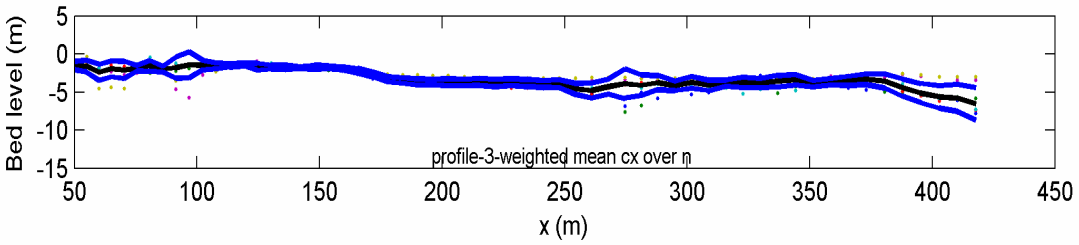

Figure 1-4 Bathymetry estimate Egmond aan Zee over a cross shore array from x=50 to x=500 m. Bed level (black) and standard deviation of bed level (blue), determined from celerity estimates resulting from 6 separate successive timestacks.

Cross correlation is also determined from the group signal in the filtered intensity time series. The filtered intensity signal is divided by its standard deviation to equalize the intensity of the signal over the whole length of the cross-shore array. The envelope of the time serie is derived by using a Hilbert transform and the resulting intensity signal is squared to correspond to the elevation. Strong correlation was found in the shoaling region and the surf zone. In the transition area the correlation is weaker because of the change in intensity signal from dark wavefront to light breaking wavefront. So far the underlying bathymetry cannot be derived from the group celerity despite of the correlation and time lags determined between the envelope of pixel intensity time series.

1 Introduction

1.1 General

The nearshore coastal zone is generally a wave dominated environment. This zone is the dynamic region of the coastal environment where ocean waves interact with local morphology. Due to the dense population in this area, the coastal zone is of great societal importance. Therefore the coastal zone has attracted significant research interest. It is of great importance to scientists and managers to quantify wave characteristics and nearshore bathymetry. The nearshore zone is a morphologically dynamic area as can be seen by the eroding and accreting shorelines. The increased development along the coastal zone and the problems of erosion ask for knowledge of how the nearshore system behaves. The dynamics of the nearshore processes are determined by the fluid motions and the sediment response.

Wave measurements and bathymetric data are basic elements for understanding the fluid dynamics and the interactions between fluid dynamics and bathymetry. Collection of long-term data sets of wave characteristics and bathymetry is an important requirement for the improvement of the nearshore science. With the help of images from video cameras wave characteristics and bathymetric data can be collected automatically, regularly and on a long-term basis. With the use of these remote sensing techniques, data can be collected not involving instruments into the hostile environment of the surf zone, allowing sampling at any time.

1.2 Objectives

Recently, a technique has been developed that uses pixel intensity time series to obtain wave characteristics. This technique is one of the applications of a broader used video remote sensing programme, named Argus (Holman et al., 1993). The Argus Video program is developed at the Coastal Imaging Lab, Oregon State University. Lately, in this program more attention is paid to derive wave characteristics from video. In this framework a technique is developed to derive frequency-direction spectra from time series of pixel intensities (Holman and Chickadel, 2004). This theory is already successfully applied during the NCEX experiment in Southern California, USA. Also a technique is developed to derive wave phase speed and nearshore bathymetry from video imagery and applied at Duck, North Carolina, USA (Stockdon and Holman, 2000).

To test genericity, the theories to estimate wave characteristics from video imagery that have been applied to the coast of the USA need application to the Dutch coast. Field data from a field experiment in Egmond aan Zee will be used to compare the time series from tripod mini frames in one point (ground truth data) to the time series of pixel intensities (time stacks) in the same point.

The central aim of this project is to apply, and assess applicability, of two different theories to estimate wave characteristics from video imagery with data from the Dutch coast. To achieve this central aim, two main objectives are formulated:

1. Apply an existing technique (Holman and Chickadel, 2004) to determine the directional wave spectrum from video to a dataset from Egmond aan Zee (NL), and asses accuracy of the results for this dataset.

2. develop analysis techniques to determine wave phase speed and corresponding bathymetry from video using cross correlation analysis as opposed to the spectral technique devolped by Stockdon and Holman (2000).

The work described here is part of the ONR funded BeachWizard project (Cohen et al, 2006), which aims at the nowcasting of bathymetrical evolution through assimilation of remote sensing data and model computations of nearshore processes.

1.3 Outline

In this introductory Chapter 1, background information is given that motivates the present research and the resulting objectives of the research are explained. Chapter 2 describes the Argus video technique and the video data types used in this work. Instead of using pressure sensors, pixels from video imagery are implemented as sensor elements and the signals are variations of optical intensity from each of the pixels. In Chapter 3 the nearshore wave theory will be explained shortly and standard equations applied in this research are given. The next section, Chapter 4 focuses on the field experiments in Egmond aan Zee that have been carried out in the framework of this research and compares optical with in situ measurements. Information is given about the site and the measuring techniques used to obtain data and a data selection is made. Finally, the data set is discussed. The model that will be used to determine the directional spectrum from optical arrays is described in Chapter 5. The wave period and direction are determined from the spectra and comparison is made with ground truth data. The analysis technique to determine wave celerity using cross-correlation is discussed in Chapter 6. The accuracy of different approaches to calculate celerity is determined and an estimation of the corresponding bathymetry is given. A discussion on the utility and applicability of the techniques is presented in Chapter 7. The last chapter of this thesis reports the conclusions that can be drawn of the application and applicability of estimating wave characteristics from video data along the Dutch coast. Finally, recommendations are given on which further research can be concentrated.

2 The Argus video technique

2.1 Introduction

The Argus video technique is developed specifically for purposes of basic research in the nearshore. The Argus program is developed under the guidance of Prof. R. Holman of Oregon State University (USA). Video based monitoring stations are being placed at important sides around the world, presently more than 30. Unmanned, automated video stations guarantee the collection of video data at sites of scientific interest. An Argus video monitoring system generally consists of four to five video cameras, spanning a 180° field of view and allowing a full coverage of about four to six kilometres of beach. The cameras are mounted on a high location along the coast. Video data are collected during daylight, usually hourly, although any schedule can be specified. The video data are temporarily stored on a computer on site, which communicates to the outside world by broadband internet.

2.2 General Argus conventions

At every Argus site, the orientation of the x-axis is shore normal, with the positive x-axis pointing in seaward direction. The y-axis is directed perpendicular to the x-axis, such that the co-ordinate system thus obtained is positive in mathematical sense (Figure 2-1). The latter means that the rotation from the x-axis towards the y-axis indicates the counter-clockwise turning direction. The vertical reference level ($z = 0$) is generally set to match the mean tidal level or a commonly used (often national) ordinance level (like NAP in the Netherlands). All Argus processing is performed in GMT times.

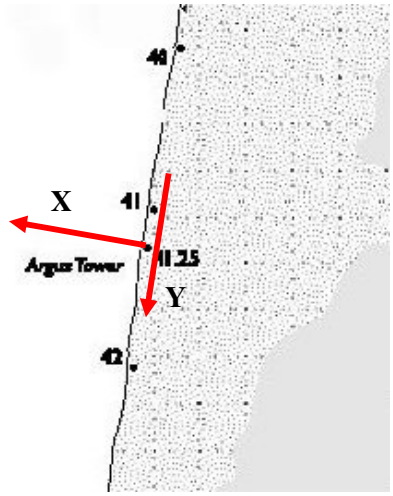

Figure 2-1 Argus co-ordinate system at Egmond aan Zee, Coast3D tower

2.3 Image processing

Quantification of the information contained in a video image requires the conversion of image coordinates (*u, v*) to the corresponding real world location (*x, y, z*). The relation between image and real world coordinates is defined by means of camera location (x_c, y_c, z_c), the camera orientation and the effective focal length *f* which directly relates to the camera horizontal field of view δ. The camera orientation is defined through three camera angles, namely the tilt τ, azimuth ϕ and roll σ (Figure 2-2). The angles τ, ϕ and σ represent the rotation with respect to the vertical *z*-axis, the orientation in the horizontal *xy*-plane and the rotation of the focal plane with respect to the horizon. Standard photogrammetric procedures enable the transformation of field (*x, y, z*) to image coordinates (*u, v*), expressed by means of the collinearity equations:

$$u = \frac{L_1 x + L_2 y + L_3 z + L_4}{L_9 x + L_{10} y + L_{11} z + 1} \tag{2.1}$$

and

$$v = \frac{L_5 x + L_6 y + L_7 z + L_8}{L_9 x + L_{10} y + L_{11} z + 1} \tag{2.2}$$

The coefficients L1 to L11 are linear functions of the seven unknowns in camera orientation (τ, ϕ, σ), camera location (x_c, y_c, z_c) and focal length *f* (see Appendix A). The inverse transformation from image to field coordinates results in two equations with three unknowns (*x, y, z*). The *z*-coordinates in this transformation are assumed to match a certain horizontal reference level or the tidal water level.

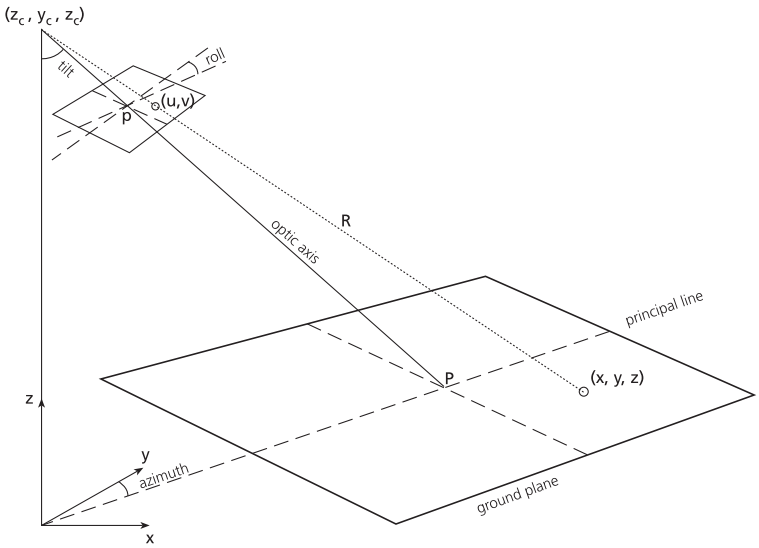

Figure 2-2 Relation between image (*u, v*) coordinates and real world coordinates (*x, y, z*).

2.4 Standard image types

Each standard hourly collection usually consists of three types of images (see Figure 2-3, Figure 2-4 and Figure 2-5), i.e. a snapshot, time exposure and variance image. A snapshot image serves as simple documentation of the ambient conditions but offers little quantitative information. Every daytime hour, snapshot images are collected and averaged over a period of 10 minutes, yielding time-exposure images. These time exposure images average out natural modulations in wave breaking to reveal a smooth pattern of bright image intensities which are a proxy for the underlying, submerged sand bar topography. Time exposure images also 'remove' moving objects such as ships, vehicles and people from the camera field of view. Variance images display the variance of the light intensity signal during the same ten minutes of time exposure. Variance images help identify regions which are changing in time (like the sea surface) from those which may be bright but are unchanging (like the dry beach). Merged images can be obtained by rectification of simultaneously collected images from all cameras, giving plan view or panoramic images of the nearshore.

Figure 2-3 Snapshot image at Egmond aan Zee

Figure 2-4 Time exposure image at Egmond aan Zee

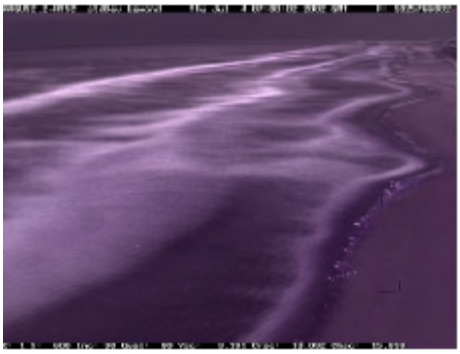

Figure 2-5 Variance image at Egmond aan Zee

2.5 Timestacks

Besides snap shots and time averaged video data, data sampling schemes can be designed such to collect time series of pixel intensities, typically at 2 Hz. As an example, Figure 2-6 show the strong correlation which is commonly observed between a time series of pixel intensities and the wave height signal obtained from a wave gauge at the same location (Lippmann and Holman, 1991). From this pixel intensity time series, wave and flow characteristics can be derived. Time series of pixel intensities can be sampled along a cross-

shore or alongshore array. The resulting data collection, $I(t, x, y)$ yields a time stack image (see Figure 2-7). Due to the digitalisation process, the intensity data are normalised over the lens's intensity range and thus dimensionless.

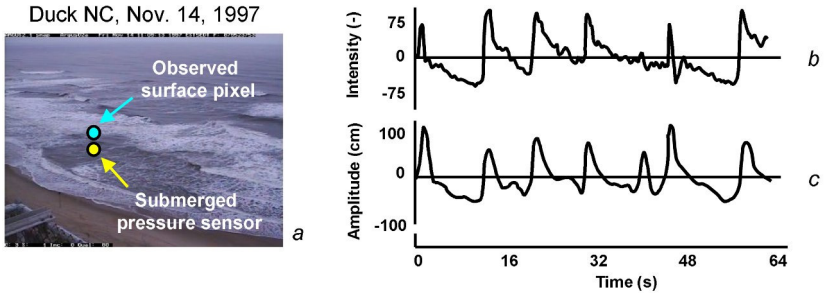

Figure 2-6 Relation between time series of pixel intensities and a wave height measured by a pressure sensor sampled from Duck, USA (after Lippmann and Holman, 1991).

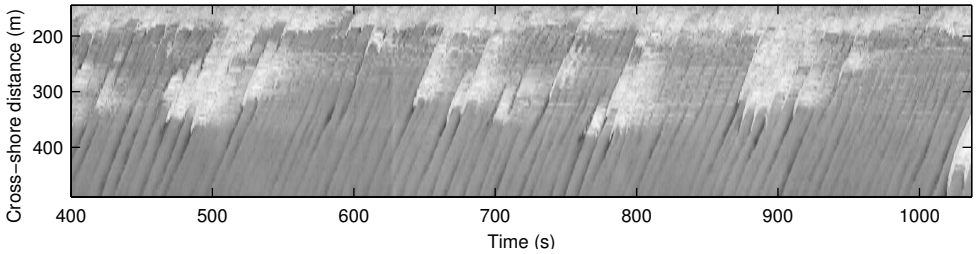

Figure 2-7 Example of a time stack image sampled along a cross-shore array at Duck, USA. The cross-shore axis is positive off-shore. The dark bands represent the non-breaking wave fronts and the white bands reflect the foam of the breaking waves.

Pixel instruments can be used to measure a range of nearshore variables. In Table 2-1 the pixel instruments are listed including the number of pixels needed for each. The alpha and bathy instruments are used in this research.

Table 2-1 Pixel instruments

Pixel instrument	**Variable of Interest**	**Number of Pixels**
single pixel	wave period	1
alpha array	wave angle, wave directional spectrum	17
tess array	wave angle field, field of wave directional spectra	O (1000) sampling area dependent
bathy array	bathymetry	O (100) for single transect
runup array	wave runup	O (100)
vbar	longshore current	O (100)

Alpha arrays (Appendix B.2) are small 2D groups of pixels designed to allow estimation of peak wave direction or, preferably full directional wave spectra. Bathy arrays consist of cross-shore arrays of several locations at which the pixel intensity time series are collected.

From these time series the shoreward propagation of waves can be measured through spectral or cross-correlation techniques resulting in an estimation of the nearshore bathymetry through linear theory.

The basic assumption of the optical measurement of directional spectra is that optical radiance from the ocean surface is representative of the sea surface. This optical radiance can be analyzed in the same ways as other wave measurements but without the logistic complexity of in situ sensors. Consequently the basic variable of interest is the optical intensity $I(x, y, t)$, measured with a camera.

Variations in sea surface slope due to waves cause reflection from different elevations in the sky, making the wave visible owing to the sky gradient (the variation of sky brightness from very bright near the horizon to darker near the zenith (Lynch and Livingston, 1995). Thus seaward the face of the wave (away from a land-based camera) is usually light, while the landward, front face is dark. The angle of view relative to wave rays also determines how strong the visible signal will be. For example, if one were to look along a wave crest, there will be no sea surface slope component in the direction of view; therefore the wave would not be discernable. Once waves begin to break, individual wave crests can be recognized by diffuse reflection from the white foam associated with the turbulence from breaking.

3 Nearshore wave theory

3.1 Introduction

Waves are nothing but disturbances of the equilibrium state in any given body of material, which propagate through that body over distances and times much larger than the characteristic wavelengths and periods of the disturbances. Water waves are characterized by their height H, their celerity c, their length L, and their period T (Figure 3-1). The wave height is the distance between the trough (lowest part) and crest (highest part) of the wave. The wave length is the distance between two successive wave crests. The wave period is the time for two consecutive crests to pass a fixed point. Shoaling and refraction of waves occur when the waves are in shallow water. If the water depth is less than half the wave length, then the wave is considered to be in shallow water. When the waves move into shallow water, they begin feel the bottom of the ocean.

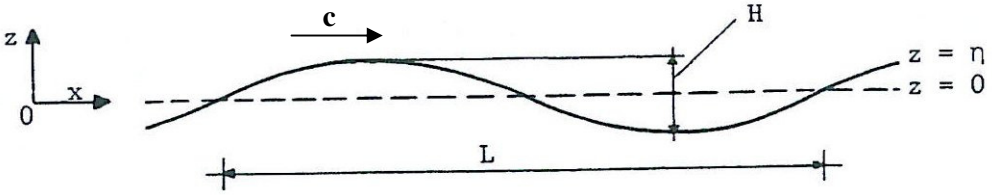

Figure 3-1 Defenition of regular wave including waveheight H, wavelength L and elevation η.

Shoaling occurs as the waves enter shallower water. The group wave speed and wave length decrease in shallow water, therefore the energy per unit area of the wave has to increase, so the wave height increases. The wave period remains the same during shoaling. When the wave crest becomes too steep, it becomes unstable, curls forward and breaks. This usually happens when the height of the wave becomes about the same size as the local water depth. Figure 3-2 shows the progression of a wave as it comes towards the shore indicating the shoaling region, transition area and surf zone.

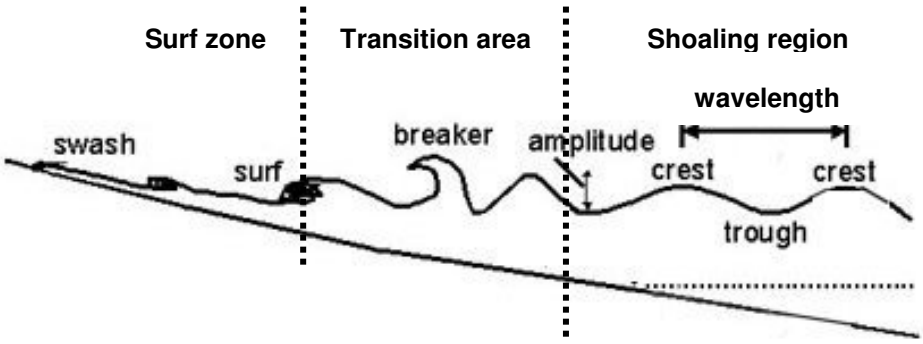

Figure 3-2 Wave propagating to the shore

Refraction is the bending of waves because of varying water depths underneath. The part of a wave in shallow water moves slower than the part of a wave in deeper water. So when the depth under a wave crest varies along the crest, the wave bends. An example of refraction is when waves approach a straight shoreline at an angle. The part of the wave crest closer to shore is in shallower water and moving slower than the part away from the shore in deeper water. The wave crest in deeper water catches up so that the wave crest tends to become parallel to the shore.

Diffraction usually happens when waves encounter surface-piercing obstacle, such as a breakwater or an island. It would seem that on the lee side of an island, the water would be perfectly calm; however it is not. The waves, after passing the island, turn into the region behind the island and carry wave energy and the wave crest into this so-called 'shadow zone'. The turning of the waves into the sheltered region is due to the changes in wave height (say along the crest) in the same wave. If the sides of the island are sloping under the water, then refraction would also be present.

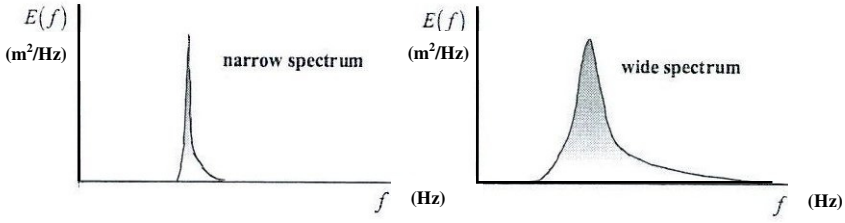

Figure 3-3 Energy density spectrum

The wave spectrum is based on the notion that the surface profile of ocean waves can be seen as the superposition of very many propagating harmonic waves, each with its own frequency, amplitude, wave length, direction and phase. The wave characteristics are represented by the wave spectrum. An example of a narrow and wide energy density spectrum is shown in Figure 3-3.

3.2 Wave characteristics

In this section the wave characteristics wave period, wave direction and wave celerity will be described. The sea characteristics are determined by the variance density spectrum *E(f)* of the waves. The one-dimensional frequency spectrum *E(f)* can be obtained from the frequency-direction spectrum *E(f,θ)* (see Figure 3-4) by integration over all directions (per frequency)

$$E(f) = \int E(f,\theta)d\theta \tag{3.1}$$

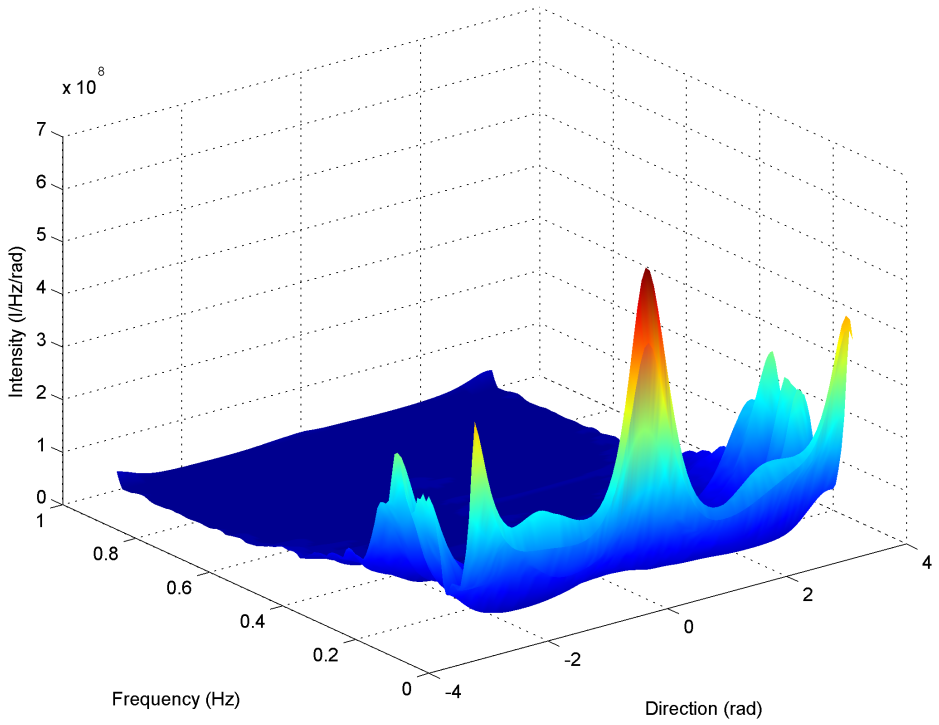

Figure 3-4 Frequency-directional spectrum at Egmond aan Zee, intertidal beach, 26 October 2005 8:15 Hrs

3.2.1 Wave period

The wave period can be computed from the spectrum *E(f)* in several ways. The peak period can be determined from the inverse of the frequency with maximum energy density.

$$T_p = f_p^{-1} \tag{3.2}$$

The wave characteristics can also be expressed in terms of the moments of the spectrum, which are defined as:

$$m_n = \int f^n E(f) df \quad \text{for} \quad n = 0,1,2,3.... \tag{3.3}$$

A characteristic wave period is the average period between consecutive zero-crossings:

$$T_{m_{02}} = \sqrt{\frac{m_0}{m_2}} \tag{3.4}$$

where m_2 represents the second-order moment of the spectrum.

The values of higher order moments are rather sensitive to noise in the high-frequency range of the spectrum. The reason is that in the computation of higher-order moments, the spectral

levels of higher frequencies, where noise is usually relatively large, are enhanced far more than the spectral levels of the lower frequencies. These considerations suggest that T_{m02} is not always the most reliably estimated characteristic wave period. Another mean period is therefore sometimes used, which is less dependent on high-frequency noise. It is defined as the inverse of the mean frequency of the wave spectrum (based on the first-order moment of the spectrum rather than the second-order moment). This results in

$$T_{m_{01}} = \frac{m_0}{m_1} \tag{3.5}$$

where the variables m_0 and m_1 represents the zero-th and first-order moment respectively of the wave spectrum.

3.2.2 Wave direction

The cross spectra of a collocated pressure sensor and bidirectional current meter yield low-resolution directional wave information equivalent to that obtained from measurements of commonly used surface-following heave-pitch-roll buoys (Longuet-Higgins et al., 1963). The normalized cospectra of pressure p, and the horizontal (x, y) velocity components u and v yield the lowest four Fourier moments of the directional distribution of wave energy $S(\theta) = E(f,\theta)/E(f)$.

The method of Kuik (1988) is used to calculate the angle depending on frequency. The input in this method is the wave spectrum in frequency directional domain. This results in a mean propagation direction depending on the frequency described by

$$\theta_0(f) = arc\tan\frac{b_1}{a_1} \tag{3.6}$$

and is defined in terms of the first-order moments a_1 and b_1 which are given below:

$$a_1(f) = \int \cos\theta S(\theta; f) d\theta = \frac{C_{pu}(f)}{\left\{C_{pp}(f)\left[C_{uu}(f) + C_{vv}(f)\right]\right\}^{1/2}} \tag{3.7}$$

$$b_1(f) = \int \sin\theta S(\theta; f) d\theta = \frac{C_{pv}(f)}{\left\{C_{pp}(f)\left[C_{uu}(f) + C_{vv}(f)\right]\right\}^{1/2}} \tag{3.8}$$

The mean angle can be calculated with two methods. The first method (as used in Swan) can be applied to determine the mean direction

$$\overline{\theta_{mean}} = mean(\theta_0(f)) \tag{3.9}$$

where $\theta_0(f)$ represents the mean propagation direction depending on frequency, Eq. (3.6).

Secondly the weighted mean can be calculated.

$$\overline{\theta_{weighted}} = \frac{\int E_f \theta_0 df}{\int E_f df} \tag{3.10}$$

The weighted mean reflects the mean propagation direction depending on frequency weighted by the energy density of that frequency instead of just averaging over the frequencies as in Eq. (3.9).

The peak wave direction is determined from the peak wave frequency in the spectrum

$$\theta_p = \theta(f_p) \tag{3.11}$$

A directional distribution can also be calculated from pressure and horizontal and vertical velocity components. Therefore the maximum entropy of Krogstad (1986) has to be applied, including the first order moments stated in Eq. (3.7) and (3.8) and the second order moments described by:

$$a_2 = \frac{C_{uu} - C_{vv}}{C_{uu} + C_{vv}} \tag{3.12}$$

$$b_2 = \frac{2C_{uv}}{C_{uu} + C_{vv}} \tag{3.13}$$

3.2.3 Wave celerity

Knowing the timelag belonging to the maximum cross-correlation (Eq. (3.22)) between two time series in two neighbouring points, the celerity in *x*-direction along a cross-shore array can be calculated applying

$$c_x = \frac{\Delta x_{ij}}{lag_{\max}} \tag{3.14}$$

where Δx is the distance between points *i* and *j* and the $lag_{\max}$ represents the time lag belonging to the maximum correlation between points *i* and *j*.

Snel's law can be applied to determine the celerity in the direction of θ.

$$\sin\theta = c\frac{\sin\theta_0}{c_0} \tag{3.15}$$

where θ_0 represents the offshore angle of incidence, c_0 the offshore celerity, c the celerity at depth h and θ the angle of incidence at depth h. Employing the celerity in *x*-direction by Eq. (3.14) and θ results in:

$$c = c_x \cdot \cos\theta \tag{3.16}$$

The group celerity, that is the celerity with which a group of waves is propagating, can be determined by

$$c_g = \frac{1}{2} \cdot \left(1 + \frac{2kh}{\sinh(2kh)} \right) \frac{\omega}{k} \tag{3.17}$$

where k represents the wavenumber, h the waterdepth and ω the angular frequency.

3.2.4 Linear dispersion relation

When the wave phase speed on a specific cross-shore array is known, the underlying bathymetry can be determined through linear theory. An estimate of the waterdepth will be defined using the linear dispersion relation

$$h = \frac{1}{k} arc\tanh\left(\frac{\omega^2}{gk} \right) \tag{3.18}$$

where g is the acceleration of gravity, ω the angular frequency determined applying the waveperiod T

$$\omega = \frac{2 \cdot \pi}{T} \tag{3.19}$$

and k the wavenumber solved from the relation

$$k = \frac{\omega}{c} \tag{3.20}$$

where c represents the celerity.

3.3 Cross-correlation analysis

The covariance between points i and j is determined using

$$\mathrm{cov}(x_i, x_j) = \left[\left(x_i - \mu_i \right) \left(x_j - \mu_j \right) \right]_t \tag{3.21}$$

where μ_i represents the mean of x_i and t the averaging over time. Subsequently the cross-correlation between points i and j is determined by

$$cor(x_i, x_j) = \frac{\mathrm{cov}(x_i, x_j)}{\sigma_i \sigma_j} \tag{3.22}$$

where σ_i, σ_j are the standard deviation of x_i, x_j.

3.4 Quality values

To quantify the quality of a parameter estimate, three quality values are calculated. The difference between a video-derived parameter and an in situ parameter (for example the wave period) is given by

$$\Delta T = T_{video} - T_{groundTruth} \tag{3.23}$$

and the root-mean-square error of this difference averaged over time

$$\Delta T_{rms} = \sqrt{\overline{(\Delta T)^2}} \tag{3.24}$$

The following equation represents the standard deviation of the difference between the video-derived parameter and the in situ parameter:

$$\sigma_{\Delta T} = \left(\frac{1}{n} \sum_{i=1}^{n} \left(\Delta T_i - \Delta T_{mean} \right)^2 \right)^{\frac{1}{2}} \tag{3.25}$$

where ΔT_{mean} equals:

$$\Delta T_{mean} = \frac{1}{n} \sum_{i=1}^{n} \Delta T_i \tag{3.26}$$

The correlation coefficient between a video-derived parameter and an in situ derived parameter is stated in the following equation

$$R_{T_{video}, T_{groundTruth}} = \frac{C(T_{video}, T_{groundTruth})}{\sqrt{C(T_{video}, T_{video}) \cdot C(T_{groundTruth}, T_{groundTruth})}} \tag{3.27}$$

where the C is described by

$$C_{video, groundTruth} = E((T_{video} - \mu_{T_{video}})(T_{groundTruth} - \mu_{T_{groundTruth}})) \tag{3.28}$$

and *E* represents the expected value of the parameters between brackets.

4 Data

4.1 Introduction

The analysis of wave direction, period and celerity from time stack images was performed with data collected along the Dutch coast. For this research project data will be used from a field experiment at Egmond aan Zee, from 20 September 2005 to 29 October 2005 (Figure 4-1). The experiment was carried out just north of the Argus Coast3D tower, in cooperation with students from Utrecht University.

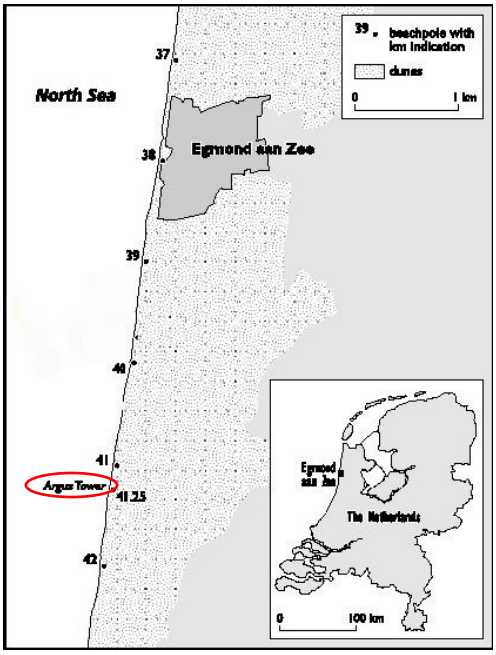

Figure 4-1 Map of the Egmond field site

4.2 Site information

The Egmond Coast

The coastal zone of the Netherlands is often divided into three major regions, namely the Delta area, the Wadden area and the Holland coast. These regions differ in morphological appearance and in the dominance of related physical processes. Egmond aan Zee is located on the Holland Coast, in between the harbour of IJmuiden and the Hondsbossche Seadyke. The Holland coast is de central part of the Dutch coast. This coastal stretch is about 120 km long and mainly consists of sandy beaches and multiple barred nearshore zones. The orientation of the coastline is approximately north-south (10°-190°).

Geomorphology and sediment characteristics

The shoreface of the Egmond coast has a slope of 1:170 and a transition to the North Sea bottom at -15 m NAP (NAP is Dutch Ordnance Level, 0 m NAP is about mean sea level). The nearshore at Egmond is characterised by a double subtidal bar system (Figure 4-2). The crest of the outer bar is almost straight and lies at a level of -3.5 to -4.0 NAP. The crest of the inner nearshore bar has an irregular alongshore plan view and lies below a mean bed level of -1.5 to -2.5 m NAP. Sometimes rips appear in the inner nearshore bar. The cross-shore bar crest spacing is fairly constant in time at about 300 m (Van Rijn et al, 2002).

The beach at Egmond aan Zee has a width of 100 to 200 m from the dune foot to the low water line and has an average slope between 1:35 and 1:60. The morphology of the beach is often characterised by a swash bar. This intertidal bar is generated during low to moderate wave-energy conditions and disappears during high wave-energy conditions.

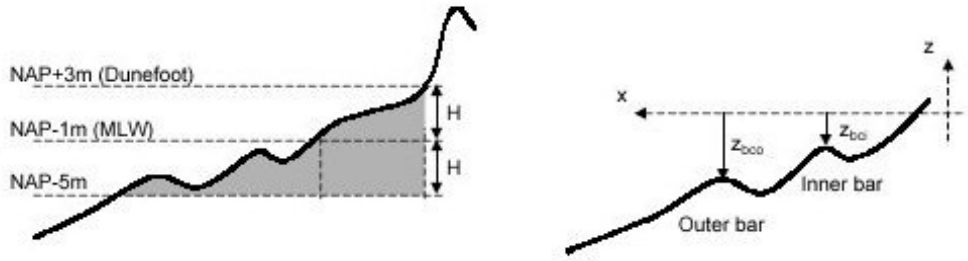

Figure 4-2 The bar system along in the nearshore zone along the Dutch coast.

The sediments at the field experiment site are composed of fine to medium sand with a mean grain size between 250 and 350 μm. There is a coarsening of the sediment from deep water to the intertidal beach and a fining of the sediment from the intertidal beach to the dunes.

Wind and waves

On the Holland coast both wind waves and tides have an effect on the sandy sediments inducing the morphological responses. Most of the winds along the Holland coast come from the North Sea. The prevailing wind direction is southwest (23%), followed by west (16%), east (13%) and northwest (12%). The storm winds coming from northwest cause the largest wind set-up. The seasonal variation in the wind climate is clearly reflected in the wave climate. The yearly mean wave height H_{m0} is about 1.2 m and the yearly mean centroidal wave period T_{m01} is about 5 s. In the stormy winter months (November to January) the monthly mean wave height is about 1.7 m while in the summer months (April to August) the mean monthly wave height is just about 1 m.

Tide

During the flood period the tidal currents in front of the Holland coast are northward directed. During the ebb period these currents are southward directed. The semi-diurnal tidal curve is asymmetrical with a flood period of 4 hours and an ebb period of 8 hours near

Egmond. This tidal asymmetry is mainly caused by an interaction between the M2 and M4 tidal components. The mean semi-diurnal tidal range near Egmond has a value of 1.65 m. Spring and neap tidal range at Egmond are about 2.0 m and 1.4 m, respectively (Van Rijn et al, 2002).

Intertidal beach

Bars on the intertidal beach at Egmond can be divided into two types namely the low-tide swash bar and the high-tide swash bar. The low tide swash bar is positioned near the low-tide water line. There it is influenced by swash processes during low tide and by (breaking) wave processes during high tide. The high tide swash bar is positioned near the high-tide water line where it is influenced by swash processes during high-tide only.

4.3 Field experiment

4.3.1 Conditions

The wave conditions during the measurement period were mostly mild with an average wave period of about 1.5 m and an average direction of about 230 degrees to North. During the field campaign a complex, highly-irregular beach morphology was noticed at the location of the field campaign resulting in a wide range of wave directions. Because of the presence of a migrating bar immediately outside the intertidal beach just seaward of the mini tripods, the direction of the waves was highly affected. Frequently, the waves were propagating alongshore at the intertidal beach. Winds were mostly directed from south-south-east to west-south-west.

4.3.2 Data collection

During the field campaign in Egmond aan Zee from 19 September to 28 October 2005, data were simultaneously collected by video and in situ instruments using measuring devices attached to mini tripods. During the measurement period velocity, pressure and sediment concentration time series were collected in the intertidal zone. Also half hourly time stack images have been collected at the Coast3D Tower.

Video data

During the field experiment video data is collected from the cameras positioned on top of the Coast3D tower. This 40 m high tower is situated three kilometres to the south of Egmond aan Zee.

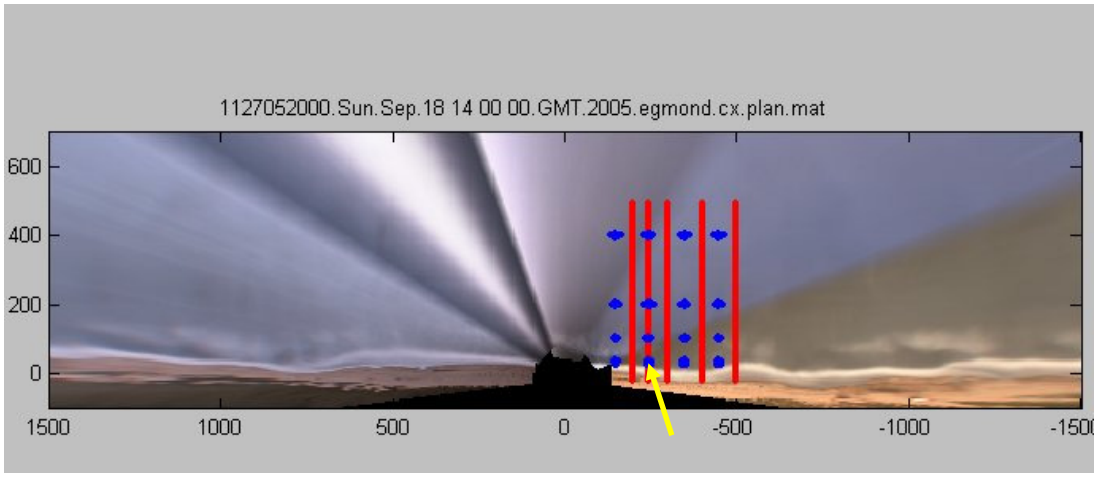

Figure 4-3 Plan view of Egmond aan Zee, Coast3D tower including pixel array design. Blue: alpha arrays. Red: bathy arrays. Yellow mark: location mini tripods.

The pixel sampling array was designed to cover the full extent of the main field experiment region and spanned the view of the three most northward cameras (see Figure 4-3). The five cross shore lines (bathy arrays) each consist of several pixels extending 400 m offshore from the shoreline. These bathy arrays will be used in this research to determine the wave celerity. The wave celerity is closely related to the underlying bathymetry so from this estimate we can derive a bottom profile. Furthermore 24 alpha arrays are placed around the location of the field experiment. These blue groups of pixels will be used to analyse the wave period and direction. An alpha array consists of 17 pixels deployed in a spatial pattern with a range of inter-sensor lags in both horizontal dimensions (Herbers et al., in press; Pawka, 1983). In this experiment 17 sensors are implemented and their accurate locations defined. Appendix B.2 shows the spatial array of pixels used in the directional spectral calculation. The 17 pixels are spread in a roughly diamond-shaped domain with dimensions of 50 and 100 m in the cross-shore and long-shore dimensions, respectively. The minimum distance between individual pixels is 5 m in the cross shore and 10 m in the long-shore (thus minimum resolvable wavelengths are 10 and 20 m respectively).

Using the known geometry of the image, the list of sampling locations (x,y,z) was converted to a corresponding list of pixel coordinates (U,V) in oblique images through standard photogrammetric procedures (Holland et al., 1997). Timestacks of pixel intensity were then collected half hourly, at each point in the array at a rate of 2 Hz for 17.17 min, 2060 samples every time. The collection of time stacks starts at 15 min and 45 min past every hour.

Ground truth data

During the field experiment four mini tripods of the laboratory of physical geography of the University of Utrecht are used to measure the water velocity, sediment concentration and wave height. With a DGPS (Differential Global Positioning System) the intertidal beach is measured every day during the six weeks of field experiments (see Appendix A).

The mini tripod is a small (about 2.0 m wide) instrumented tripod that can be deployed by hand in the intertidal area on the beach. Instruments include a pressure sensor (measures

waterlevel), three optical backscatter sensors (OBS) (measures sediment concentration), and an electromagnetic flow meter (EMF).

From the raw data files collected during the fieldwork the wave height, period and direction are calculated using spectral analysis. The energy density spectrum is calculated and from this spectrum the wave height is derived. The wave direction is calculated from the pressure, cross- and long shore velocity. The mean angle of incidence and the spreading around this mean angle is calculated using standard spectral techniques (Kuik, Eq. (3.6)). An energy weighted value (heigh frequency part) is calculated from this direction as function of *f*.

Every day at low tide the intertidal beach was surveyed with the DGPS and the measured data stored at the data logger in the mini tripod were read out using a laptop. After that the data logger was activated again. During high tide the mini tripods were again covered by water and new measurements could be made. The data is ordered and calibrated using Hardhat software. Hardhat is a time series analysis tool which splits and calibrates data files. The calibration includes correction for air pressure and conversion to surface elevation. Wave parameters can be computed from the measured time series.

4.4 Data selection

For further analysis a selection of the video and ground truth data is made. Due to problems with the Coast3D station the cameras only collected time stacks at 20 and 21 October and 26 to 28 October 2005. A criterion for the selection is the simultaneity of video and ground truth data. All video data files which coincide with ground truth data files are selected and vice versa.

Not included in analysis are:
- Stacks collected during night
- Stacks that are not complete, for example because of the incoming darkness
- Data of the most landward frame, as the measurement devices on that frame collected a minimum amount of data because of the low water level at that place.

The resulting data set consists of:
- Two and a half days of good quality time stacks at half hour intervals (43 stacks).
- Concurrent in situ measurements from 3 tripods.

The figures in the following sections correspond to the arrays and frames as stated in Table 4-1.

Table 4-1 Optical and in situ instruments

Optical instrument name	**Location**	**Corresponding mini tripod name**
a-246.25	intertidal beach	most landward frame nr. 15
a-246.31	intertidal beach	middle frame nr. 14
a-246.37	intertidal beach	most seaward frame nr. 13
a-246.100	surf zone	-
a-246.200	surf zone	-
a-246.400	shoaling region	-

The data selection which will be used in the analysis can be found in Appendix B.3.

5 Wave period and direction from video

5.1 Introduction

This section applies to objective one of this research, which is the application of an existing technique to determine the directional wave spectrum from video to a dataset from Egmond aan Zee. It discusses the applicability of optical measurements to estimate directional wave spectra in the nearshore from time stack images collected along the Dutch coast. The central question is how to interpret video observations of wave period and wave direction. A method has been used to calculate the directional spectrum $S(f, \theta)$ from video (Holman and Chickadel, 2004). The method is identical with that used to calculate the directional spectrum from arrays of pressure sensors, but the sensor elements are now pixels from video imagery and the signals are variations of optical intensity from each of the pixels. Various measures for wave period and wave direction have been determined from the directional spectra and a comparison is made between these measures. In situ data, obtained during the field experiment in Egmond aan Zee (Chapter 4.3), will be applied for ground-truthing.

5.2 Model description

High-resolution estimation of wave directional spectra involves analysis of synchronous time series of, for example, sea surface elevation η, collected at a set of locations. From the time domain signals, frequency (f) characteristics are found. From the spatial array, the directional (θ) and wavenumber (k) characteristics are computed for each frequency. The spatial lags between the optical instruments must span from a fraction of the shortest to approximately the longest wavelength of interest (Holman and Chickadel, 2004).

Holman and Chickadel (2004) have developed a technique called the Optical Wave Model (OWM) to calculate the directional spectrum $S(f, \theta)$ from video timestack data. Using the OWM, wave period and wave direction will be determined from timestack images. A time series of pixel intensities is measured at some specified locations (x, y). The timestack data I (t, x, y) will be used as input in the OWM. The model processes the data resulting in an estimate of the wave spectrum in the frequency-direction domain (Figure 5-1).

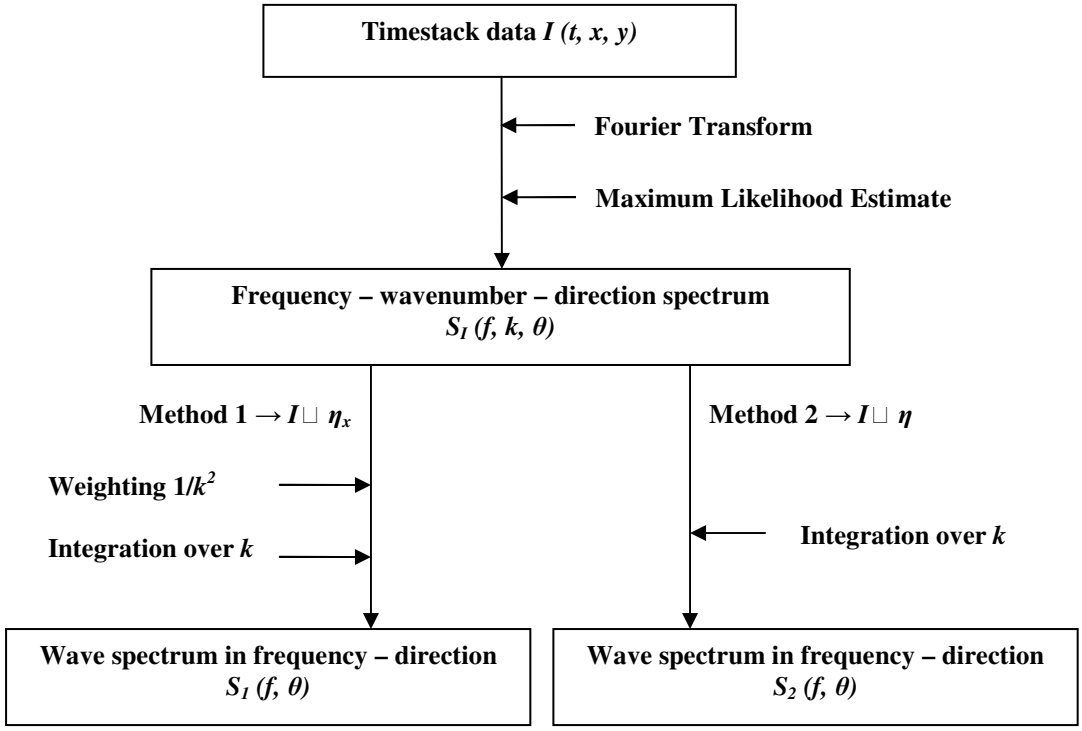

Figure 5-1 Scheme Optical Wave Model

The calculation of the directional spectrum starts with a Fourier transform of the data I (t, x, y) in time. Subsequently, the pixel arrays are processed using a maximum likelihood estimation of the wavenumber spectrum in each frequency band (Capon, 1969). This results in a frequency-wavenumber-direction spectrum $S(f, k, \theta)$. In this spectrum, f is the frequency, k the wave number and θ the direction of the wave.

The so called parameter dx in the Maximum Likelihood Estimate (MLE) is the spatial sampling interval used to define the Nyquist wave number (the highest wavenumber that can be coded at a given sampling rate in order to be able to fully reconstruct the signal). The dx value used in this analysis is dx = 1.0 m, adjusted to the circumstances at the Dutch coast. This value is based on the wave number conditions and corresponds to approximately the minimum lag of the pixels in the alpha array.

Two approximations are used to calculate the frequency-direction spectrum $S(f, \theta)$ from $S(f, k, \theta)$ as shown in Figure 5-1. The first method supposes that variations in sea surface slope due to waves cause reflection from different elevations in the sky, and that the intensity I is proportional to the wave slope. Subsequently the elevation can be derived from the intensity spectrum using the following relation:

$$S_{II} \square S_{\eta_x \eta_x} \square k^2 S_{\eta\eta} \tag{3.29}$$

with

$$\eta = e^{-i(kx-\omega t)}$$
$$\eta_x = \frac{\partial}{\partial x}\eta = ike^{-i(kx-\omega t)} = -ik\eta \tag{3.30}$$
$$S_{\eta_x\eta_x} = (\eta_x)^2 = k^2\eta^2 = k^2 S_{\eta\eta}$$

where S_{II} represents the intensity spectrum, k the wavenumber, η the elevation, η_x the wave slope and $S_{\eta\eta}$ the spectrum of the elevation. This results in

$$S_{\eta\eta}(f,k,\theta) = \frac{1}{k^2} S_{II} \tag{3.31}$$

This means the spectrum $S(f, k, \theta)$ has to be multiplied by a k^{-2} weighting. Finally, the spectrum S is integrated through all the wave numbers to estimate at the final spectrum $S(f, \theta)$:

$$S_{\eta\eta,1}(f,\theta) = \int_0^{k_{\max}} S_{\eta\eta}(f,k,\theta)\,dk \tag{3.32}$$

In the second method, it is assumed that the intensity I is proportional to the surface elevation η. This is shown in the following relation:

$$S_{II}(f,k,\theta) = S_{\eta\eta} \tag{3.33}$$

As a consequence, the spectrum $S(f, \theta)$ can be determined directly from the frequency-wavenumber-direction spectrum by integrating over all the wavenumbers:

$$S_{\eta\eta,2}(f,\theta) = \int_0^{k_{\max}} S_{II}(f,k,\theta)\,dk \tag{3.34}$$

In the Optical Wave Model as used by Holman and Chickadel (2004), only wave periods smaller than 15 s are included in the analysis, relating to the wave characteristics on the coast of the USA. Until now, the technique is only tested in the United States (Figure 5-2), representing a wave climate of mainly swell, that means wave periods in the order of 12 s. Thus wave periods bigger than 15 s are considered to be unrealistic in the OWM.

Results of the NCEX experiment in San Diego (Figure 5-2) show a good similarity between the optical and in situ wave measurements, except that the energy density in the lower frequencies is overestimated. By weighting the optical spectra over k^{-2} to derive the wave spectrum from the intensity spectrum the energy density of the lower frequencies is increased artificially. Together with the corresponding de-emphasizing of the high frequencies this could result in some errors. The weighting is based on the hypothesis that variations in optical radiance due to waves are related to variations in sea surface slope (yielding a wavenumber dependency). This is an approximation and only applies to the component of sea surface slope in the direction away from the camera (Holman and

Chicakel, 2004). Better understanding and implementation of this relationship is recommended.

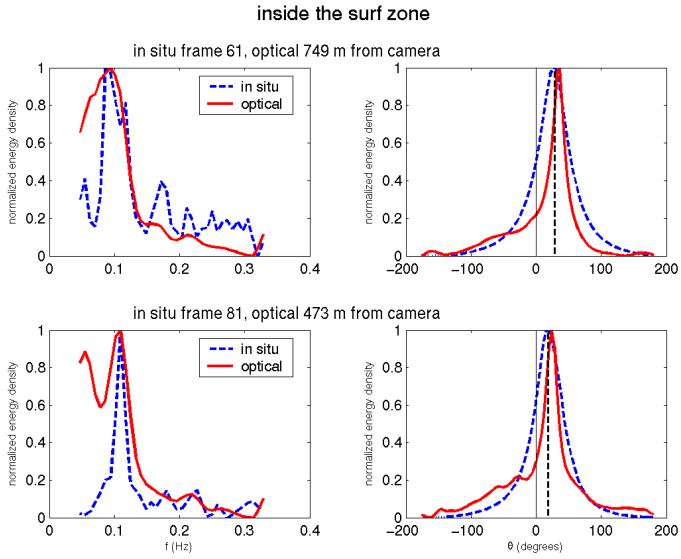

Figure 5-2 Application of the Optical Wave Model during the NCEX experiment in San Diego. Comparison of optical (red) and in situ (blue) measured, scaled spectra, at two different locations in the breaker zone.

5.3 Applicability of the model

5.3.1 Frequency and direction spectrum

As stated in Chapter 5.2, the spectrum $S(f, \theta)$ is determined from the timestack data. An example of such a spectrum is given in Figure 3-4. The frequency spectrum $S(f)$ is computed from the spectrum $S(f, \theta)$ by integrating over all directions according to Eq. (3.1).

The optical frequency spectra derived from video are compared with the in situ spectra to be able to assess accuracy of the results. An example of a frequency spectrum is given in Figure 5-3. In Appendix C.1, all spectra derived from the data collected during the field experiment (see Chapter 4.3) are shown. The spectra in these figures are normalized over the total spectral density of the spectrum.

The spectrum derived from the in situ data is represented as a black line and is determined using the maximum entropy method of Krogstad (1986), Eq. (3.7), (3.8), (3.12) and (3.13). Three different frequency spectra from video are determined. The blue line represents the spectrum weighted over k^{-2}. As shown in Figure 5-3 and the spectra in Appendix C.1, the energy density of the lower frequencies is increased artificially by the weighting. The green line reflects the spectrum from video without weighting over k^{-2}. In comparison to the weighted spectrum (blue line) the peak in the lower frequencies is smaller because no weighting is applied that increases the frequencies corresponding to the smaller wavenumbers. Comparing these two spectra in the high frequency region it can be observed distinctly that the optical spectrum corresponding to the k^{-2} weighting (blue line) is de-

emphasizing the higher frequencies as explained in Chapter 5.2 since the blue line is situated underneath the green line in this part of the spectra.

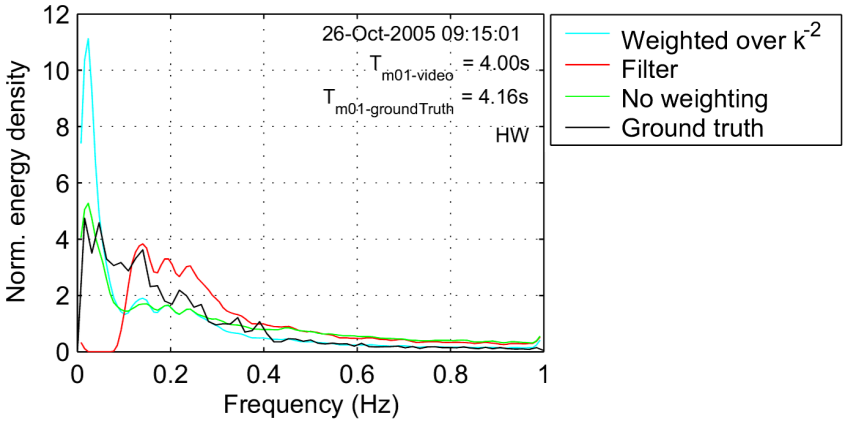

Figure 5-3 Comparison of optical (blue, red, green) spectra and in situ (black) measured scaled frequency spectra at the most landward optical instrument a-246.25. The blue and green lines represents respectively with and without weighting over k^{-2}. For the red line a high pass filter is applied before weighting and integration over k. HW means the spectrum corresponds to a point of time during high tide.

The red line in Figure 5-3 and the spectra in Appendix C.1 represent the optical spectrum while applying a high-pass filter. This filter leaves out the frequencies smaller than 0.1 Hz (about half of the peak frequency) of the data $S(f, k, \theta)$. After applying this filter the resulting dataset is again multiplied by a k^{-2} weighting. It is obvious from the red line in the figures that the lower frequencies (< 0.1 Hz) are rejected. In the remaining part of the spectra (higher frequencies) the shape of the spectrum is in accordance with the weighted spectrum without filter (blue line), considering the normalization over the total spectral density of the spectrum. The shapes of the optical spectra show correspondence with the in situ spectrum. In the low-frequency part of the spectrum the in situ spectrum seems to approach the spectra without weighting over k^{-2} and while applying a high-pass filter. In the high frequency part of the spectrum, the line corresponding to the weighted spectrum seems to give the most realistic reflection of the ground-truth data.

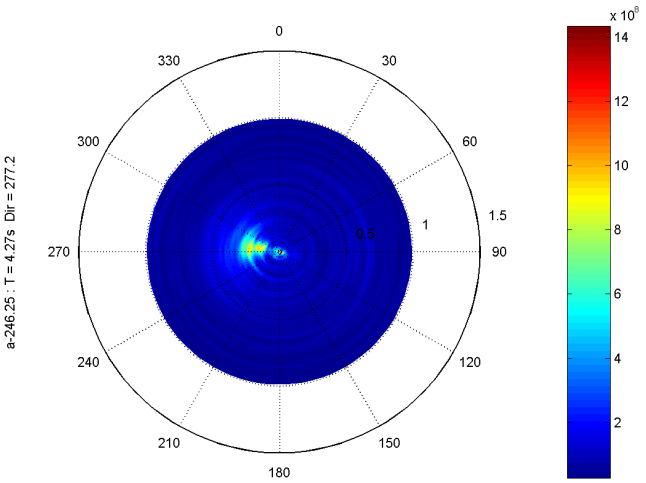

Figure 5-4 Directional spectrum (nautical) intertidal beach Egmond aan Zee, 26 October 2005 8:15 Hrs

An example of a directional spectrum derived from video and ground truth data is represented in Figure 5-5. In Appendix C.2, all spectra for the different instruments and points in time derived from the data collected during the field experiment (see Chapter 4.3) are shown. The spectra in these figures are normalized over the total spectral density of the spectrum.

The optical directional spectra are computed from the spectrum in frequency-directional domain (Figure 5-4) by integrating over all the frequencies. The four lines represent the same calculation methods as the lines presented in Figure 5-3. Generally two peaks can be noticed in the spectra. The peak at around 90 degrees corresponds to sea going waves and the peak at around 270 degrees in the figure reflects the waves propagating in the direction of land. The agreement between the optical and in situ data is obvious, especially for the land going waves. The left peak in the spectrum represents the reflected signal of the waves as they have returned from the beach. It is obvious that the filtered data do not show such a second peak in the spectrum. In this red line the low frequencies representing swell have been filtered out. Most probably the left peak is caused by these low frequency waves that are reflected by the sloping beach. Because these swell waves are long and less steep they will notice the sloping beach as a straighter wall than the higher frequented short wind waves. Therefore these waves are better reflected thus corresponding to the left peak in Figure 5-5. This is also shown in Figure 5-3 where in the blue, green and black line also a peak can be noticed in the lower frequencies.

The values of the directions determined in Figure 5-5 (Dir_{mean}, Dir_{field}) and Appendix C.2 are not calculated using the shape of the spectra in this figure but using the method of Kuik stated in Eq. (3.6) to (3.10). Using this method the direction is calculated corresponding to the frequency with the highest energy density. A motivation for applying this standard method is that the direction is determined for the waves with a frequency corresponding to the highest energy density thus considering the wind waves we are most interested in. By determining the direction considering the peaks in Figure 5-5, waves with all kind of frequencies are involved in the calculation, also the ones with low energy density which will not give a reliable result for the direction.

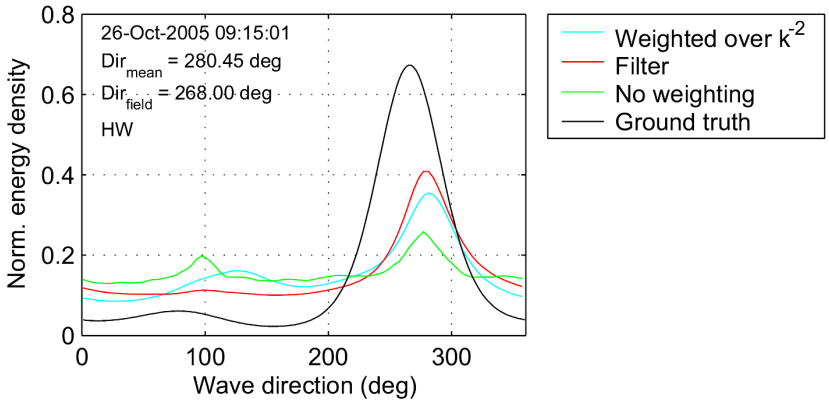

Figure 5-5 Comparison of optical (blue, red, green) spectra and in situ (black) measured scaled frequency spectra at the middle optical instrument a-246.31 at the intertidal beach. The blue and green lines represents respectively with and without weighting over k^{-2}. For the red line a high pass filter is applied before normalization and integration over k. HW means the spectrum corresponds to a point of time during high tide. Directions are given in degrees with respect to North.

5.3.2 Determination period and direction

The period and direction of the waves can be determined from the wave spectrum in frequency direction domain, $S(f, \theta)$, see Eq. (3.2) to (3.5) and Eq. (3.9) to (3.11) respectively. Holman and Chickadel (2004) use T_{peak} to determine period and direction. The peak period is determined from the inverse of the frequency with maximum energy density (Eq. (3.11)). As the North Sea wave conditions, which represent a broad wave spectrum, differ from the swell-dominated spectra usually found at the coast of the USA, the resulting spectrum is not necessarily single-peaked. This means T_{peak} is not always well defined. It will be better not only to observe the peak of the spectrum, but the spectrum as a whole. Therefore, also T_{m01} is calculated as the video-based indicator for wave period. The T_{m01} is calculated applying Eq. (3.5). For the optical instruments situated in the shoaling region T_{m02} is applied (Eq. (3.4)) as indicator for the wave period because only offshore T_{m02} data is available for ground-truthing. Consequently, a mean (weighted) wave direction (Eq. (3.9) and (3.10)) is calculated to adjust to the different wave conditions at the North Sea in comparison to the Pacific.

To determine the correlation between the video data and the simultaneously measured in situ data, the video data are plotted against the ground truth data. To quantify the quality of a set of stack averaged wave period estimates, quality values are calculated (Eq. (3.24) to (3.27)), i.e. the root-mean-square value of the difference between video derived wave period and in situ wave period, the standard deviation of that difference and the correlation coefficient between the video derived period and ground truth period. In the following these measures are respectively described with ΔT_{rms}, $\sigma_{\Delta T}$ and $corr_{coef}$. To quantify the wave direction estimates from video, the same values are calculated.

5.3.3 Results wave period

In this section the optical wave period and in situ wave period will be compared. Three scatter plots are shown in the Figure 5-6 to Figure 5-14 representing the three methods used to calculate the spectrum, that is with weighting over k^{-2} (Eq. (3.31) and (3.32)), applying a high-pass filter before weighting over k^{-2} (ignoring frequencies lower than 0.1 s^{-1}) and without adopting the weighting over k^{-2} (Eq. (3.34)). As shown in Figure 5-6 to Figure 5-14, the scatterplots represent the results corresponding to the deepest instrument a-246.37 at the intertidal beach in comparison with the deepest mini tripod nr. 13. In Appendix D, all scatterplots derived from the data collected during the field experiment (see Chapter 4.3) are shown.

Peak period

Figure 5-6 shows the correlation between the in situ peak period and the peak period determined from video.

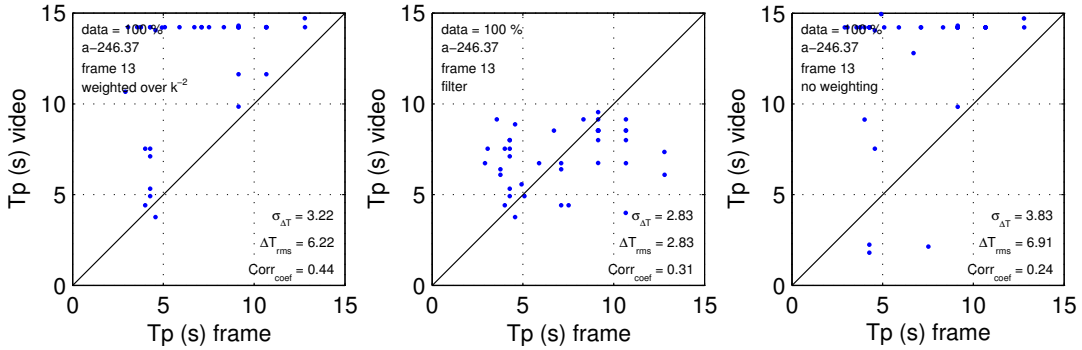

Figure 5-6 Peak period video data plotted against in situ peak period, all data, applying a weighted over k^{-2} spectrum (left figure), filter including weighting over k^{-2} (middle figure) and spectrum without weighting over k^{-2} (right figure).

Because the energy density in the lower frequencies is overestimated by the Optical Wave Model a lot of calculated periods exist with a value higher than 10 s. Holman and Chickadel (2004) therefore decided to remove unrealistic data with a period higher than 15 s from the dataset. Nevertheless the wave climate along the North Sea differs from that in the Pacific.

Moreover, optical data emphasize high frequency motions, but retains the phase and coherence information of lower frequency swell. By contrast, in situ sensors do not notice these high frequency motions due to rapid depth attenuation (Holman and Chickadel, 2004). i.e., the very short wind waves often observed visually rapidly diminish with depth. Even at one meter depth, in situ instruments will not notice this signal. Therefore, time series from in situ instruments are usually smooth and dominated by the dynamically important wave periods. Optical data are subject to short wavelengths waves so will always be noisier than in situ data. This can cause differences by comparison of optical and in situ spectra. With the comparison of optical and in situ wave period and direction these differences will be excluded, because the spectra are considered between 2 and 9 s and consequently the high and low frequencies have been filtered out.

Therefore in this work the energy density spectrum is used between 0.11 and 0.5 s (see Figure 5-7), which means that periods above 9 s or below 2 s are considered to be unrealistic. In the upper left corner of every figure the percentage is given of the part of the dataset that is presented in the figure, containing the percentage of the data that belongs to the spectrum between 0.11 and 0.5 s.

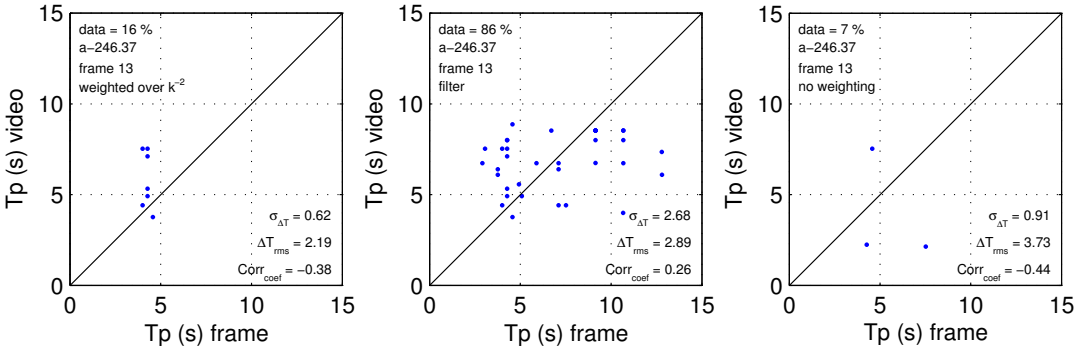

Figure 5-7 Peak period video plotted against in situ peak period, 2s < T_{m01} < 9s, applying a weighted over k^{-2} spectrum (left figure), filter including weighting over k^{-2} (middle figure) and spectrum without weighting over k^{-2} (right figure).

As expected the Egmond video data shows almost no correlation with the ground truth data. The peak period does not seem a good estimate to calculate the period from video data because we do not have a well-defined peak in the frequency spectra (Appendix C.1). This is confirmed by the field work data (Figure 5-7) and is explained by the fact that in very shallow water the wave spectrum is very broad and the peak is not clearly determined. Therefore the T_{m01} will be determined in the next section. As shown in Figure 5-7, by ignoring the periods outside the range of 0.11 to 0.5 seconds, a large part of the data is not used to derive an estimate from.

$T_{m_{01}}$ period

In this section the correlation between the in situ T_{m01} and the T_{m01} from video will be discussed (Figure 5-8).

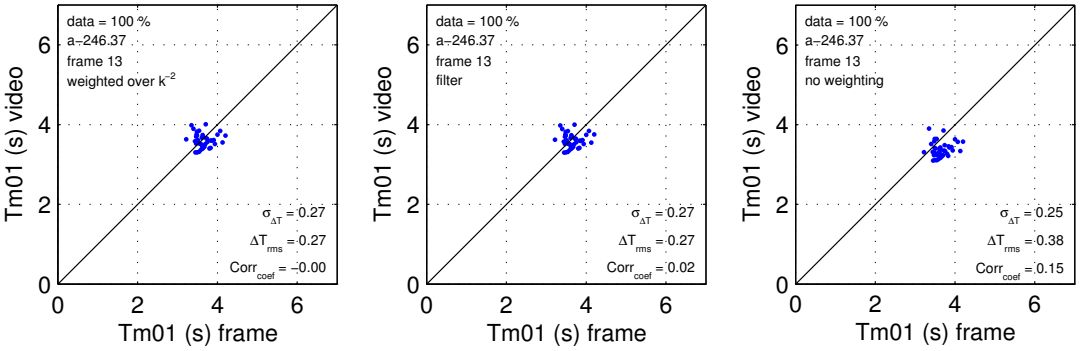

Figure 5-8 T_{m01} video plotted against in situ T_{m01}, 2s< T_{m01}< 9s, applying a weighted over k^{-2} spectrum (left figure), filter including weighting over k^{-2} (middle figure) and spectrum without weighting over k^{-2} (right figure).

The Egmond video data show correlation with the ground truth data characterized in T_{m01} as can be seen in Figure 5-8. The root-mean-square value of the difference between video derived T_{m01} and in situ T_{m01} is much less (0.27) than the root-mean-square value corresponding to the peak period (2.19 to 3.73). The T_{m01} seems a better method to calculate the wave period of the video data. This could be expected, because the T_{m01} considers the shape of the spectrum as opposed to determining the peak of the spectrum. Because the spectrum between 0.11 and 0.5 s is considered and the filter is operating outside this region,

the first two methods in Figure 5-8 show the same results. The method without weighting over k^{-2} produces a better result by comparing the $\sigma_{\Delta T}$ and $corr_{coef}$, this means in the intertidal area the intensity is probably proportional to the elevation.

$T_{m_{02}}$ period

The offshore period is compared with the deepest optical instruments (Figure 5-9) situated in the shoaling region. Here the sea is more calm and this results in a better correlation ($corr_{coef} \approx 0.70$) between the video data and the offshore measurements than for the instruments in the intertidal area. The standard deviation is larger than calculated for the intertidal instruments (0.42 as opposed to about 0.25), this can be explained by the larger spreading of the periods in the shoaling region.

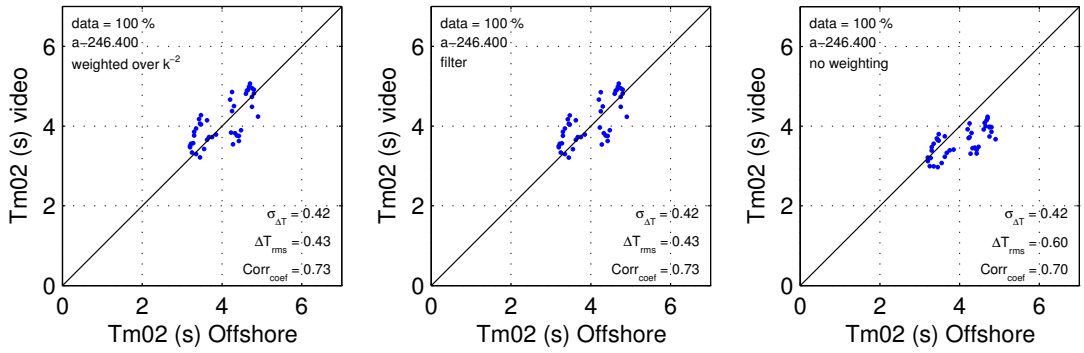

Figure 5-9 T_{m02} video plotted against T_{m02} offshore, 2s< T_{m02} <9s, for an instrument located at x=400m applying a weighted over k^{-2} spectrum (left figure), filter including weighting over k^{-2} (middle figure) and spectrum without weighting over k^{-2} (right figure).

The periods calculating by weighting over k^{-2} and the periods by applying the filter before weighting give a better correlation than without applying the weighting. This in contrast to the T_{mo1} calculated in the intertidal area that better corresponds to the method without weighting. This is probably caused by the fact that in de shoaling region the camera is observing the waves more oblique than the waves closer to the camera. In the intertidal area the waves are observed more from above. This means further away from the camera in the shoaling region the intensity corresponds to the slope of the waves and weighting over k^{-2} have to be applied to receive the best results.

5.3.4 Results wave direction

In this section the optical wave direction and the in situ wave direction will be compared. The method of Kuik (1988), see Eq. (3.6), is used to analyse both the data collected from the mini tripods as the data from the time stacks. The peak wave direction can be determined from the peak wave frequency in the spectrum (Eq. (3.11)). On the basis of the results of the comparison of in situ and video peak periods it has to be expected that the peak direction also does not give a good correlation because the peak in the frequency spectrum is not well defined. Therefore the peak wave direction is not analysed but the mean wave direction is derived in the next section.

A complex morphology existed at the location and time of the field test (Chapter 4.3.1). First the angle depending on frequency is calculated using the method of Kuik (see section 3.2). The spectral parts of Eq. (3.7) and (3.8) are applied for the video data and the right parts in these equation are used to determine the direction from the in situ data. The directional spectrum frequently has several peaks, see Figure 5-5. To determine the main direction more accurate, the waves propagating seaward are neglected in the following.

Mean wave direction

The mean angle is than calculated using two methods. First the same method as used in the Swan wave model is applied to determine the mean angle (Eq. (3.9)). Secondly the weighted mean is calculated (Eq. (3.10)). This results in the following scatter plots for the mean direction.

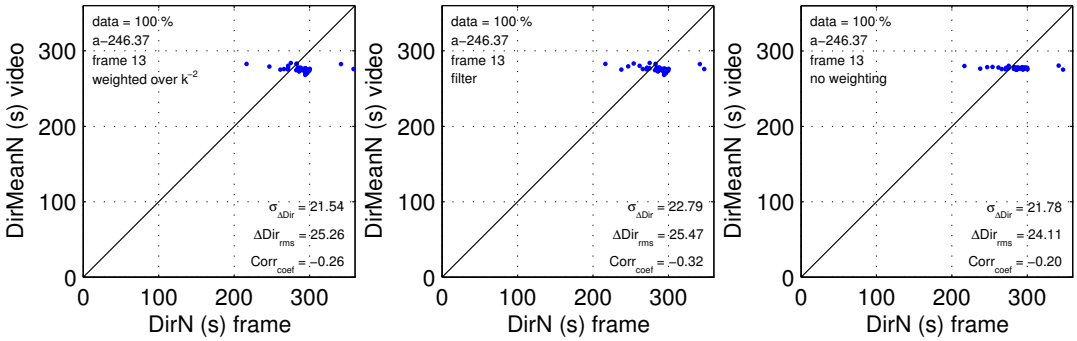

Figure 5-10 Mean direction video plotted against in situ mean direction (Swan method), $2< T_{m01} < 9{,}5$s, seaward propagating waves neglected, applying a weighted over k^{-2} spectrum (left figure), filter including weighting over k^{-2} (middle figure) and spectrum without weighting over k^{-2} (right figure).

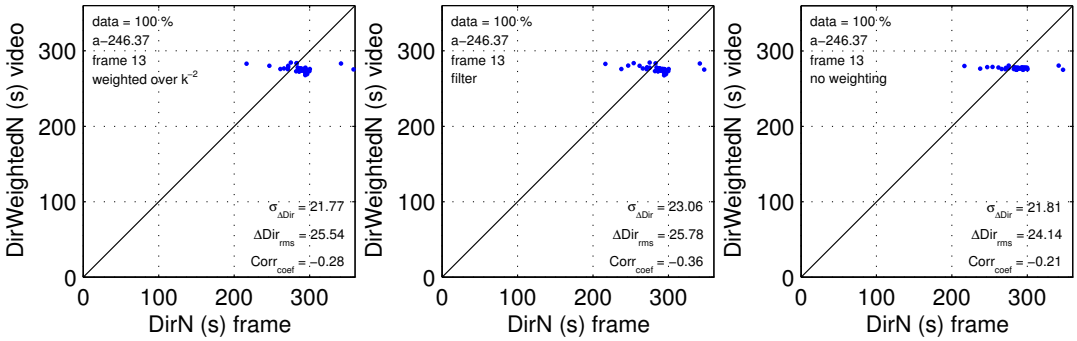

Figure 5-11 Mean direction video plotted against in situ mean direction (weighted mean), $2< T_{m01} < 9{,}5$s, seaward propagating waves neglected, applying a weighted over k^{-2} spectrum (left figure), filter including weighting over k^{-2} (middle figure) and spectrum without weighting over k^{-2} (right figure).

The results of the video data are situated on a straight line, representing waves propagating perpendicular to the coast. Because of refraction in the shoaling and surf zone this result had to be expected. The ground-truth data however do not show this perpendicular entering of the waves when approaching the coast. The weak correlation of the video and ground-truth data could be a result of the complex morphology in that area (Chapter 4.3.1). Furthermore the measuring devices applied to the mini tripods are located under the water level thus measuring the waves inside the water, where the water is also influenced by long-shore

currents and undertow. The optical signal however is measured at the surface and will not notice these currents influencing the direction measured by the frames.

The results in Figure 5-10 and Figure 5-11 are quite corresponding. However, because of the weighting over the energy density of the frequency spectrum, the weighted mean direction seems the most reliable estimate of the direction, because then the shape of the spectrum is considered as well. No significant difference can be noticed according to the three different methods (k^{-2} weighting, filter, no weighting) to calculate the spectrum.

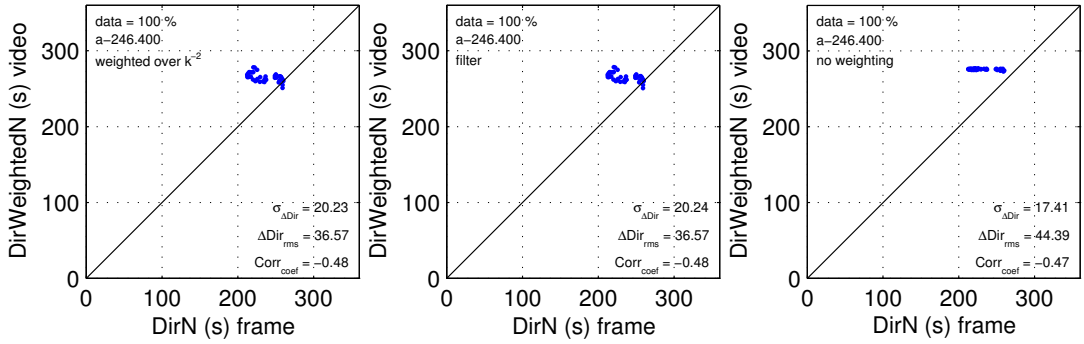

Figure 5-12 Mean direction video plotted against in situ mean direction (weighted mean), $2< T_{m01} < 9{,}5$s, for an instrument located at x=400m. Seaward propagating waves have been neglected, applying a weighted over k^{-2} spectrum (left figure), filter including weighting over k^{-2} (middle figure) and spectrum without weighting over k^{-2} (right figure).

In Figure 5-12 the weighted mean wave direction corresponding to an instrument in the shoaling region is shown. Just like the results of the direction measured in the intertidal area no correlation can be found. However, the results in the shoaling area cannot be related to the complex morphology and therefore it is concluded that the method to derive wave direction from video need further research. Consequently also the weak correlation in the intertidal area cannot be fully attributed to the complex morphology during the fieldwork.

5.3.5 Tidal influence

In this section data is analysed during high water because then the waterlevel is higher which will probably give better results. According to Figure 5-13 and Figure 5-14, only considering the data collected during high water does increase the reliability of the results for the period as for the direction. This is concluded by comparing the quality values stated in these figures by the values given in the figures in the previous section see (Table 5-1 and Table 5-2). However less data (only 56%) of the already small set can be used for ground-truthing.

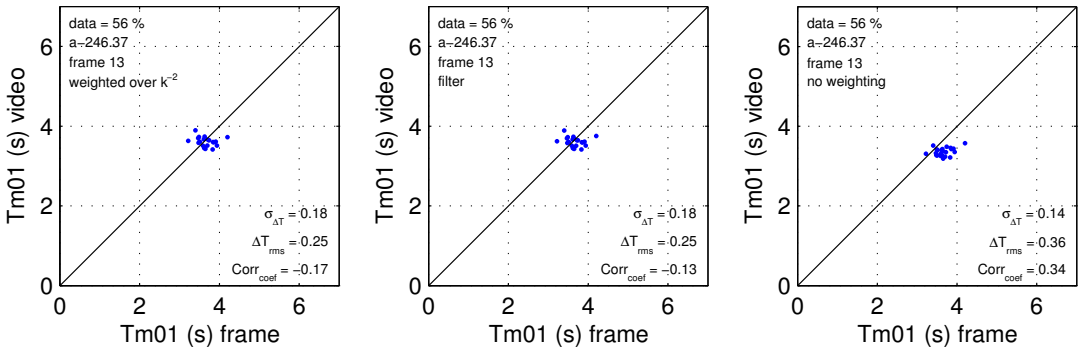

Figure 5-13 T_{mo1} video plotted against T_{m01} in situ during high water (waterlevel above 0 m). Applying a weighted over k^{-2} spectrum (left figure), filter including weighting over k^{-2} (middle figure) and spectrum without weighting over k^{-2} (right figure).

Table 5-1 Comparing data video and ground truth T_{m01} with and without tidal limitation

T_{m01} intertidal area		All data	Data during high tide
weighted over k^{-2}	$\sigma_{\Delta T}$	0.27	0.18
	ΔT_{rms}	0.27	0.25
	$corr_{coef}$	-0.00	-0.17
filter	$\sigma_{\Delta T}$	0.27	0.18
	ΔT_{rms}	0.27	0.25
	$corr_{coef}$	0.02	-0.13
no weighting	$\sigma_{\Delta T}$	0.25	0.14
	ΔT_{rms}	0.38	0.36
	$corr_{coef}$	0.15	0.34

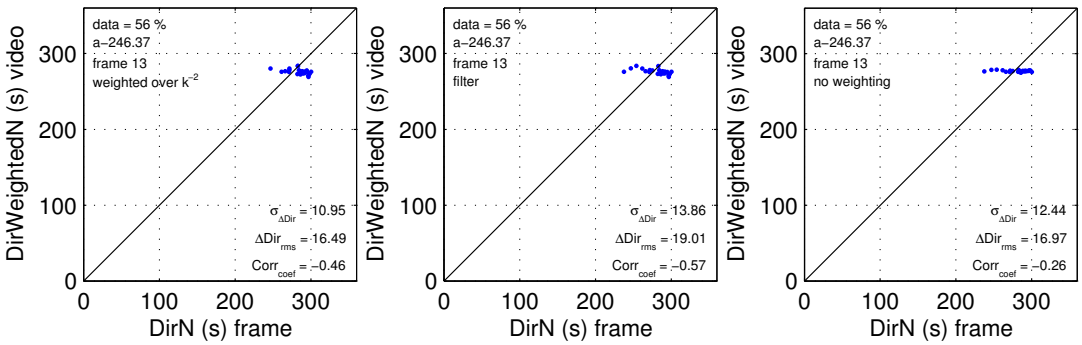

Figure 5-14 Mean weighted direction video plotted against mean in situ mean weighted direction during high water (waterlevel above 0 m). Applying a weighted over k^{-2} spectrum (left figure), filter including weighting over k^{-2} (middle figure) and spectrum without weighting over k^{-2} (right figure).

Table 5-2 Comparing data video and ground truth direction with and without tidal limitation

Weighted mean direction intertidal area		All data	Data during high tide
weighted over k^{-2}	$\sigma_{\Delta T}$	21.77	10.95
	ΔT_{rms}	25.54	16.49
	$corr_{coef}$	-0.28	-0.46
filter	$\sigma_{\Delta T}$	23.06	13.86
	ΔT_{rms}	25.78	19.01
	$corr_{coef}$	-0.36	-0.57
no weighting	$\sigma_{\Delta T}$	21.81	12.44
	ΔT_{rms}	24.14	16.97
	$corr_{coef}$	-0.21	-0.26

5.3.6 Location instruments

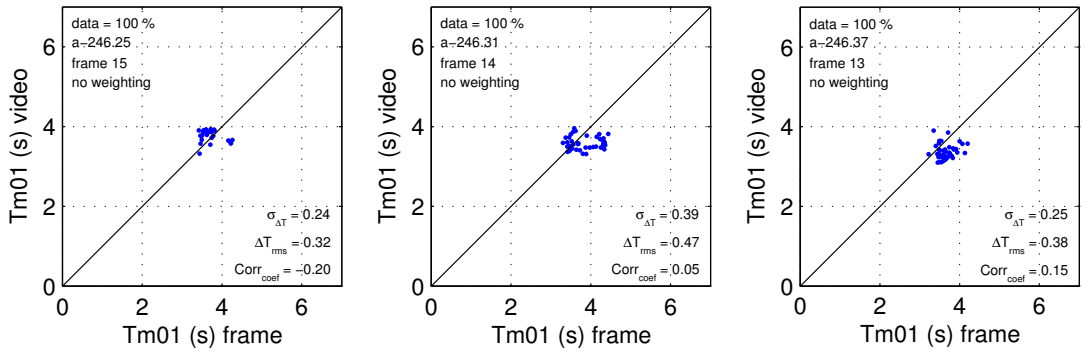

Figure 5-15 T_{m01} video plotted against T_{m01} in situ for three instruments in the intertidal area for applying no weighted over k^{-2} . The instruments are situated respectively at x=25, 31 and 37 m.

Scatterplots corresponding to the three different instruments situated in the intertidal area (spectra without weighting over k^{-2}) are given in Figure 5-15 and Figure 5-16. It is not clearly visible which of these instruments give the best results. Comparing the correlation and standard deviation of these instruments does not give a preference for one of them. The deepest instrument is covered by water earlier than the other two and therefore more data for ground-truthing is collected and the results are therefore based on a larger dataset. For the instruments situated in the shoaling region the correlation is better for the deepest of these three instruments as can be seen in Figure 5-17. The optical periods obtained with these instruments are compared with offshore data and at the location of the deepest instruments slightest influence of the bottom is noticed. As a result the offshore period at the location of the deepest optical instruments has slightly changed in comparison to the offshore period at deep water.

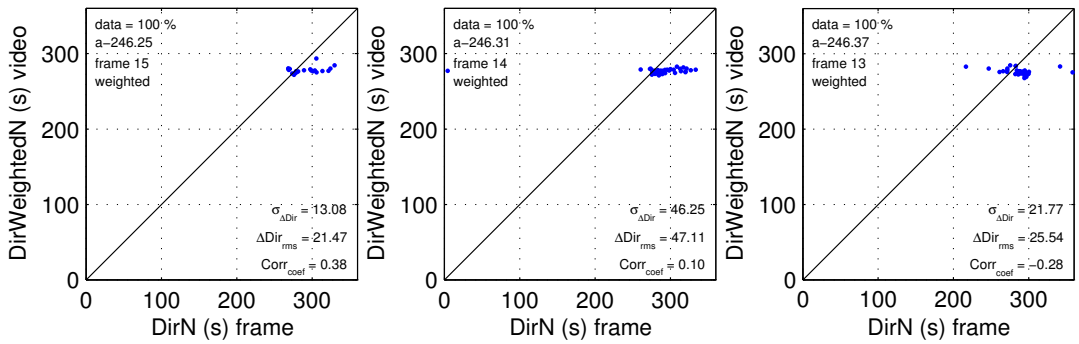

Figure 5-16 Mean weighted direction plotted against in situ weighted mean direction for three instruments in the intertidal area applying a weighted over k^{-2} spectrum.

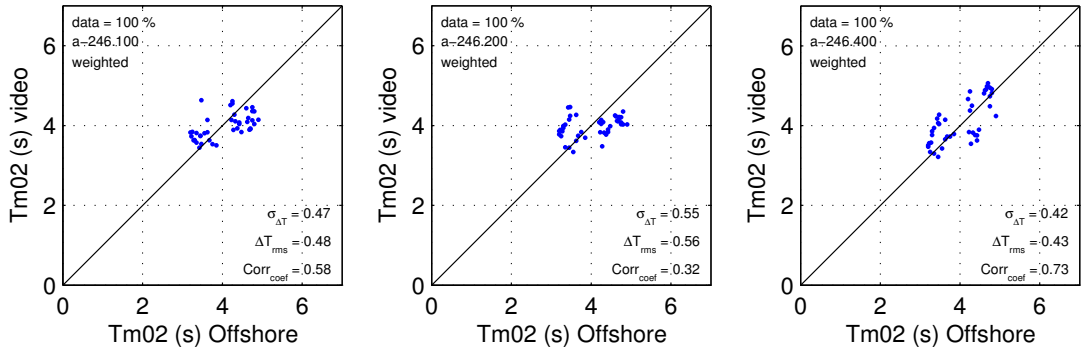

Figure 5-17 T_{m02} video plotted against T_{m02} offshore for three instruments at different locations in the shoaling region applying a over k^{-2} spectrum.

5.4 Synthesis

The Optical Wave Model (Holman and Chickadel, 2004) is applied to calculate the directional spectrum $S(f, \theta)$ from video. Three different methods are used to calculate the frequency and directional spectrum, i.e. weighting over k^{-2}, filtering and weighting, and without weighting over k^{-2}. By determining the period over the spectrum between 2 and 9 s the method without weighting corresponds the most to the in situ spectrum for the instruments in the intertidal area. For the instruments in the shoaling region, the periods calculating by weighting over k^{-2} and the periods by applying the filter before weighting give a better correlation than without applying the weighting. Generally, the comparisons made here are quite encouraging. The value of the period in each spectrum appears accurate within a few tenths of seconds. Considering the wave direction, the three methods used does not show a significant difference in results. Summarized, the following conclusions can be made:

- The Optical Wave Model can be applied to the Dutch coast. The frequency spectrum has to be considered between 0.11 and 0.5 s^{-1}.
- Wave period is best estimated from video by T_{m01}.
- The optical frequency spectrum using the method without weighting over k^{-2} shows the best correlation with the ground-truth data for the intertidal area. Therefore the intensity in the intertidal area seems proportional to the elevation.

- In the shoaling region further away from the camera the intensity corresponds to the slope of the waves and weighting over k^{-2} have to be applied to receive the best results.
- Overall: poor correlation for wave direction, at least partly attributed to complex beach topography and limited dataset.
- Wave direction is best estimated from video by the weighted mean direction.
- Correlation increases by only applying data collected during high water.

Some remarks are given below:

The optical spectra represent a rather large area (order 10 by 20 m in the intertidal area) as opposed to the point measurement obtained from the in situ measurement at the same location of the instrument. This can introduce discrepancies between the video and in situ results.

Optical data emphasizes high frequency motions, but retains the phase and coherence information of lower frequency swell. By contrast, in situ sensors do not notice these high frequency motions due to rapid depth attenuation. This can cause difference by comparison of in situ and video data.

6 Wave celerity from video

6.1 Introduction

This section applies to objective two in this research. The central question is how well we can determine wave celerities from video data in the time domain rather than in the spectral domain. Data are used from pixel intensity time series at cross-shore arrays of locations sampled from the field experiment in Egmond aan Zee, October 2005, see Chapter 4.3. Stockdon and Holman (2000) applied a cross-spectral technique to calculate wave celerity, or wave phase speed, and corresponding bathymetry. However, other techniques can be applied to calculated wave phase speed from pixel intensity time series. The idea occurred to use a cross correlation method in stead of a spectral technique to calculate celerity (pers comm. Roelvink). In this section cross correlation of remotely collected intensity data will be applied to estimate wave celerity and subsequently local bottom level is inferred based on linear wave theory.

6.2 Approach

The analysis of the video technique is performed with data collected at Egmond aan Zee, during the experiment of October 2005 (Chapter 4.3.2). Half hourly pixel intensity time series of 2060 data points corresponding to more than 17 minutes are available for five cross-shore arrays. Each cross-shore array consists of 84 pixels. The distance between neighbouring pixels in an array increases by increasing depth, thus varying between around 5 m (intertidal beach) and 8 m (500 m in shoaling region).

The time lag between two timeseries is estimated from cross correlation of intensity time series in neighbouring pixels from each point in the stack. For different time lags between two timeseries the cross correlation is calculated between pixels i and j in these series using Eq. (3.21) and Eq. (3.22). The celerity in x-direction (c_x) is determined by Eq. (3.14) using the lag belonging to the maximum correlation in one point and the distance between the two pixels used to calculate this correlation. The c_x is transformed to c using Snells law (Eq. (3.15) and (3.16)).

In the following, two different approaches will be described to calculate time lag and bathymetry. First the original intensity signal is used to calculate c and the corresponding bottom profile (Chapter 6.3). Furthermore the envelope of the intensity signal is determined resulting in an estimate of the group wave phase speed and a matching bathymetry (Chapter 6.4).

6.3 Individual wave phase speed

In this section the individual intensity signal is used to calculate wave phase speed in *x*-direction. Some operations are performed to improve the results of the estimate of the time lag and bottom level which will be discussed in the following.

Filter

In the raw intensity time series a low frequency signal is observed. Therefore the original intensity signal from the stack is first smoothed with a high-pass filter to remove low-frequency trends. Frequencies lower than 0.05 s^{-1} are eliminated by this filter. Also a low-pass filter that excludes frequencies higher than 0.5 s^{-1} is applied to remove noise.

Accuracy

The stacks of 17 minutes length (2060 data points) are divided into three sub-samples of the same length, corresponding to 686 data points (2 per second). For every sub-sample of the signal, the maximum lag is determined for each pixel point in the array. Some spreading in the maximum lag is noticed. Therefore the median lag from the multiple estimates from sub-samples from the stack is determined (Figure 6-1). Error bands corresponding to plus or minus the standard deviation are determined from the multiple estimates from sub-samples in the time stack. If the standard deviation divided by the median lag in a point is higher than 0.5, the estimate is unreliable and therefore no lag and celerity will be determined for this point.

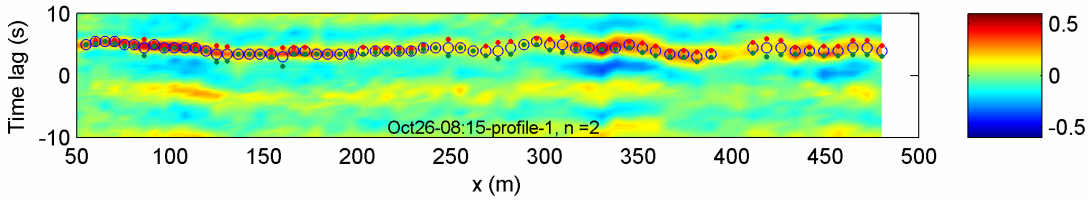

Figure 6-1 Correlation along the cross-shore array from *x*=50 to *x*=500 plotted against time lag for pixel intensity time series. The circles represent the estimated time lag corresponding to the maximum cross-correlation between pixel intensity time series. The red and dark green dots represent the standard deviation of the time lag.

At both sides of the maximum lag a minimum lag can be indicated. For the three sub-samples of the signal, the period of the intensity signal is then determined as the distance between these minimum lags. Some spreading in the period is observed as well and correspondingly the standard deviation of the period is calculated. If the standard deviation of the period divided by the median lag in a point is higher than 0.5, the estimate is unreliable and therefore no celerity will be determined for these points.

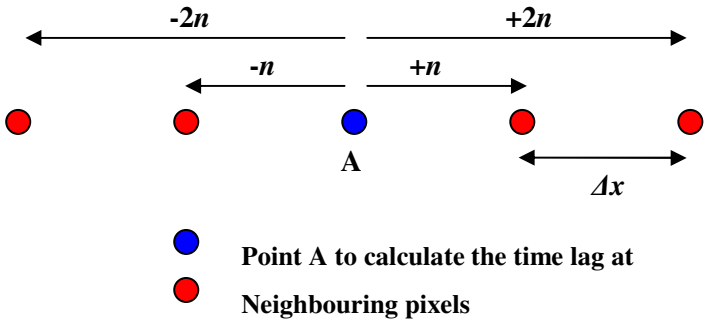

Figure 6-2 Step-size between points in the cross-shore array

The time lag from cross correlation of intensity time series in one point (point A in Figure 6-2) is estimated in two neighbouring pixels of that point (Figure 6-2). These neighbouring pixels are situated at a step-size $+n$ times the distance between two pixels (Δx) and $-n$ times this distance. Consequently n represents the step-size in number of pixels to both sides of point A. In Figure 6-3 is shown the time lag corresponding to maximum correlation by increasing values of n from 1 to 5. The subsequent figure with values of n from 6 to 10 is shown in Appendix E.

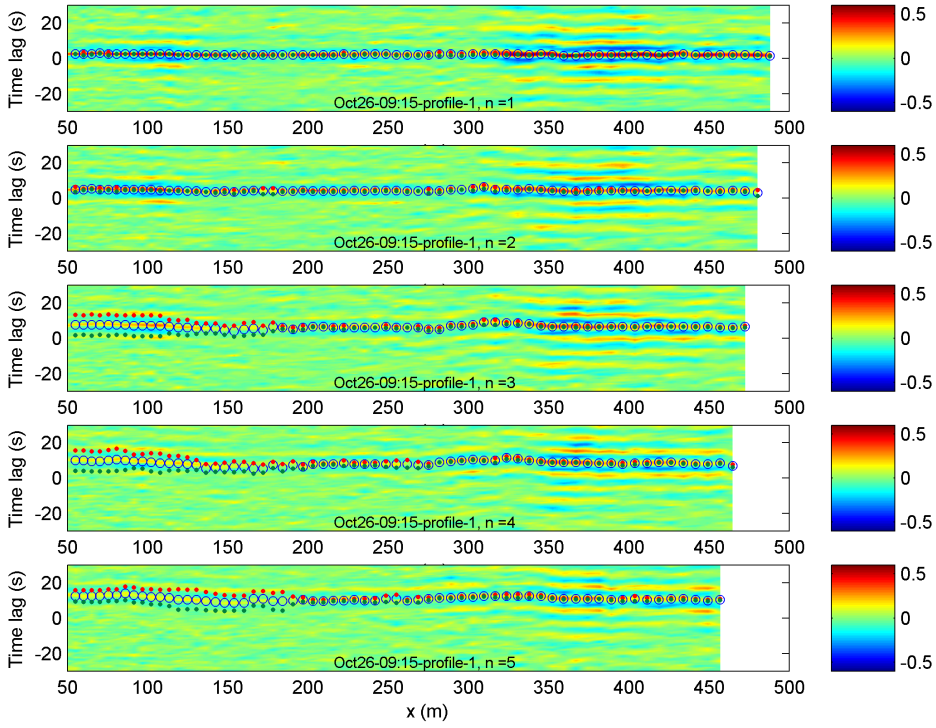

Figure 6-3 Correlation along the cross-shore array from x=50 to x=500 against time lag for pixel intensity time series from for n is one to five. The circles represent the estimated time lag corresponding to the maximum cross-correlation between pixel intensity time series. The red and dark green dots represent the standard deviation of the time lag.

As shown in Figure 6-3 the waves are propagating landward corresponding to an increasing positive time lag belonging to an increasing value of n. The smaller the value of n, the larger the correlation is as can be seen in the quantity of yellow to red colours plotted in the figure.

Apparently the standard deviation of the lag increases with n, because the distance between the pixels is also ascending with n. With lower values of n, the standard deviation only increases in the surf zone. Because of the breaking of the waves in this zone the correlation between points will decrease quickly especially with a large distance between the points (large value of n). As shown in Appendix E the correlation in the surf zone is very low by increasing value of n, almost no wave signal can be noticed in this region anymore. In the shoaling area still some wave signal is observed by large value of n. A consideration has to be made between a decreasing correlation with increasing n and a smaller weighted standard deviation by increasing value for n, see next section.

Multiple estimates using different step-sizes

The maximum correlation and time lag are estimated from cross correlation of intensity time series in two neighbouring pixels from each point in stack. These neighbouring pixels are situated at both sides of the involved point at a distance of $+n$ times the distance between two pixels and $-n$ times these distance. A value of n of one to 10 is used to calculate the maximum lag in every point. By increasing the step-size n, the maximum lag corresponding to the maximum correlation will also increase because of the increasing distance between the pixels that are applied to calculate the correlation in one point. The reliability will also increase by increasing n because the weighted standard deviation of the lag, that means the standard deviation of the lag divided by the distance between the involved pixels, will decrease. The multiple estimates of maximum correlation and corresponding lag have been combined in a '$\Delta x - \Delta t$' diagram (Figure 6-4). A mean of multiple estimates of the time lag using increasing values of n, weighted with the correlation, will give an estimate of the celerity.

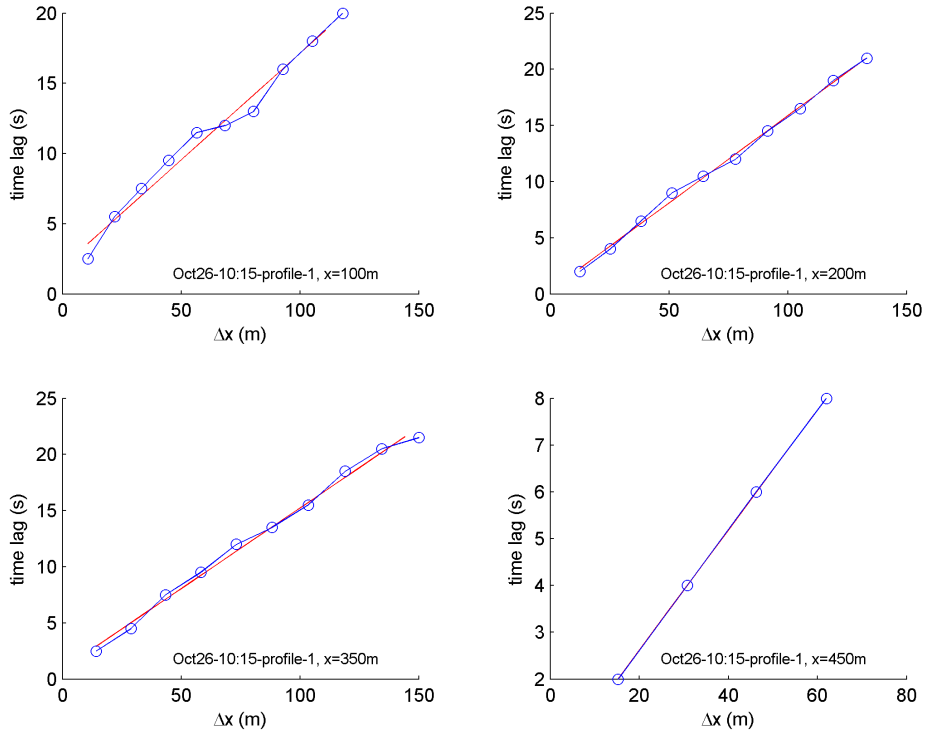

Figure 6-4 $\Delta x - \Delta t$ diagram for four different points in the cross-shore array and increasing value of the step-size n. The circles represent values for step-size n from one to 10. The red line is the polynomial of degree one that fits the data.

Presented in Figure 6-4 is the increasing time lag by increasing step-size n. The steepness of the red line represents the celerity in x-direction at the congruous location. As shown in the figure the circles are clearly situated at a straight line. This means the waves are propagating regularly. Applying the average of the ten estimates of Δx and Δt will give an accurate estimate of the celerity in x-direction.

Estimation of bottom profile from c

The wave phase speed in x-direction is determined by cross-correlation analysis (Eq.(3.22)). After that, applying Snell's law to determine the wave celerity in direction θ and an iteration method including the dispersion relationship result in a final estimate of the bathymetry (see Figure 6-5).

A first estimate of the bottom level is determined using the celerity calculated applying cross-correlation of pixel intensity time series (Eq. (3.14)) and the wave period measured with an offshore buoy. The first estimation of the waterdepth according to Eq. (3.18) in combination with the tidal level z_{tide} results in a first estimate of the bathymetry:

$$z_b = z_{tide} - h \tag{3.35}$$

The celerity in the direction of θ will be applied to determine a final estimate of the bathymetry. Therefore Snel's law (Eq. (3.15) and (3.16)) has to be employed to calculate the angle of incidence θ at depth h and the celerity c. The offshore angle of incidence is needed as input in Snel's law as well as the offshore celerity which is determined by applying the dispersion relationship (Eq. (3.18)) using the offshore waterdepth (21 m) and the relation denoted in Eq. (3.20). The celerity in the direction of θ is also needed as input in Snel's law. This celerity c is estimated applying Eq. (3.20) and (3.18) by using the bottom level according to Eq. (3.35). Finally these parameters can be inserted in Snel's law (Eq. (3.15) and (3.16)) to result in the celerity in the direction of θ.

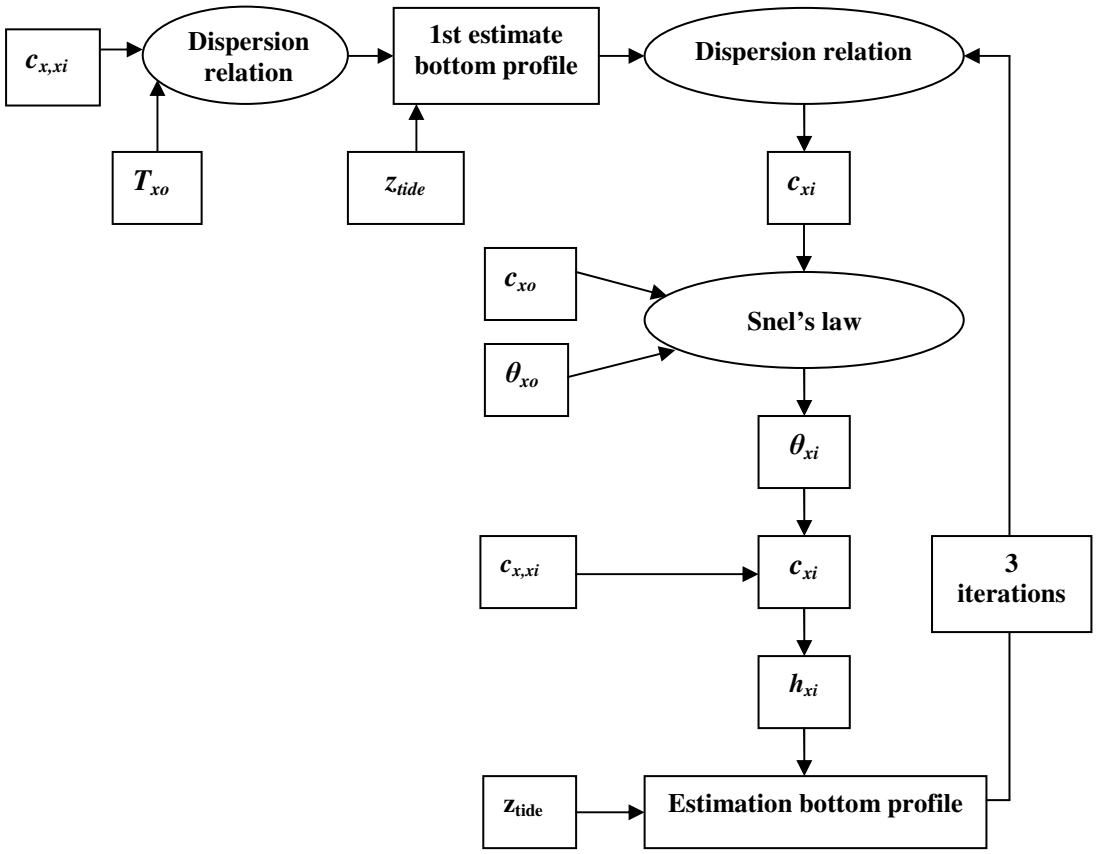

Figure 6-5 Iteration estimation bottom profile. c means wave celerity, T wave period, z_{tide} is tidal level, θ is angle of incidence, h is waterdepth. xi means location from x=0 to x=400m, xo means offshore location.

Next Eq. (3.20) can be applied again to obtain a better estimate of the wavenumber after which the dispersion relation leads to a final estimate of the water level and bathymetry by Eq. (3.18). Than again Snel's law can be applied to create a better estimate of θ and the waterdepth. Repeating this iteration results in a better estimate of the bathymetry.

The iteration described above is repeated three times for every cross-shore array. This is implemented for different timestacks (data at half hourly intervals) and the results of several timestacks in a day are averaged over time. A smoother bottom profile has to be expected by determining a celerity and bottom profile using different values of the step-size n instead of using one value of n. Namely the celerity is than averaged over more estimates for one point in the array applying the '$\Delta x - \Delta t$' diagram (Figure 6-4). A mean of multiple estimates of the

time lag using increasing values of *n*, weighted with the correlation, will give an estimate of the celerity. From this estimate a bathymetry is determined.

To smooth the obtained bathymetry a running mean is applied. This running mean consists of a filter and is used to arrive at smoother estimates of local bathymetry. This filter has a depth-dependent length of 10 times the depth. A final estimate of the bathymetry is shown in Figure 6-6.

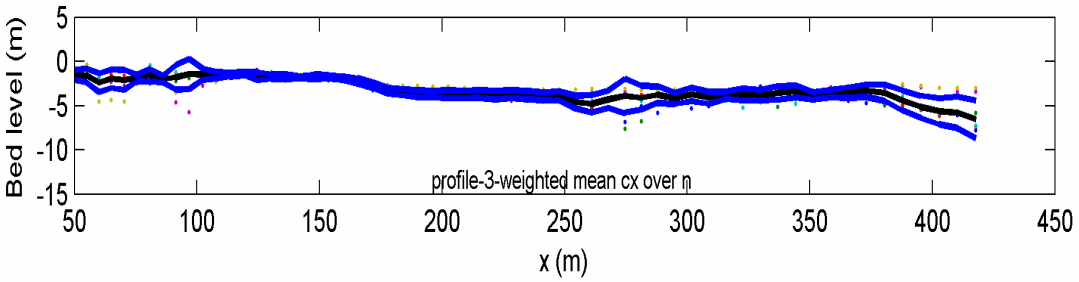

Figure 6-6 Bed level calculated using a weighted mean celerity applying a depth-related filter and 6 timestacks of 17 minutes. The black line represents the bottom level and the blue lines represent the standard deviation of the bed level. The small coloured dots reflect the estimates belonging to the different timestacks.

The bed level estimated in Figure 6-6 shows a realistic bathymetric course. The smallest standard deviation is found in the surf zone and shoaling region to about 350 m. Outside this area a broader error band can be noticed. This may be explained by the fact that these points are situated at increased distance from the camera. The broader error band may be a consequence of the decrease of pixel resolution with distance. In the transition zone from *x* is 250 to 280 m the error band is also broader probably because of the change in intensity signal from dark wave front to light breaking wave front.

To validate the estimated profile, the bed level is compared to a measured profile obtained from a JARKUS survey of July 2005 (see Figure 6-7). From this figure, we can observe that the estimate in the intertidal area is situated much lower than the measured profile. In that area not one distinct measure of wave celerity is present, therefore we cannot derive a good estimate of the bathymetry in that area. The height of the first bar (x=150m) is estimated accurately, however the profile is shifted in horizontal position. An explanation for this is that this bar is situated in a dynamic region and moreover the long-shore position of the measured and estimated profiles is not exactly the same. In the remaining part of the figure, the shape of the measured profile is approximated very well by the estimated profile, however an offset downward exists. This can be caused by the fact that the waveheight is not included in the estimation of the bed level yet. In this study we have applied an estimated mean wave period based on the time lag between two maxima in the correlation diagram. This period is estimated to have a value of 8 s. However, if a period is estimated from the actual time lag more accurately (on each cross-shore location), a better estimate of the bottom profile might be made.

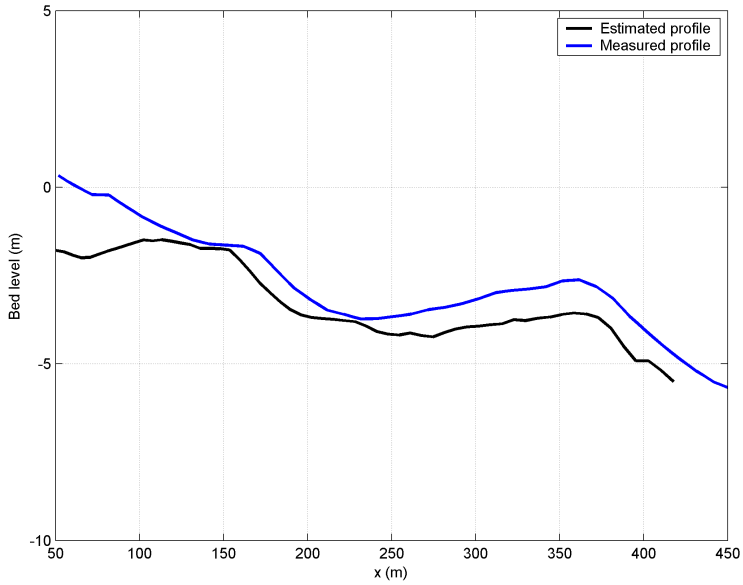

Figure 6-7 Estimated bed level (black) and measured profile (blue). The estimated profile is located on y=-300m, the measured profile on y=-250 m.

6.4 Group wave phase speed

Instead of determining the individual wave phase speed from pixel intensity time series also the group celerity can be determined. It is expected that the smoother group signal will result in a less spiked bathymetry estimate. Therefore the original intensity signal has to be translated in a signal corresponding to the phase speed of a group of waves. This will be described in the following part. Also some operations are performed to improve the results of the estimate of the time lag and bottom level.

Envelope and filter

Just as with the individual wave signal a high-pass filter is applied to smooth the original intensity signal and frequencies lower than 0.05 s^{-1} are therefore eliminated. Subsequently a low-pass filter is applied that reject frequencies above 0.5 s^{-1}. The intensity signal is divided by its standard deviation to equalize the intensity of the signal over the whole length of the cross-shore array. After that a Hilbert transform is employed to obtain the envelope of the intensity time series. The intensity signal is squared to correspond to the elevation (Eq. (3.30)), assuming that the intensity is proportional to the wave slope. A lot of high frequency noise is noticed in the signal of the envelope. Therefore a low-pass filter is applied and frequencies above 1.5 times the peak frequency are rejected.

Accuracy

Before examining the results the data were screened. Only onshore phase speed would be used in the estimation of water depth. In the coordinate system defined for Egmond aan Zee a wave moving toward the shore would be moving in a negative *x*-direction corresponding to a positive lag. The celerity and depth estimates are thus limited to those instances where the lag is positive.

Just as with the individual celerity the stacks are divided into three sub-samples of the same length. For every sub-sample of the signal the maximum lag is determined for each point in the array and the median lag is determined. Large spreading of width in the maximum correlation is observed. Also the maximum lag can not be determined accurately for points having a much lower maximum correlation. Therefore a lag corresponding to a maximum correlation lower than 0.35 times the maximum correlation in the sub-sample is left out of consideration. Error bands are determined from the multiple estimates from sub-samples in the time stack. When the standard deviation divided by the median lag is higher than 0.5, the estimate is unreliable and therefore no lag and group celerity will be determined for these points.

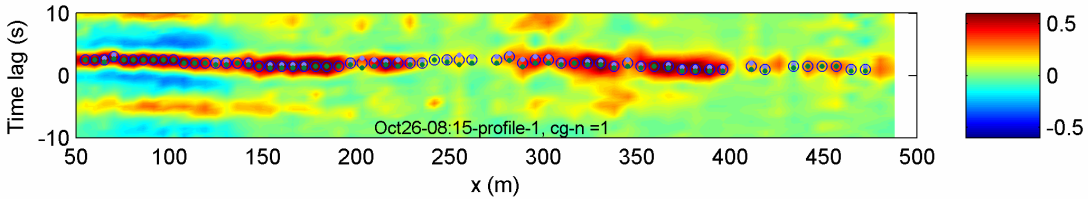

Figure 6-8 Correlation against time lag for pixel intensity time series from *x*=50 to *x*=500 and *n* = 1. The circles represent the estimated time lag corresponding to the maximum cross-correlation between the envelope of pixel intensity time series. The blue and dark green dots represent the standard deviation of the time lag.

Not one single lag can be indicated corresponding to the maximum correlation as shown in Figure 6-8. In comparison to Figure 6-1 corresponding to the individual wave signal, the correlation using the envelope of the signal does not have a clearly visible peak but a broad high correlation band belonging to different values of the lag. An explanation for this purpose is perhaps the longer wave signal of the envelope in comparison to the individual wave signal. Consequently the peaks in this signal are broader resulting in a broader correlation band by comparing two signals. Moreover, by increasing the value of the step-size *n,* a strong decrease of the correlation can be noticed (Figure 6-8 and Figure 6-9). Therefore, the group celerity is only determined using a value of *n* of one because in that case it is possible to define a lag matching with the maximum correlation (Figure 6-8).

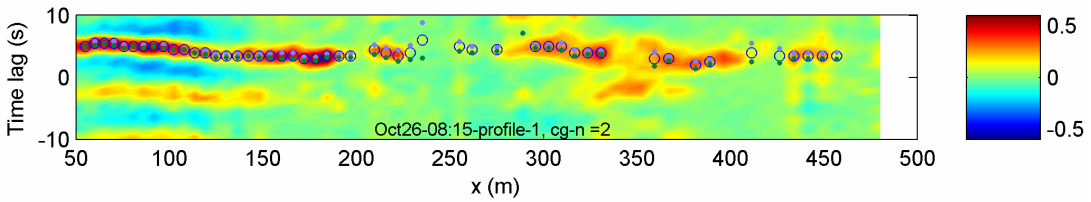

Figure 6-9 Correlation against time lag for pixel intensity time series from *x*=50 to *x*=500 and *n* = 2. The circles represent the estimated time lag corresponding to the maximum cross-correlation between the envelope of pixel intensity time series. The blue and dark green dots represent the standard deviation of the time lag.

According to Figure 6-8, strong correlation can be noticed in the shoaling region and the surf zone. In the transition area the correlation is weaker. This is probably caused by the change in intensity signal from dark wavefront to light breaking wavefront. The maximum correlation decreases strongly at a distance of $x > 400$ m. As with the celerity, this may be explained by a decrease of pixel resolution at distance from the camera.

Estimate of bottom profile from c_g

Estimation of a bottom profile out of the group celerity is not possible in the same way as with the individual celerity, because the wavenumber can not be determined directly. Nevertheless a first estimate of the bottom level is needed to apply Snel's law (Eq. (3.15) and (3.16)) for determining the group celerity from the group celerity in x-direction. To separate the calculations performed with the original intensity signal and the envelope of this intensity signal, we do not use the estimated bathymetry from c as a first estimate for our iteration. Instead, we choose to use an idealized profile (straight line from x=0 to x=970 m and z=0 to z=8 m). Further investigation is needed if the results will be better if the profile calculated in Chapter 6.3 is used.

After creating a first estimate of the bottom profile the dispersion relationship formulated in Eq. (3.18) is applied to determine the offshore wavenumber. Subsequently the offshore celerity according to Eq. (3.20) is calculated. Using Eq. (3.15) and (3.16) the group celerity can be determined from the group celerity in x-direction and the angle of incidence at a specific point.

Again, an estimate of the bottom profile has to be generated from the group celerity without knowing the wavenumber. Therefore, first a temporary array of the waterdepth is created with the range of possible values of h from zero to 50 meters. Applying the dispersion relationship according to Eq. (3.18), the relation between this h and the wavenumber k can be created. By applying Eq. (3.17), this results in an estimate of the group celerity dependent to the waterdepth. This is shown in Figure 6-10.

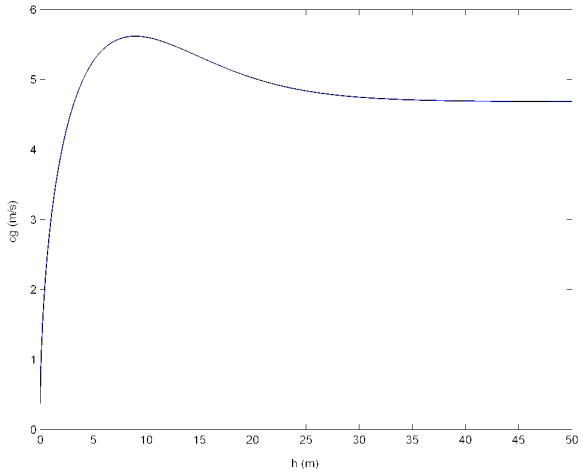

Figure 6-10 Group celerity in relation to the waterdepth

Because the cross-shore array of pixels to be analysed is located in shallow water it is assumed that the waverdepths are situated in the ascending line of the curve. Supposing that, using the group celerity determined by cross-correlation according to Eq. (3.14) a corresponding waterdepth can be observed. Another advantage of using the ascending line of the curve instead of the descending line is the smaller error band in the estimate of the waterdepth h. Namely in the first part of the curve a large change of the group celerity results in a small change of the corresponding waterdepth according to the curve whereas a large change in the group celerity results in a very large change in the waterdepth applying the second part of the curve. Applying this curve results in a first estimate of the bottom level and by iteration a smoother approximation can be generated.

According to Figure 6-10 a group celerity larger than the peak in the curve can not occur. However the group velocity calculated using cross-correlation analysis does sometimes exceed the maximum estimated group velocity according to Figure 6-10. It is therefore not possible to determine a corresponding waterdepth for these points.

To investigate the accuracy of the estimated group celerity and corresponding lag determined by applying the cross-correlation method a numerical approach of the group celerity is performed by calculating backwards starting at a bathymetry. The estimate of the bottom profile from Chapter 6.3 is used to calculate the water depth. Applying the dispersion relation (Eq. (3.18)) and a known angular frequency the corresponding wavenumber is determined. The group celerity is calculated using the expression stated in Eq. (3.17). Knowing the locations of the pixels in the array, the time lag can be solved from Eq. (3.14). This results in a time lag that differs from the time lag determined by cross-correlation of the envelope of the pixel intensity signal. As shown in Figure 6-11 the time lag increases by increasing x and as a result the time lag is larger in the shoaling region than in the surf zone. The distance Δx between the pixels i and j at which the correlation is calculated also increases by increasing x. But because the lag belonging to the maximum correlation also increases a smaller group velocity is noticed as calculated by applying the cross-correlation method. This smaller group velocity can be applied to Figure 6-10 and a corresponding waterdepth is found. This means the lag calculated by cross-correlation of the envelope of intensity time-series is not reliable yet.

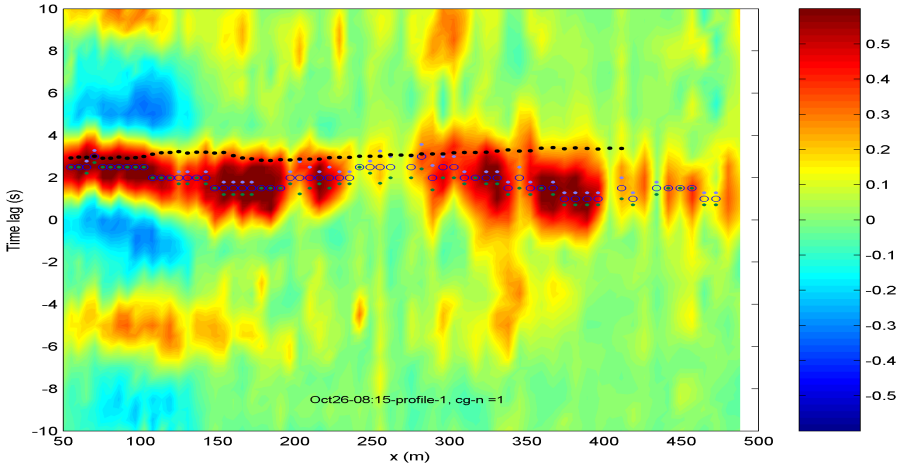

Figure 6-11 Correlation against time lag and from x=0 to x=500 m corresponding to the envelope of the pixel intensity time series. The circles represent the estimated time lag by cross-correlation of pixel intensity time series and the black dots represents the numerical calculated time lag fro m an bathymetry.

As a result of the determined group velocity no corresponding bottom level can be calculated. Therefore it is recommended to investigate the method for estimating the correlation and time lag out of an envelope of the intensity signal. The group celerity and the relation to the underlying bathymetry have to be investigated further as well.

6.5 Synthesis

A new technique has been developed for the estimation of wave celerity and bathymetry from remote pixel intensity time series applying cross correlation analysis. The measurement of wave phase speed and associated water depths made at a series of cross-shore positions is providing a cross-shore profile of beach morphology. These remotely collected profiles may create a longterm record of the large-scale morphology changes at a particular site.

The video-based technique to estimate celerity using a cross-correlation was shown to be most accurate when the mean of the estimates of several timestacks in a day at one particular cross-shore position was chosen as a representative single water depth. A mean of multiple estimates of the time lag using increasing values of the step-size between neighbouring pixels, weighted with the correlation, gives an estimate of the celerity. A running mean (filter window is several meters cross-shore) is a good instrument to arrive at smooth estimates of the local bathymetry.

Applying the envelope of the pixel intensity signal, i.e. the group signal, strong cross-correlation was found in the shoaling region and the surf zone. In the transition area the cross-correlation is weaker. So far the underlying bathymetry cannot be derived from the group celerity despite of the correlation and time lags determined between the envelope of pixel intensity time series.

Errors in the estimate of bathymetry from wave celerity may occur due to inaccuracies in the linear dispersion relation. Phase speeds in the nearshore can be affected by many physical processes such as surface drift currents, mean flows and rip currents (Plant and Wright, 1980), the directional spread of wave energy (Huang and Tung, 1977) and the presence of shorter travelling waves on low-frequency long waves (Phillips, 1981).

7 Discussion

7.1 Introduction

In the preceding chapters the applicability of two different methods to estimate wave characteristics from video has been investigated. The Optical Wave Model is applied to calculate a directional wave spectrum resulting in wave period and direction (Chapter 5) and cross-correlation analysis is used to determine the wave celerity and corresponding bathymetry (Chapter 6). From Chapter 5 and 6 some doubts can be cast on the applicability of the different methods to determine wave characteristics with data from the Dutch coast. In this section the main findings of this thesis will be discussed and a further look will be taken at the applicability of the theories to derive wave characteristics from video.

7.2 Applicability of optical wave techniques

The dynamic nearshore system is driven by energy from ocean waves propagating into the nearshore domain after generation at sea. Specifications of this incident wave forcing will help to understand dynamics in the nearshore zone. Therefore for improving the nearshore science, long-term data sets of wave characteristics are required. It was assumed that images from video cameras can be of great help to collect wave data and bathymetric information. During the field experiment in Egmond aan Zee (Chapter 4.3) it was noticed that both video system and in situ instruments are sensitive to breakdown. However, if the video system is working properly, it is able to collect data automatically and on a long-term basis, and is much less labour-intensive than applying mini tripods in the nearshore zone. Besides, a lot of optical instruments applied on different locations in the view of the camera can be used to collect data by applying a video system. This means a much higher spatial coverage can be realised. Because of breakdown of instruments, the resulting dataset applied in this research consists of 43 good quality timestacks and concurrent in situ measurements. Anyway it is therefore recommended to carry out another field experiment to provide more data.

A technique to derive directional wave spectra (Holman and Chickadel, 2004) and a spectral technique to estimate wave phase speed (Stockdon and Holman, 2000), has already been successfully applied to the coast of the USA. In this work, the application of two theories using pixel intensity time series to obtain wave characteristics at the Dutch coast has been investigated. Therefore the central aim of this project was to apply and assess applicability of these different theories to estimate wave characteristics from video imagery with data from the Dutch coast.

It can be concluded from the foregoing chapters, that the different circumstances along the coast of the USA and the Dutch coast result in different experiences. This means that the methods that have been successfully applied to the coast of the USA cannot directly be applied to the Dutch coast. The North Sea wave conditions representing a broad wave spectrum differ from the swell-dominated spectra usually found at the coast of the USA. As

a result the North Sea wave spectra are not necessarily single-peaked; hence the peak in the spectra cannot be applied to determine wave characteristics. Attention should be paid to the differences in the shape of the spectra between the sites around the world, which ask for other analysing methods of the pixel intensity signal. Moreover it is recommended to investigate if the methods used in this work are also applicable to different sites around the world.

In Figure 2-6 it is mentioned that a strong correlation exists between a time series of pixel intensities and the wave height signal obtained from a wave gauge at the same location (Lippmann and Holman, 1991) at Duck, USA. The theory to derive wave characteristics from video imagery is based on this assumption that optical radiance from the ocean surface is representative of the sea surface. Because of the different findings compared to the USA from the optical measurement of directional spectra as stated in Chapter 5, a similar figure is made from data collected along the Dutch coast. This is shown in Figure 7-1. It can be concluded that the relation between intensity signal and surface elevation is weaker at the location of the instruments used in this study. From these figures it can be observed, that a strong correlation between wave height and time series of pixel intensities (as shown in Figure 2-6) is not always present. This might cause the relatively low correlation found between in-situ and optical signals in this study.

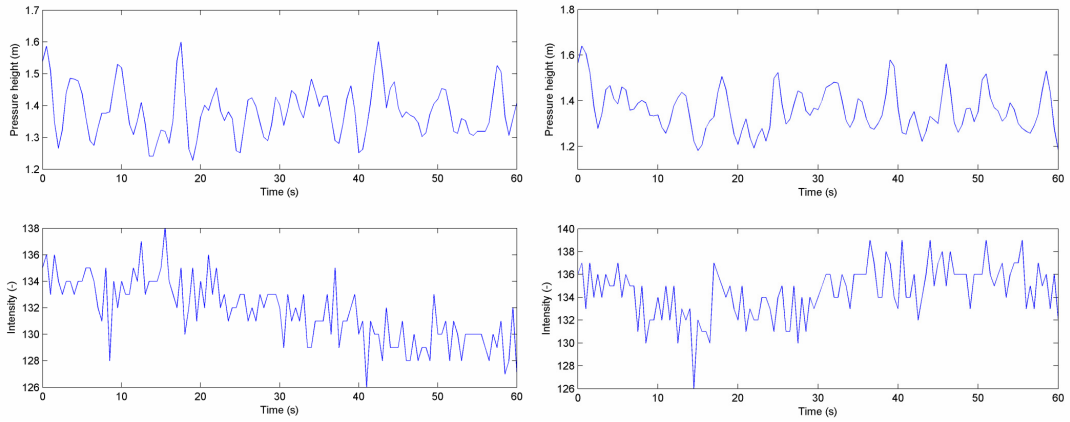

Figure 7-1 Relation between time series of pixel intensities and a wave height measured by a pressure sensor sampled from Egmond aan Zee (NL), for two different time series on October 21st, 2005 15:15 Hrs.

Performance of video imaging of waves is degrading with increased distance from the camera and with increased viewing angle. This is probably a consequence of the decrease of pixel resolution with distance from the camera. Further research is needed to investigate this degradation of performance with distance from the camera.

Certain wave conditions are more favorable for use with video technique. A clean narrow-banded swell as in the USA makes the identification of a peak frequency rather obvious. A broad-banded or directionally spread spectrum, as found during the field experiment in Egmond aan Zee, is likely to degrade the Fourier analysis and makes it difficult to resolve the frequency of interest. It is recommended to investigate the methods to derive wave characteristics from video during different conditions, for instance after and during a storm (periods with increasing and decreasing wave height). Therefore, a field experiment has to be performed for a longer period collecting stacks. On the other hand, weather situations like rain, fog and poor lighting conditions obscure the visual signature of the waves. Sun

glare can add large amounts of noise. Research is needed to determine the influence of these weather conditions on the pixel intensity time series data analysis.

7.3 Discussion on the Optical Wave Model

In Chapter 5, the interpretation of video observations to estimate wave period and wave direction, the Optical Wave Model (Holman and Chickadel, 2004) has been discussed. This model is applied to calculate the directional spectrum $S(f, \theta)$ from video. Some adjustments are introduced in this work to improve the results for the dataset along the Dutch coast. Holman and Chickadel presumed that variations in optical radiance due to waves are related to variations in sea surface slope (yielding a wavenumber dependency). In this work, also a theory is used that assumes the intensity to be proportional to the surface elevation. Two different methods are therefore applied to calculate the frequency and directional spectrum, i.e. weighting over k^{-2} and without weighting over k^{-2}. The first method presumes a relation between intensity and slope of the waves while the second method supposes that the intensity is related to the surface elevation.

Determining the period over the spectrum between 2 and 9 s, the method without weighting corresponds the most to the in situ spectrum for the instruments in the intertidal area. For the instruments in the shoaling region, the periods calculated by weighting over k^{-2} give a better correlation to the in situ periods than without applying the weighting. The difference in relation between real waves and the accompanying intensity signal in the intertidal area and the shoaling region is probably caused by the change in intensity signal from dark wave front to light breaking wave front as shown in the timestack in Figure 7-2. This change occurs in the transition zone and is reflected by the white foam patches from x=0 to x=150 m. The instruments in the intertidal area are located at around x=30 m where the white foam represents the dissipation of roller energy. This energy of the white foam breakers corresponds to the wave energy and the wave height. Therefore the intensity signal can be assumed to be proportional to the surface elevation. Wave crests approaching the shore without breaking show dark bands in the timestack, which represent the sea surface slope.

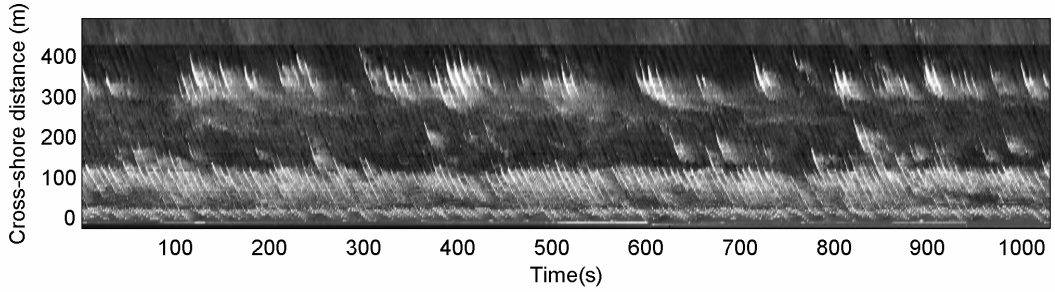

Figure 7-2 Example of a time stack image sampled along a cross-shore array at Egmond aan Zee (NL), October 26th 2005, 8:15 Hrs. The cross-shore array is distributed over three cameras. The transitions between the cameras are at x=90 and x=430 m. This explains the change in intensity in the band in the top of the figure. The dark bands represent the non-breaking wave fronts and the white bands reflect the foam of the breaking waves.

Generally, the comparisons between video wave period and in situ wave period made in Chapter 5 are quite promising. The value of the period in each spectrum appears accurate within a few tenths of seconds. As opposed to the results obtained by Holman and Chickadel

(2004), the location of the peak in each spectrum is not well defined. But applying the T_{m01} accurate results are generated that are promising for further research. However some remarks can be given. The optical spectra represent a rather large spatial area (order 10 by 20 m in the intertidal area) as opposed to the point measurement obtained from the in situ instruments. This can introduce discrepancies between the video and in situ results.

Considering the wave direction, the results are much less reliable. The present accuracy of these results is not good enough to use the technique as an actual measuring device to measure wave direction. The measuring devices applied to the mini tripods are located under the water level thus measuring the waves inside the water, where the water is also influenced by longshore currents and undertow. However, the optical signal measured at the surface is significant different from the in-situ signal obtained deeper in the water. The difference in measurement location between video instrument and in-situ instrument can cause discrepancies in the results between optical wave direction and in situ wave direction. In future studies this effect should be taken into account.

It is recommended to examine the wave direction from video in the shoaling region as well as in the intertidal area, because there the waves will not always approach perpendicularly but are still subject to refraction. Different values of the wave direction will then be noticed and an extended comparison with the in situ data can be made. Further work is needed to investigate the applicability of the wave direction derivation method from video by analysing more data runs.

7.4 Discussion on cross-correlation analysis

In Chapter 6 the determination of wave celerities in the time domain, applying cross-correlation of remotely collected intensity data has been discussed. Subsequently, the determination of wave phase speed and associated water depths inferred from linear wave theory made at a series of cross-shore positions provides a cross-shore profile of beach morphology. These remotely collected profiles create a long-term record of the large-scale morphology changes at a particular site.

The raw pixel intensity time series are filtered with a high- and low-pass filter to remove respectively low-frequency trends and noise. The cut-off frequencies in this filter are based on experiences and not examined thoroughly. In further research it is recommended to investigate the influence of different cut-off frequencies of the filter more extensively.

A mean of multiple estimates of the time lag using increasing values of the step-size between neighbouring pixels, weighted with the correlation, gives an estimate of the celerity. The video-based technique to estimate celerity using cross-correlation was shown to be most accurate when the mean of the estimates of several timestacks in a day at one particular cross-shore position was chosen as a representative single water depth. A running mean (filter window is several meters cross-shore) is a good instrument to arrive at smooth estimates of the local bathymetry. The bed level is estimated from the celerity in x-direction by a threefold iteration starting with an estimate of the bottom profile from c_x (see Figure 6-5). However, a better estimate from the celerity in x-direction could possibly be derived by increasing the number of iterations. This should be investigated in a further research.

The bed level estimated from cross-correlation show a realistic bathymetric course. However, it is recommended to compare these profiles with survey data from for example Jarkus data for ground truthing. In the estimated profiles in the transition zone a broader error band is noticed than in the shoaling area and intertidal zone, probably because of the change of intensity signal from dark wavefront to light breaking waves as shown in Figure 7-2. Likewise a broader error band is noticed with increased distance from the camera, which again asks for further investigation of the degradation of performance with distance from the camera.

Applying the envelope of the pixel intensity signal, i.e. the group signal, strong cross-correlation was found in the shoaling region and the surf zone. In the transition area the cross-correlation is weaker (change in intensity signal). So far the underlying bathymetry cannot be derived from the group celerity despite of the correlation and time lags determined between the envelope of pixel intensity time series. Therefore research is needed to further investigate if it is possible to apply the envelope of the intensity signal for determining the wave phase speed and bathymetry.

Moreover, it is recommended to investigate if wave period and direction information can be determined from the cross-correlation analysis. The wave period could probably be reflected by the distance between two successive minimum or maximum lags. Direction information could probably be derived by applying a number of cross- and longs-shore arrays in the analysis.

Phase speeds in the nearshore can be affected by many physical processes such as surface drift currents, mean flows and rip currents (Plant and Wright, 1980), the directional spread of wave energy (Huang and Tung, 1977) and the presence of shorter travelling waves on low-frequency long waves (Phillips, 1981). Therefore, errors in the estimate of bathymetry from wave celerity may occur due to inaccuracies in the linear dispersion relation.

8 Conclusions and recommendations

8.1 Conclusions

- A strong correlation between wave height and time series of pixel intensities is not always present.

Wave period and direction from video

The following conclusions can be made from the directional spectra analysis:

- The Optical Wave Model to derive directional wave spectra can be applied to the Dutch coast. The frequency spectrum has to be considered between 0.11 and 0.5 Hz.

- Wave period is best estimated from video by T_{m01}. The broad-banded spectrum along the Dutch coast result in a spectrum that is not single-peaked, hence T_{peak} is not well defined.

- The optical frequency spectrum using the method without weighting over k^{-2} shows the best correlation with the ground-truth data for the intertidal area. Therefore the intensity in the intertidal area seems proportional to the elevation.

- In the shoaling region further away from the camera the intensity corresponds to the slope of the waves and weighting over k^{-2} have to be applied to receive the best results.

- Overall: poor correlation for wave direction, at least partly attributed to complex beach topography and limited dataset.

- Wave direction is best estimated from video by the weighted mean direction.

- Correlation increases by only applying data collected during high water.

Wave celerity from video

Conclusions from the estimation of wave phase speed and corresponding bathymetry applying cross-correlation analysis:

- A mean of multiple estimates of the time lag using increasing values of the step-size between neighbouring pixels, weighted with the correlation, gives an estimate of the celerity.

- A running mean (filter window is several meters cross-shore) is a good instrument to arrive at smooth estimates of the local bathymetry.

- It is possible to derive a wave phase speed and realistic bed level by cross-correlation of intensity time series.

8.2 Recommendations

- Carry out another field experiment to provide more days with data, probably on a location with a less complicated morphology.

- Further investigation is needed if the method used in this work is also applicable to other sites.

- Further work is needed to investigate the degradation of performance with distance from the camera.

- Rain, fog and poor lighting conditions all obscure the visual signature of the waves. Sun glare can add large amounts of noise. Research is needed to determine the influence of this on the pixel intensity time series data.

Wave period and direction

- Research should be done to investigate if intensity is proportional to the surface elevation or to the wave slope.

Wave celerity

- Further research is needed to get better insight in the influence of the numbers of sub-sections a time stack is divided.

- Research is needed to determine the influence of more or less iterations to derive the bottom profile from celerity.

- Research should be done to improve the effect of the filter and the cut-off frequency applied in the filter.

- Research is needed to the method calculating the lag corresponding to the maximum correlation of the envelope signal. The group velocity determined from cross-correlation should be investigated and the relation to the underlying bathymetry. Also another first estimate in the iteration of the bottom profile may be applied.

- It would be wise to compare the bathymetric data obtained by cross-correlation analysis with survey data from for example Jarkus data for ground truthing. Also these results can be compared with the spectral method applied by Stockdon and Holman to calculate bathymetry from video imagery.

- The extent of inaccuracies in the linear dispersion relation resulting in errors in the estimated bathymetry should be investigated in further research.

- The waveheight should be included in the estimation of the bed level from cross-correlation analysis in future studies.

- The applicability of deriving wave period and wave direction from cross-correlation analysis of cross- and longshore pixel intensity time series has to be studied.

- In future studies, the period used in the calculation of the bottom profile from celerity should be estimated from the actual time lag (on each cross-shore location) from the cross-correlation analysis.

A Geo-referencing of oblique video data

Standard photogrammetric procedures enable the transformation from real world coordinates to image coordinates on the basis of the collinearity equations. These contain the coefficients L1 to L11 which are described as

$$
\begin{aligned}
L &= -\left(x_c m_{31} + y_c m_{32} + z_c m_{33}\right) \\
L_1 &= \frac{\left(u_0 m_{31} + f m_{11}\right)}{\lambda_u L} \\
L_2 &= \frac{\left(u_0 m_{32} + f m_{12}\right)}{\lambda_u L} \\
L_3 &= \frac{\left(u_0 m_{33} + f m_{13}\right)}{\lambda_u L} \\
L_4 &= -\left(L_1 x_c + L_2 y_c + L_3 z_c\right) \\
L_5 &= \frac{\left(v_0 m_{31} + f m_{22}\right)}{\lambda_v L} \\
L_6 &= \frac{\left(v_0 m_{32} + f m_{22}\right)}{\lambda_v L} \\
L_7 &= \frac{\left(v_0 m_{33} + f m_{23}\right)}{\lambda_v L} \\
L_8 &= -\left(L_5 x_c + L_6 y_c + L_7 z_c\right) \\
L_9 &= \frac{m_{31}}{L} \\
L_{10} &= \frac{m_{32}}{L} \\
L_{11} &= \frac{m_{33}}{L}
\end{aligned}
\tag{3.1}
$$

In the above equations, (x_c, y_c, z_c) are the camera *xyz*-coordinates, (u_0, v_0) are the image center *uv*-coordinates, f is the effective focal length and λ_u and λ_v are the horizontal and vertical scale factors. The *m*-coefficients describe the successive rotations around azimuth ϕ, tilt τ and roll σ.

$$
\begin{aligned}
m_{11} &= \cos\phi\cos\sigma + \sin\phi\cos\tau\sin\sigma \\
m_{12} &= -\sin\phi\cos\sigma + \cos\phi\cos\tau\sin\sigma \\
m_{13} &= \sin\tau\sin\sigma \\
m_{21} &= -\cos\phi\sin\sigma + \sin\phi\cos\tau\cos\sigma \\
m_{22} &= \sin\phi\sin\sigma + \cos\phi\cos\tau\cos\sigma \\
m_{23} &= \sin\tau\cos\sigma \\
m_{31} &= \sin\phi\sin\tau \\
m_{32} &= \cos\phi\sin\tau \\
m_{33} &= -\cos\tau
\end{aligned}
\qquad (3.2)
$$

The theoretical formulations presented here are valid for use with distortion-free lenses. Owing to the incorporation of λ_u and λ_v, the formulations embody a correction for the slightly non-squareness of individual pixels. The latter is induced by a minor difference in sampling frequency between the camera and image acquisition hardware, which causes a minor mismatch between the number of horizontal picture elements at the camera CCD and the number of columns at the image frame buffer, where the image processing stores the video data.

B Fieldwork equipment and data

B.1 Fieldwork measuring equipment

During the field tests equipment is used from the laboratory of physical geography of the University of Utrecht. Four mini tripods are used to measure the water velocity, sediment concentrations and wave height. With a DGPS (Differential Global Positioning System) the intertidal beach is measured every day during the six weeks of field tests. The equipment will be described in the next paragraphs.

B.1.1 DGPS

A Differential Global Positioning System (DGPS) is used to measure the morphology of the intertidal beach. The beach is surveyed every day during the field tests from about x=100 m to x=600 m.

The DGPS measures the bathymetry with a high accuracy. It consists of two GPS receivers. The first GPS receiver (the base) is placed at a known position. This position is at the Rijkswaterstaat cabin on the beach of Egmond aan Zee. The second GPS receiver (the rover) measures the coordinates of the unknown points. The base GPS receiver can calculate the error of a normal GPS measurement, because its position is already known. The difference between the measured and known position is the correction and the correction is transmitted by a radio to the rover. The correction is applied on the GPS measurement of the rover. The accuracy of the DGPS measurement is in a range of 2.5 cm horizontal and 4 cm vertical.

B.1.2 Mini tripod

The mini tripod is a small (about 2.0 m wide) instrumented tripod that can be deployed by hand in the intertidal area on the beach. Instruments include a pressure sensor (measures waterlevel), three optical backscatter sensors (OBS) (measures sediment concentration), and an electromagnetic flow meter (EMF).

Figure 8-1 Mini tripod including pressure sensor, optical backscatter sensors and an electromagnetic flow meter

The instruments are connected to a PVC container. The central element in this container is a data logger, which measures the signals from the instruments and controls their power supply. A battery pack inside the container provides the power supply for the data logger and the instruments. The capacity of the battery pack is enough for 20 days of continuous measurements. The mini tripod is stabilized by 10 kg of lead on each leg and an anchor to prevent drift during storms. A float is attached on the frame to ensure that data is collected at the moment the frame is under water and that the instruments will switch off when the frame is not under water.

The use of tripods has advantages over other methods like ships, boys and poles:
- Measurements with a total duration of more than a month, covering spring-neap tide cycle.
- The use of ships is too costly for such prolonged periods.
- Flexible in positioning. Opposite to the use of poles, it's simple to reallocate the tripods to another position.
- Tripods can be placed in shallow water, where ships wouldn't be able to come at low tide.
- Able to measure under extreme weather conditions.

The main drawbacks of the use of tripods are:
- No direct feedback on the proper operation of the tripods.
- The need for large amounts of batteries for powering the electronics.
- Vulnerable to (fishing-) ships.

Every day at low tide the beach is surveyed with the DGPS and the measured data stored at the data logger in the mini tripod are read out using a laptop. After that the data logger is activated again. During high tide the mini tripods are again covered by water and new measurements can be made.

B.2 Pixel instrument

In Figure 8-2 an alpha array located at the intertidal beach is shown. An alpha array consists of 17 pixels. Array a-246.37 is the most seaward array at the intertidal beach corresponding to the most seaward miniframe.

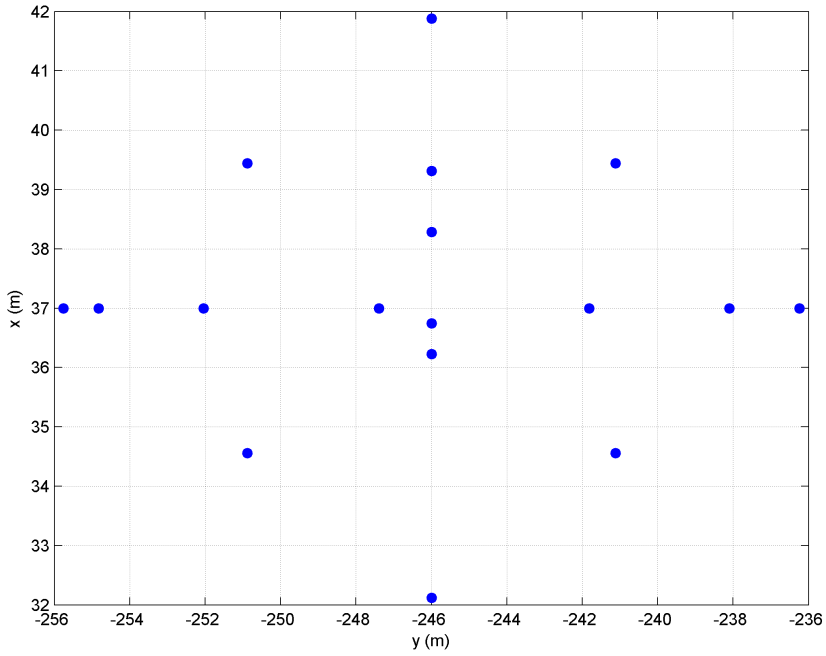

Figure 8-2 Alpha array a-246.37

B.3 Data selection

The timestacks applied in this work are stated in the following table:

1129898702.Fri.Oct.21_12_45_02.GMT.2005.egmond.c1.stack.ras
1129900501.Fri.Oct.21_13_15_01.GMT.2005.egmond.c1.stack.ras
1129902302.Fri.Oct.21_13_45_02.GMT.2005.egmond.c1.stack.ras
1129904102.Fri.Oct.21_14_15_02.GMT.2005.egmond.c1.stack.ras
1129905901.Fri.Oct.21_14_45_01.GMT.2005.egmond.c1.stack.ras
1129907702.Fri.Oct.21_15_15_02.GMT.2005.egmond.c1.stack.ras
1129909501.Fri.Oct.21_15_45_01.GMT.2005.egmond.c1.stack.ras
1130314501.Wed.Oct.26_08_15_01.GMT.2005.egmond.c1.stack.ras
1130316302.Wed.Oct.26_08_45_02.GMT.2005.egmond.c1.stack.ras
1130318101.Wed.Oct.26_09_15_01.GMT.2005.egmond.c1.stack.ras
1130319901.Wed.Oct.26_09_45_01.GMT.2005.egmond.c1.stack.ras
1130321701.Wed.Oct.26_10_15_01.GMT.2005.egmond.c1.stack.ras
1130323501.Wed.Oct.26_10_45_01.GMT.2005.egmond.c1.stack.ras
1130325301.Wed.Oct.26_11_15_01.GMT.2005.egmond.c1.stack.ras
1130327101.Wed.Oct.26_11_45_01.GMT.2005.egmond.c1.stack.ras
1130328901.Wed.Oct.26_12_15_01.GMT.2005.egmond.c1.stack.ras
1130330701.Wed.Oct.26_12_45_01.GMT.2005.egmond.c1.stack.ras
1130332501.Wed.Oct.26_13_15_01.GMT.2005.egmond.c1.stack.ras
1130334301.Wed.Oct.26_13_45_01.GMT.2005.egmond.c1.stack.ras
1130336101.Wed.Oct.26_14_15_01.GMT.2005.egmond.c1.stack.ras
1130337901.Wed.Oct.26_14_45_01.GMT.2005.egmond.c1.stack.ras
1130339701.Wed.Oct.26_15_15_01.GMT.2005.egmond.c1.stack.ras
1130341501.Wed.Oct.26_15_45_01.GMT.2005.egmond.c1.stack.ras
1130393701.Thu.Oct.27_06_15_01.GMT.2005.egmond.c1.stack.ras
1130395501.Thu.Oct.27_06_45_01.GMT.2005.egmond.c1.stack.ras
1130397301.Thu.Oct.27_07_15_01.GMT.2005.egmond.c1.stack.ras
1130399101.Thu.Oct.27_07_45_01.GMT.2005.egmond.c1.stack.ras
1130400901.Thu.Oct.27_08_15_01.GMT.2005.egmond.c1.stack.ras
1130402701.Thu.Oct.27_08_45_01.GMT.2005.egmond.c1.stack.ras
1130404501.Thu.Oct.27_09_15_01.GMT.2005.egmond.c1.stack.ras
1130406302.Thu.Oct.27_09_45_02.GMT.2005.egmond.c1.stack.ras
1130408101.Thu.Oct.27_10_15_01.GMT.2005.egmond.c1.stack.ras
1130409901.Thu.Oct.27_10_45_01.GMT.2005.egmond.c1.stack.ras
1130411702.Thu.Oct.27_11_15_02.GMT.2005.egmond.c1.stack.ras
1130413502.Thu.Oct.27_11_45_02.GMT.2005.egmond.c1.stack.ras
1130415301.Thu.Oct.27_12_15_01.GMT.2005.egmond.c1.stack.ras
1130417101.Thu.Oct.27_12_45_01.GMT.2005.egmond.c1.stack.ras
1130418901.Thu.Oct.27_13_15_01.GMT.2005.egmond.c1.stack.ras
1130420701.Thu.Oct.27_13_45_01.GMT.2005.egmond.c1.stack.ras
1130422501.Thu.Oct.27_14_15_01.GMT.2005.egmond.c1.stack.ras
1130424301.Thu.Oct.27_14_45_01.GMT.2005.egmond.c1.stack.ras
1130426102.Thu.Oct.27_15_15_02.GMT.2005.egmond.c1.stack.ras
1130427901.Thu.Oct.27_15_45_01.GMT.2005.egmond.c1.stack.ras

C Wave spectra

C.1 Frequency spectra

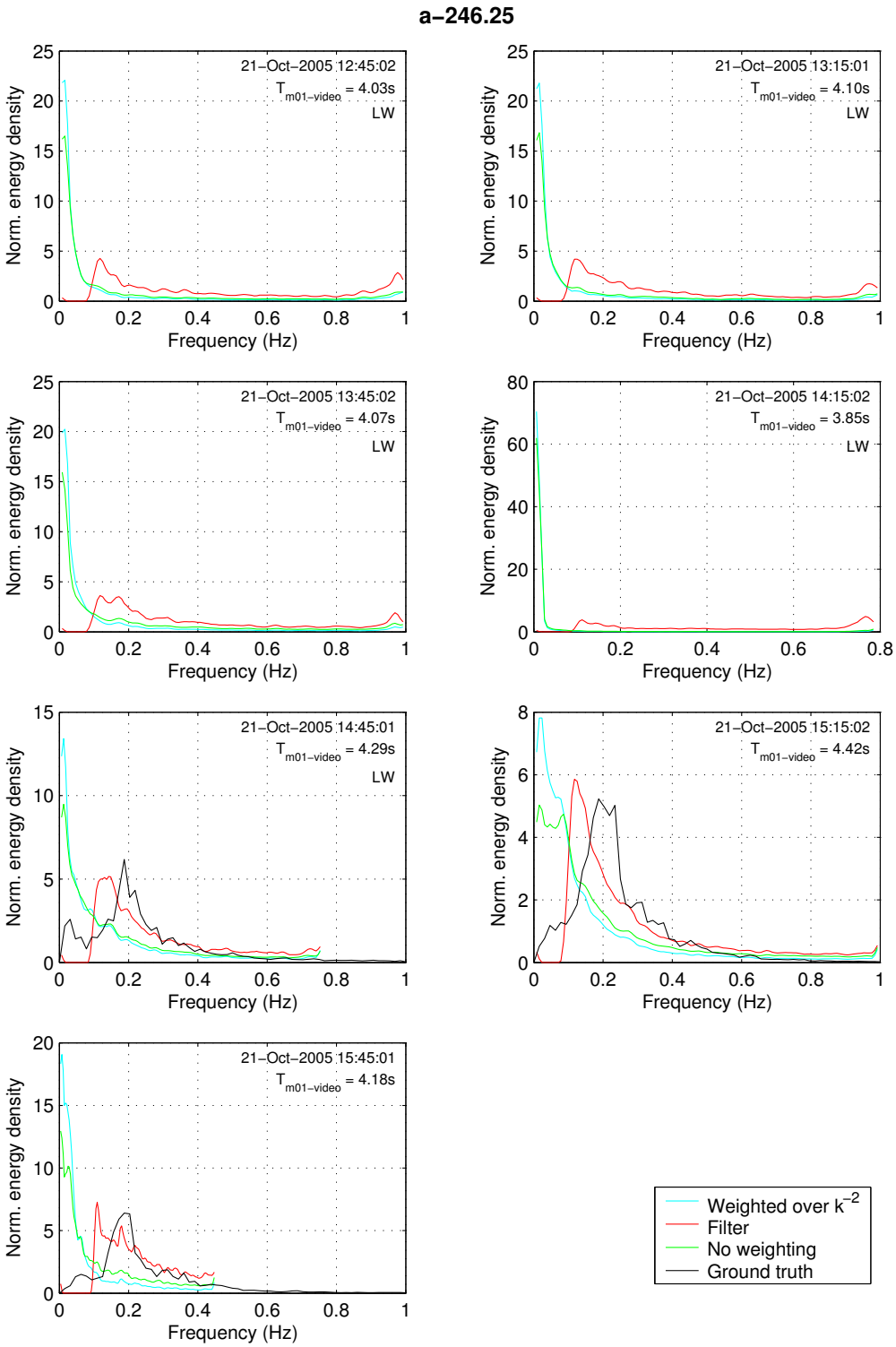

a–246.25

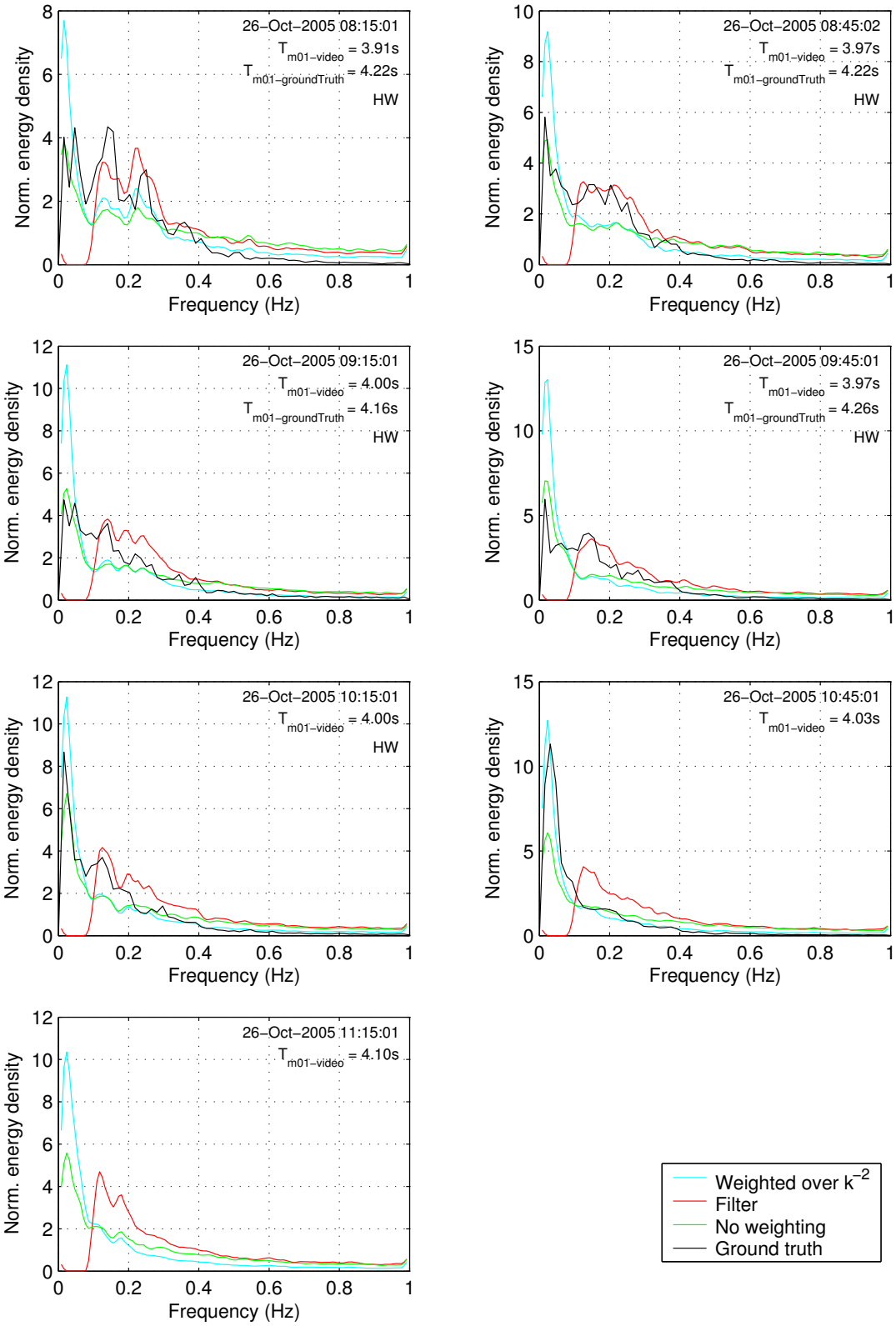
26–Oct–2005 08:15:01
$T_{m01-video}$ = 3.91s
$T_{m01-groundTruth}$ = 4.22s
HW
26–Oct–2005 08:45:02
$T_{m01-video}$ = 3.97s
$T_{m01-groundTruth}$ = 4.22s
HW
26–Oct–2005 09:15:01
$T_{m01-video}$ = 4.00s
$T_{m01-groundTruth}$ = 4.16s
HW
26–Oct–2005 09:45:01
$T_{m01-video}$ = 3.97s
$T_{m01-groundTruth}$ = 4.26s
HW
26–Oct–2005 10:15:01
$T_{m01-video}$ = 4.00s
HW
26–Oct–2005 10:45:01
$T_{m01-video}$ = 4.03s
26–Oct–2005 11:15:01
$T_{m01-video}$ = 4.10s
Norm. energy density
Frequency (Hz)
Weighted over k^{-2}
Filter
No weighting
Ground truth

a–246.25

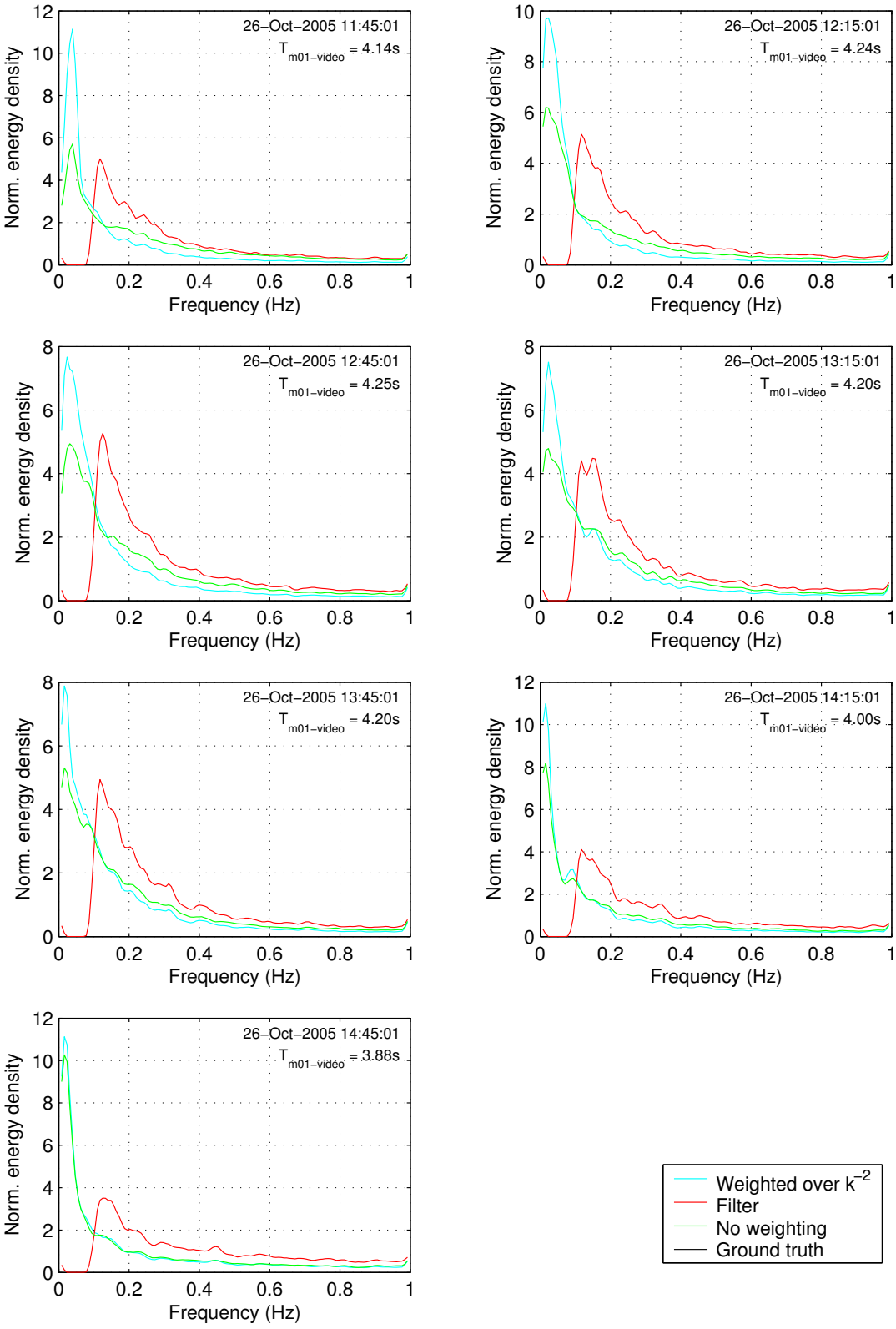
26–Oct–2005 11:45:01
$T_{m01-video}$ = 4.14s
26–Oct–2005 12:15:01
$T_{m01-video}$ = 4.24s
26–Oct–2005 12:45:01
$T_{m01-video}$ = 4.25s
26–Oct–2005 13:15:01
$T_{m01-video}$ = 4.20s
26–Oct–2005 13:45:01
$T_{m01-video}$ = 4.20s
26–Oct–2005 14:15:01
$T_{m01-video}$ = 4.00s
26–Oct–2005 14:45:01
$T_{m01-video}$ = 3.88s
Norm. energy density
Frequency (Hz)
Weighted over k^{-2}
Filter
No weighting
Ground truth

a–246.25

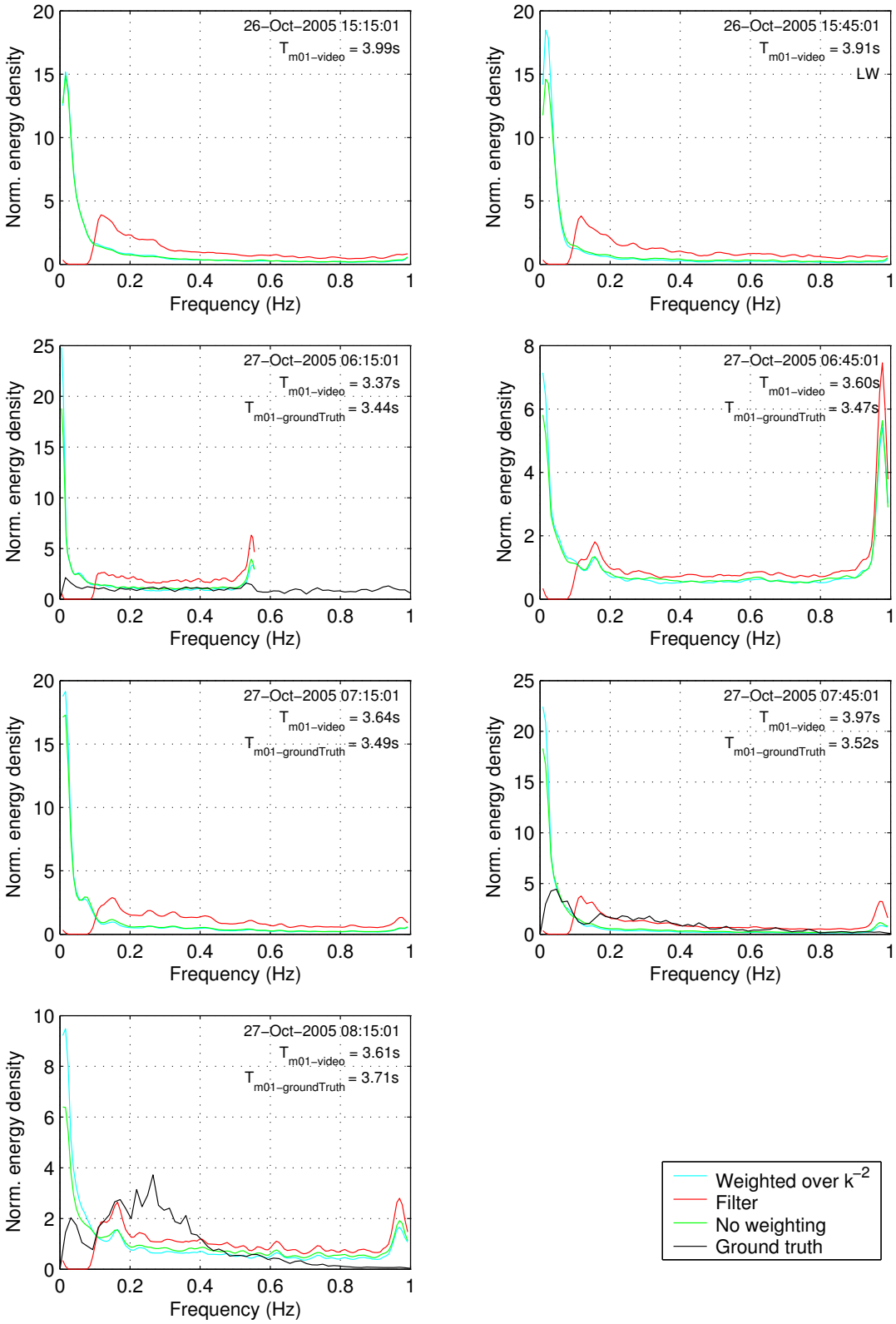
26–Oct–2005 15:15:01
T m01–video = 3.99s
26–Oct–2005 15:45:01
T m01–video = 3.91s
LW
27–Oct–2005 06:15:01
T m01–video = 3.37s
T m01–groundTruth = 3.44s
27–Oct–2005 06:45:01
T m01–video = 3.60s
T m01–groundTruth = 3.47s
27–Oct–2005 07:15:01
T m01–video = 3.64s
T m01–groundTruth = 3.49s
27–Oct–2005 07:45:01
T m01–video = 3.97s
T m01–groundTruth = 3.52s
27–Oct–2005 08:15:01
T m01–video = 3.61s
T m01–groundTruth = 3.71s
Norm. energy density
Frequency (Hz)
Weighted over k−2
Filter
No weighting
Ground truth

a–246.25

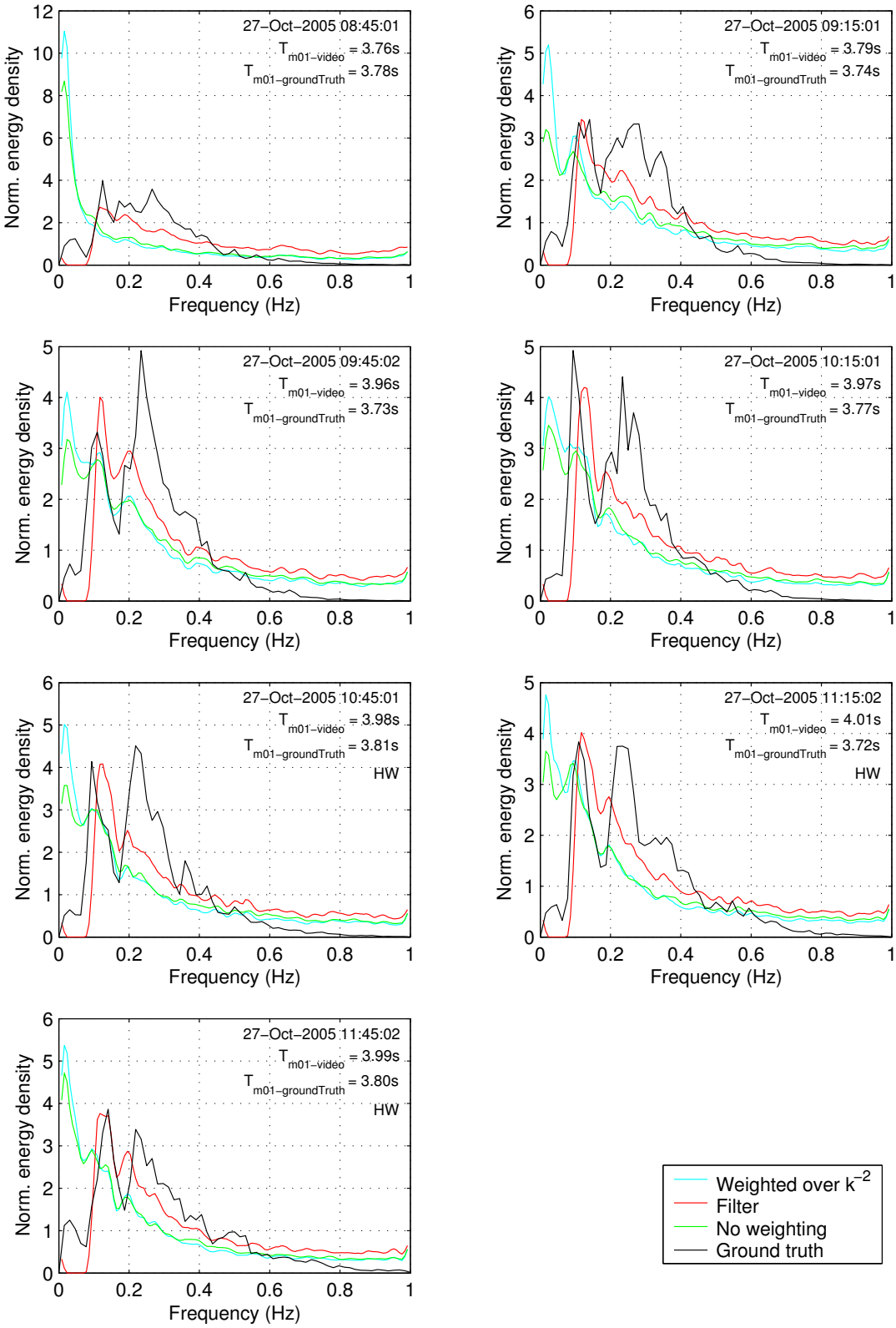
27–Oct–2005 08:45:01
$T_{m01-video}$ = 3.76s
$T_{m01-groundTruth}$ = 3.78s
27–Oct–2005 09:15:01
$T_{m01-video}$ = 3.79s
$T_{m01-groundTruth}$ = 3.74s
27–Oct–2005 09:45:02
$T_{m01-video}$ = 3.96s
$T_{m01-groundTruth}$ = 3.73s
27–Oct–2005 10:15:01
$T_{m01-video}$ = 3.97s
$T_{m01-groundTruth}$ = 3.77s
27–Oct–2005 10:45:01
$T_{m01-video}$ = 3.98s
$T_{m01-groundTruth}$ = 3.81s
HW
27–Oct–2005 11:15:02
$T_{m01-video}$ = 4.01s
$T_{m01-groundTruth}$ = 3.72s
HW
27–Oct–2005 11:45:02
$T_{m01-video}$ = 3.99s
$T_{m01-groundTruth}$ = 3.80s
HW
Norm. energy density
Frequency (Hz)
Weighted over k^{-2}
Filter
No weighting
Ground truth

a–246.25

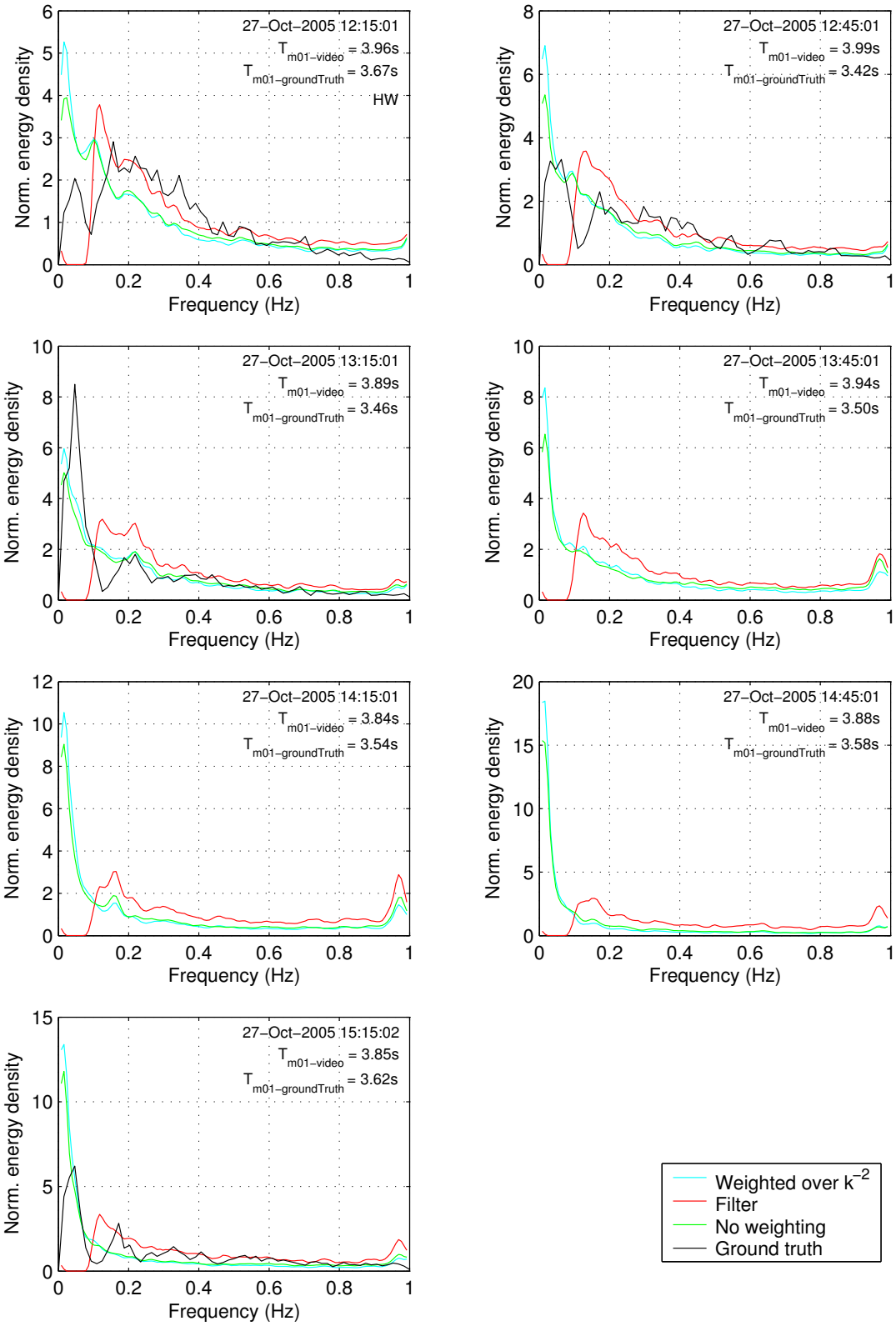
27–Oct–2005 12:15:01
T m01–video = 3.96s
T m01–groundTruth = 3.67s
HW
27–Oct–2005 12:45:01
T m01–video = 3.99s
T m01–groundTruth = 3.42s
27–Oct–2005 13:15:01
T m01–video = 3.89s
T m01–groundTruth = 3.46s
27–Oct–2005 13:45:01
T m01–video = 3.94s
T m01–groundTruth = 3.50s
27–Oct–2005 14:15:01
T m01–video = 3.84s
T m01–groundTruth = 3.54s
27–Oct–2005 14:45:01
T m01–video = 3.88s
T m01–groundTruth = 3.58s
27–Oct–2005 15:15:02
T m01–video = 3.85s
T m01–groundTruth = 3.62s
Norm. energy density
Frequency (Hz)
Weighted over k−2
Filter
No weighting
Ground truth

a–246.25

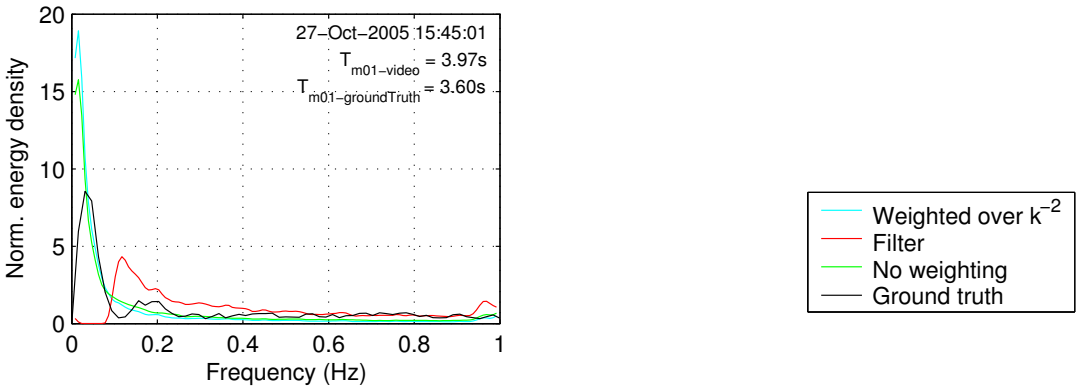
27–Oct–2005 15:45:01
$T_{m01-video}$ = 3.97s
$T_{m01-groundTruth}$ = 3.60s
Norm. energy density
Frequency (Hz)
0
5
10
15
20
0
0.2
0.4
0.6
0.8
1
Weighted over k^{-2}
Filter
No weighting
Ground truth

a–246.31

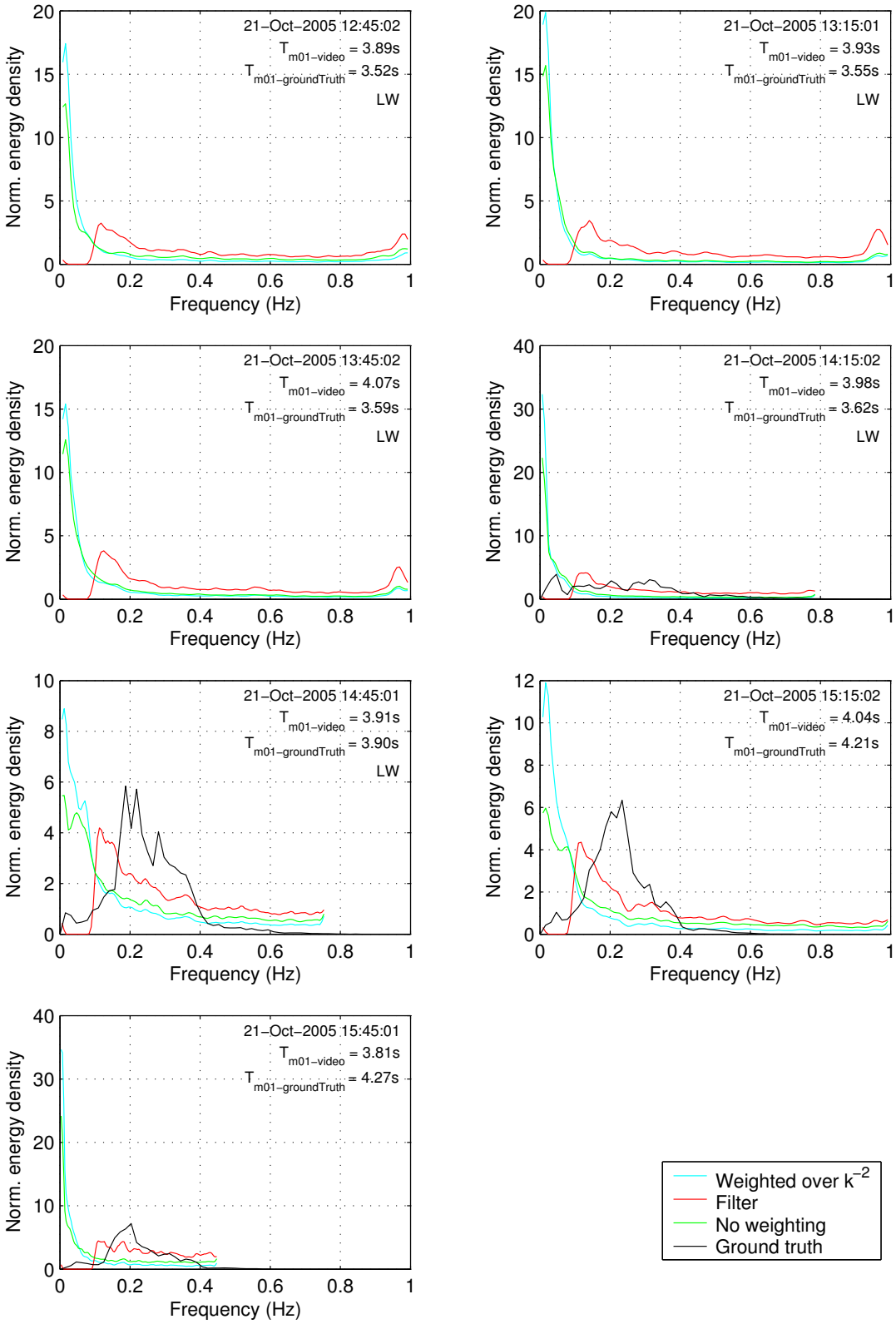
21–Oct–2005 12:45:02
T m01–video = 3.89s
T m01–groundTruth = 3.52s
LW
21–Oct–2005 13:15:01
T m01–video = 3.93s
T m01–groundTruth = 3.55s
LW
21–Oct–2005 13:45:02
T m01–video = 4.07s
T m01–groundTruth = 3.59s
LW
21–Oct–2005 14:15:02
T m01–video = 3.98s
T m01–groundTruth = 3.62s
LW
21–Oct–2005 14:45:01
T m01–video = 3.91s
T m01–groundTruth = 3.90s
LW
21–Oct–2005 15:15:02
T m01–video = 4.04s
T m01–groundTruth = 4.21s
21–Oct–2005 15:45:01
T m01–video = 3.81s
T m01–groundTruth = 4.27s
Norm. energy density
Frequency (Hz)
Weighted over k−2
Filter
No weighting
Ground truth

a–246.31

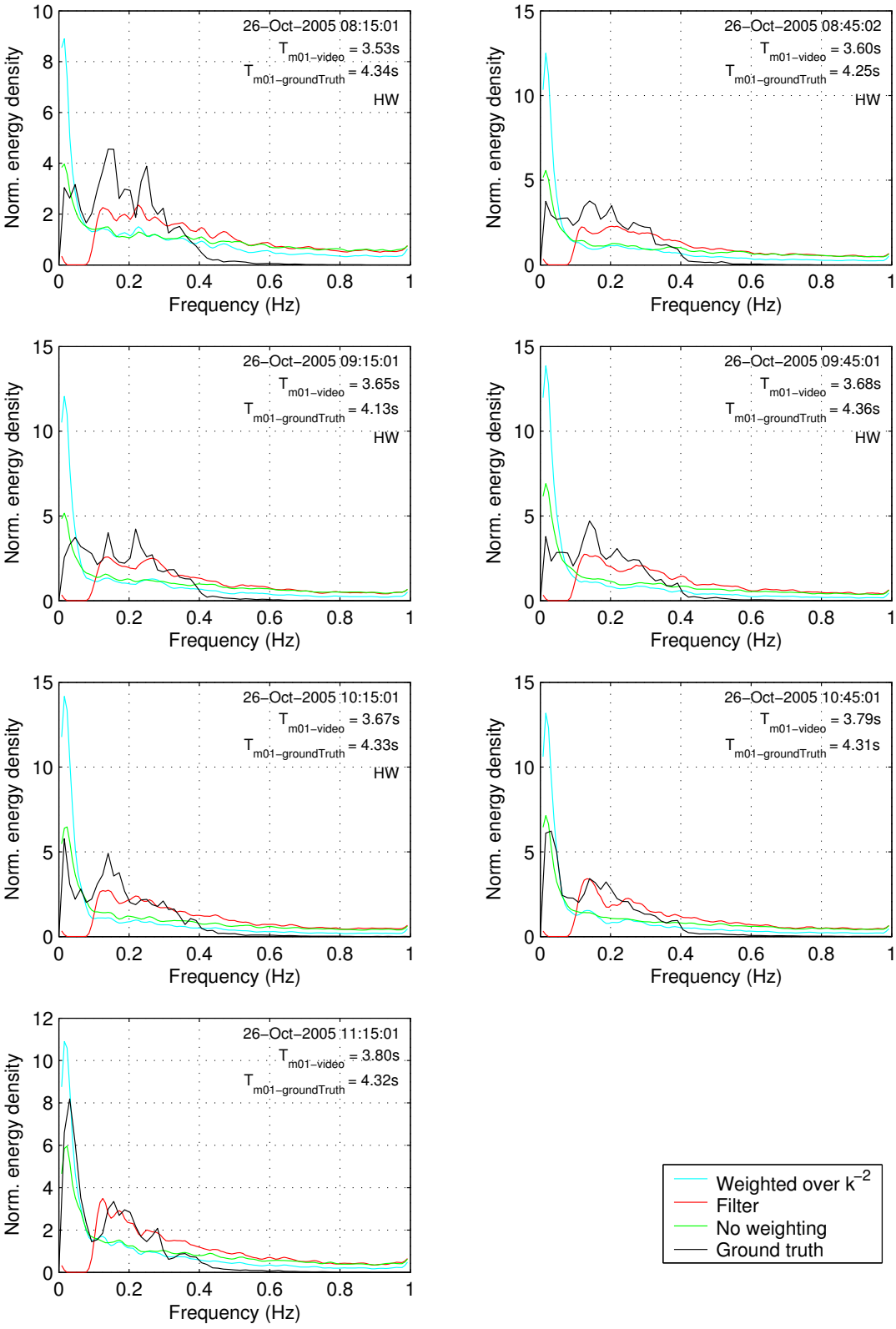
26–Oct–2005 08:15:01
$T_{m01-video}$ = 3.53s
$T_{m01-groundTruth}$ = 4.34s
HW
26–Oct–2005 08:45:02
$T_{m01-video}$ = 3.60s
$T_{m01-groundTruth}$ = 4.25s
HW
26–Oct–2005 09:15:01
$T_{m01-video}$ = 3.65s
$T_{m01-groundTruth}$ = 4.13s
HW
26–Oct–2005 09:45:01
$T_{m01-video}$ = 3.68s
$T_{m01-groundTruth}$ = 4.36s
HW
26–Oct–2005 10:15:01
$T_{m01-video}$ = 3.67s
$T_{m01-groundTruth}$ = 4.33s
HW
26–Oct–2005 10:45:01
$T_{m01-video}$ = 3.79s
$T_{m01-groundTruth}$ = 4.31s
26–Oct–2005 11:15:01
$T_{m01-video}$ = 3.80s
$T_{m01-groundTruth}$ = 4.32s
Norm. energy density
Frequency (Hz)
Weighted over k^{-2}
Filter
No weighting
Ground truth

a–246.31

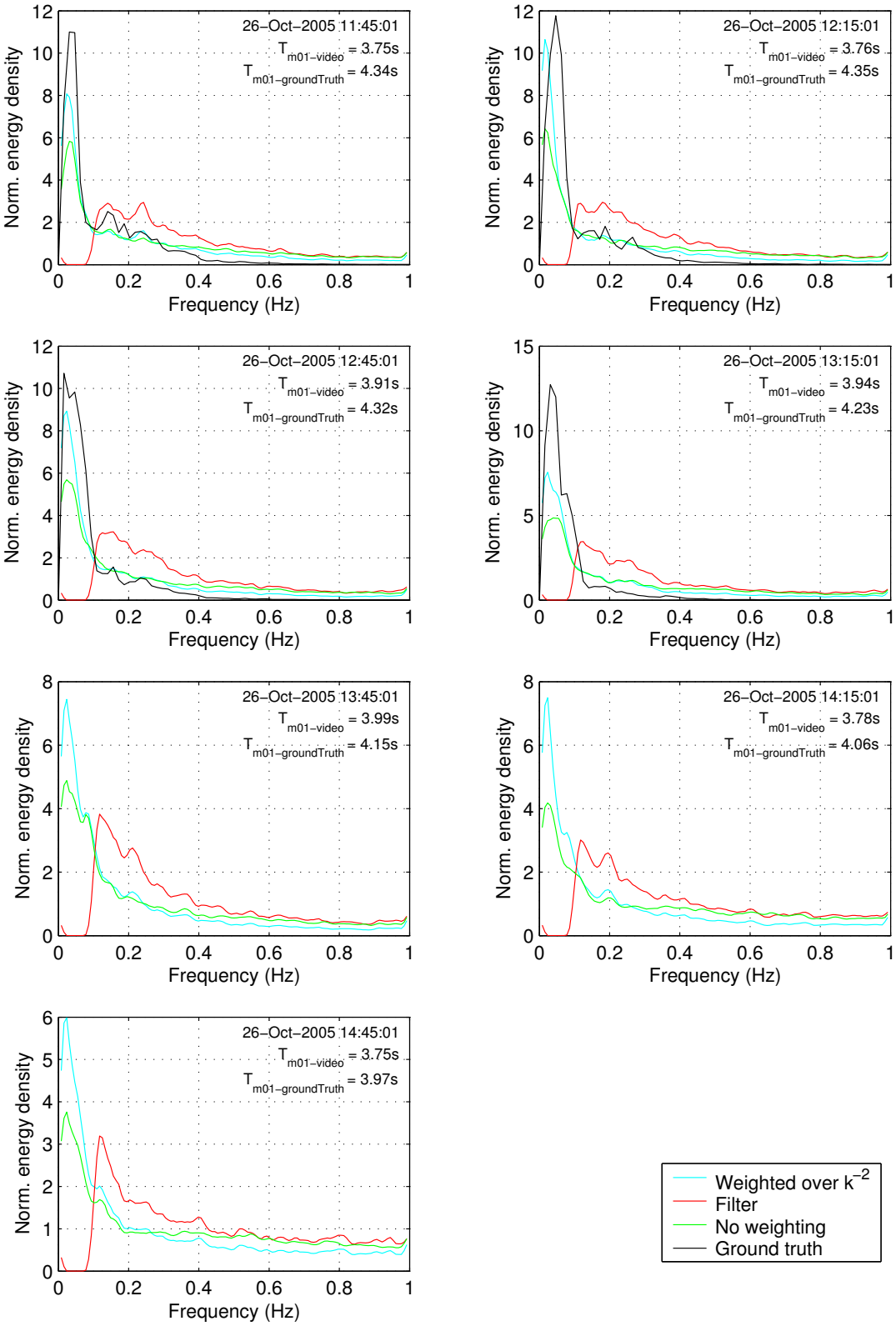
26–Oct–2005 11:45:01
T m01–video = 3.75s
T m01–groundTruth = 4.34s
26–Oct–2005 12:15:01
T m01–video = 3.76s
T m01–groundTruth = 4.35s
26–Oct–2005 12:45:01
T m01–video = 3.91s
T m01–groundTruth = 4.32s
26–Oct–2005 13:15:01
T m01–video = 3.94s
T m01–groundTruth = 4.23s
26–Oct–2005 13:45:01
T m01–video = 3.99s
T m01–groundTruth = 4.15s
26–Oct–2005 14:15:01
T m01–video = 3.78s
T m01–groundTruth = 4.06s
26–Oct–2005 14:45:01
T m01–video = 3.75s
T m01–groundTruth = 3.97s
Norm. energy density
Frequency (Hz)
Weighted over k−2
Filter
No weighting
Ground truth

a–246.31

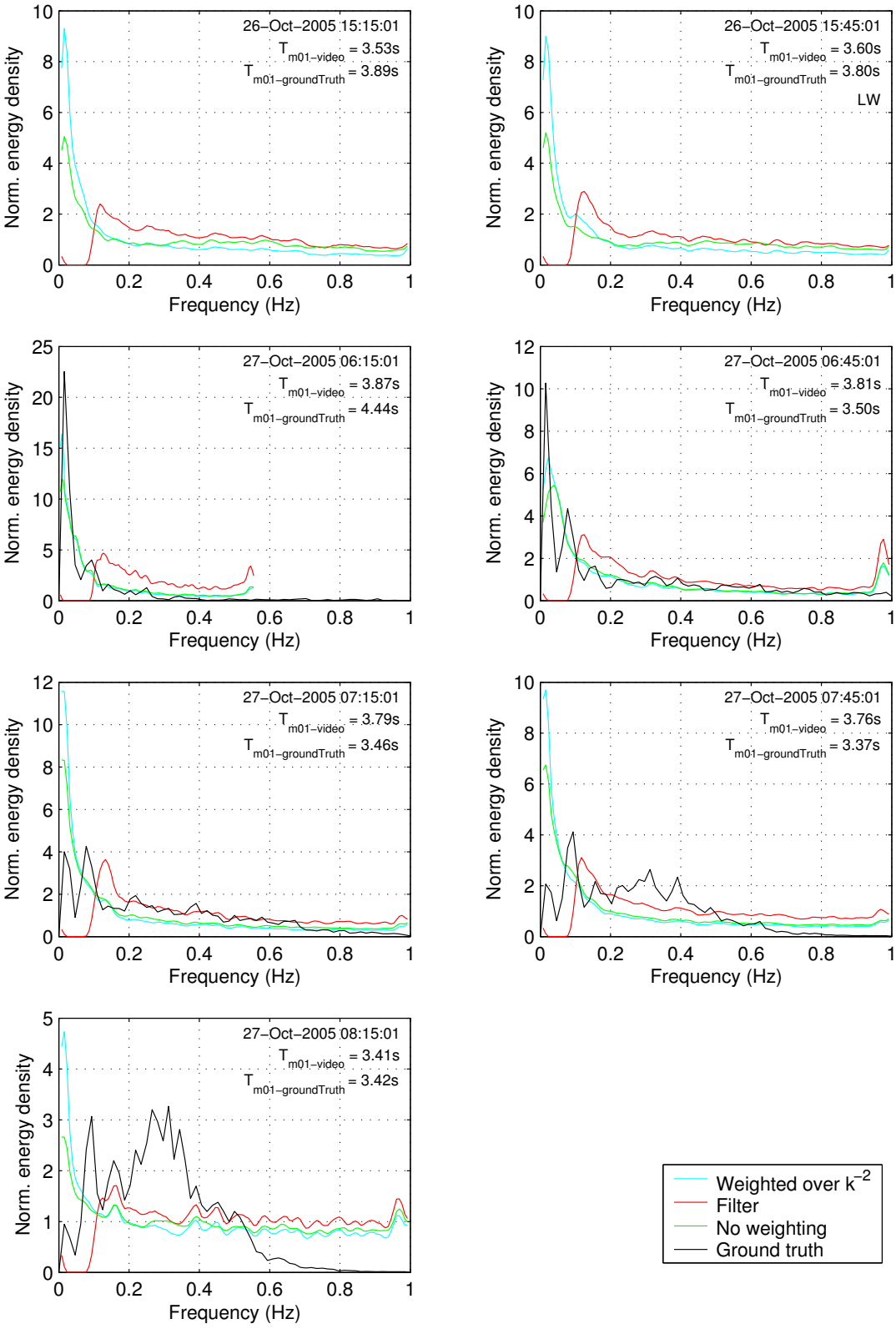
26–Oct–2005 15:15:01
T m01–video = 3.53s
T m01–groundTruth = 3.89s
26–Oct–2005 15:45:01
T m01–video = 3.60s
T m01–groundTruth = 3.80s
LW
27–Oct–2005 06:15:01
T m01–video = 3.87s
T m01–groundTruth = 4.44s
27–Oct–2005 06:45:01
T m01–video = 3.81s
T m01–groundTruth = 3.50s
27–Oct–2005 07:15:01
T m01–video = 3.79s
T m01–groundTruth = 3.46s
27–Oct–2005 07:45:01
T m01–video = 3.76s
T m01–groundTruth = 3.37s
27–Oct–2005 08:15:01
T m01–video = 3.41s
T m01–groundTruth = 3.42s
Norm. energy density
Frequency (Hz)
Weighted over k−2
Filter
No weighting
Ground truth

a–246.31

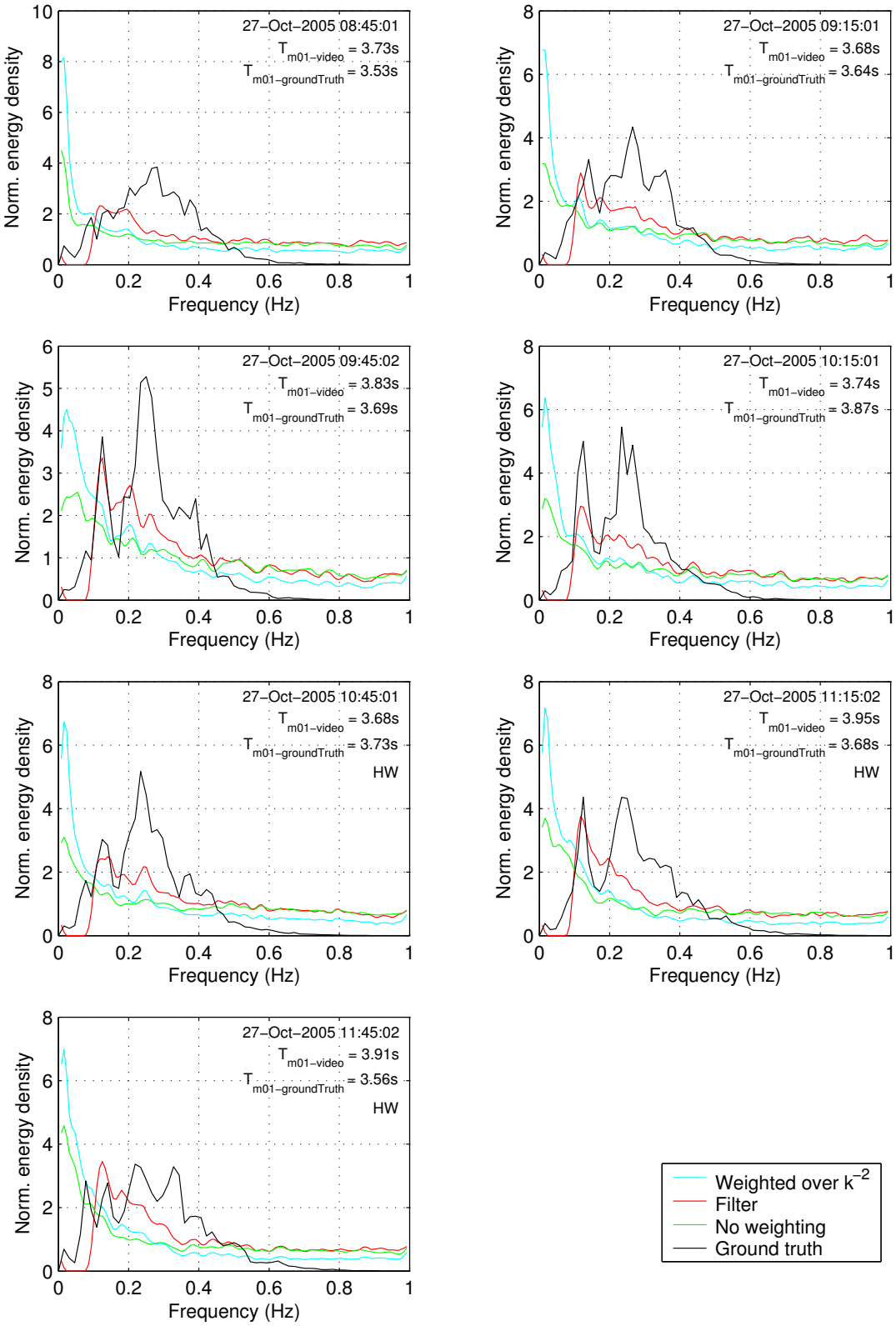
27–Oct–2005 08:45:01
T m01–video = 3.73s
T m01–groundTruth = 3.53s
27–Oct–2005 09:15:01
T m01–video = 3.68s
T m01–groundTruth = 3.64s
27–Oct–2005 09:45:02
T m01–video = 3.83s
T m01–groundTruth = 3.69s
27–Oct–2005 10:15:01
T m01–video = 3.74s
T m01–groundTruth = 3.87s
27–Oct–2005 10:45:01
T m01–video = 3.68s
T m01–groundTruth = 3.73s
HW
27–Oct–2005 11:15:02
T m01–video = 3.95s
T m01–groundTruth = 3.68s
HW
27–Oct–2005 11:45:02
T m01–video = 3.91s
T m01–groundTruth = 3.56s
HW
Norm. energy density
Frequency (Hz)
Weighted over k−2
Filter
No weighting
Ground truth

a–246.31

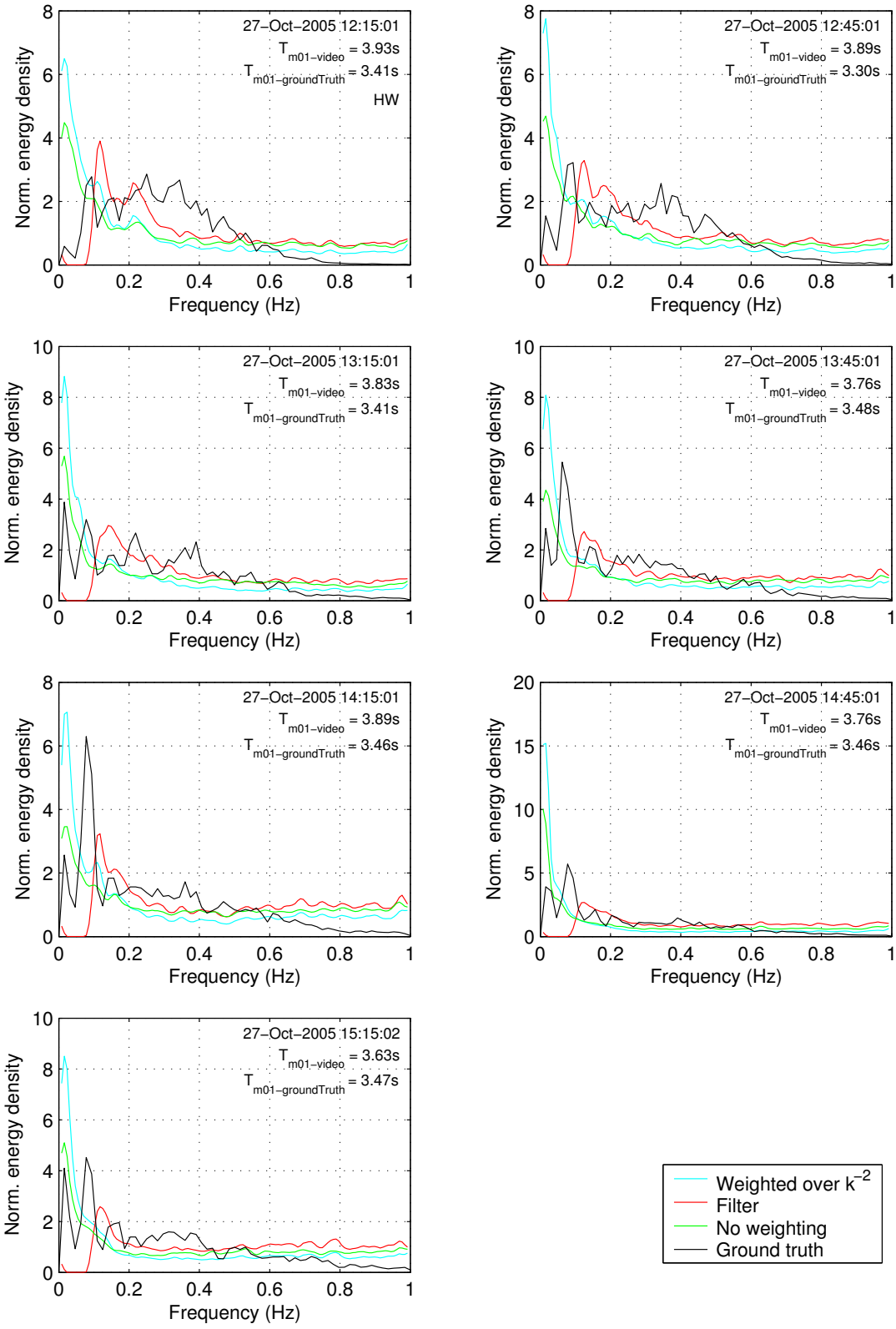
27–Oct–2005 12:15:01
T m01–video = 3.93s
T m01–groundTruth = 3.41s
HW
27–Oct–2005 12:45:01
T m01–video = 3.89s
T m01–groundTruth = 3.30s
27–Oct–2005 13:15:01
T m01–video = 3.83s
T m01–groundTruth = 3.41s
27–Oct–2005 13:45:01
T m01–video = 3.76s
T m01–groundTruth = 3.48s
27–Oct–2005 14:15:01
T m01–video = 3.89s
T m01–groundTruth = 3.46s
27–Oct–2005 14:45:01
T m01–video = 3.76s
T m01–groundTruth = 3.46s
27–Oct–2005 15:15:02
T m01–video = 3.63s
T m01–groundTruth = 3.47s
Norm. energy density
Frequency (Hz)
Weighted over k−2
Filter
No weighting
Ground truth

a–246.31

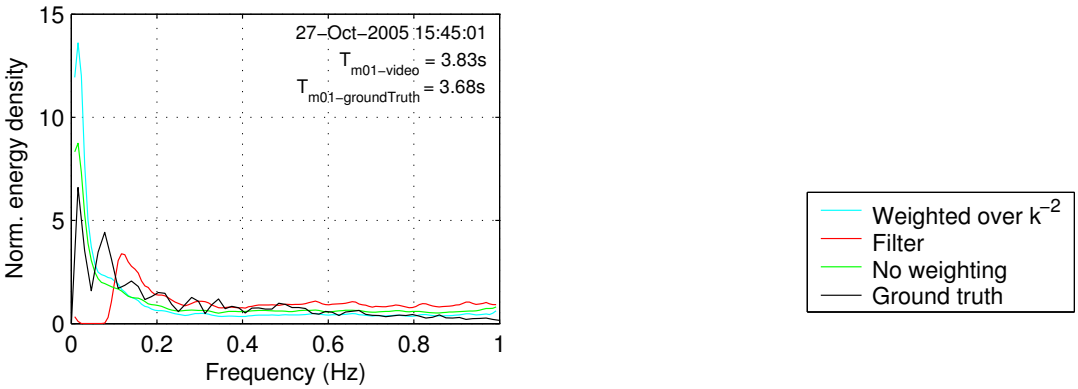
27–Oct–2005 15:45:01
$T_{m01-video}$ = 3.83s
$T_{m01-groundTruth}$ = 3.68s
Norm. energy density
Frequency (Hz)
0
5
10
15
0.2
0.4
0.6
0.8
1
Weighted over k^{-2}
Filter
No weighting
Ground truth

a–246.37

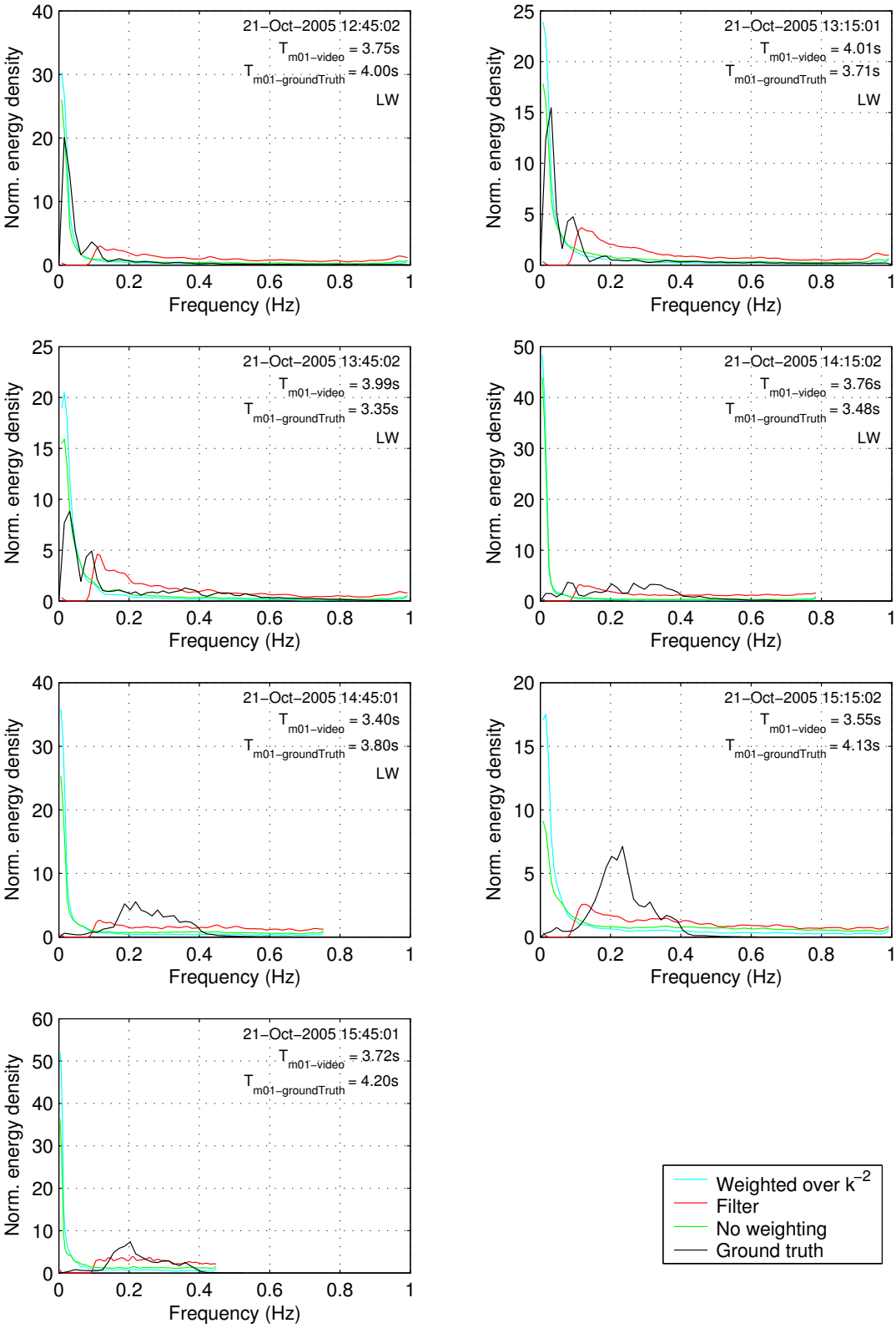
21–Oct–2005 12:45:02
$T_{m01-video}$ = 3.75s
$T_{m01-groundTruth}$ = 4.00s
LW
21–Oct–2005 13:15:01
$T_{m01-video}$ = 4.01s
$T_{m01-groundTruth}$ = 3.71s
LW
21–Oct–2005 13:45:02
$T_{m01-video}$ = 3.99s
$T_{m01-groundTruth}$ = 3.35s
LW
21–Oct–2005 14:15:02
$T_{m01-video}$ = 3.76s
$T_{m01-groundTruth}$ = 3.48s
LW
21–Oct–2005 14:45:01
$T_{m01-video}$ = 3.40s
$T_{m01-groundTruth}$ = 3.80s
LW
21–Oct–2005 15:15:02
$T_{m01-video}$ = 3.55s
$T_{m01-groundTruth}$ = 4.13s
21–Oct–2005 15:45:01
$T_{m01-video}$ = 3.72s
$T_{m01-groundTruth}$ = 4.20s
Norm. energy density
Frequency (Hz)
Weighted over k^{-2}
Filter
No weighting
Ground truth

a–246.37

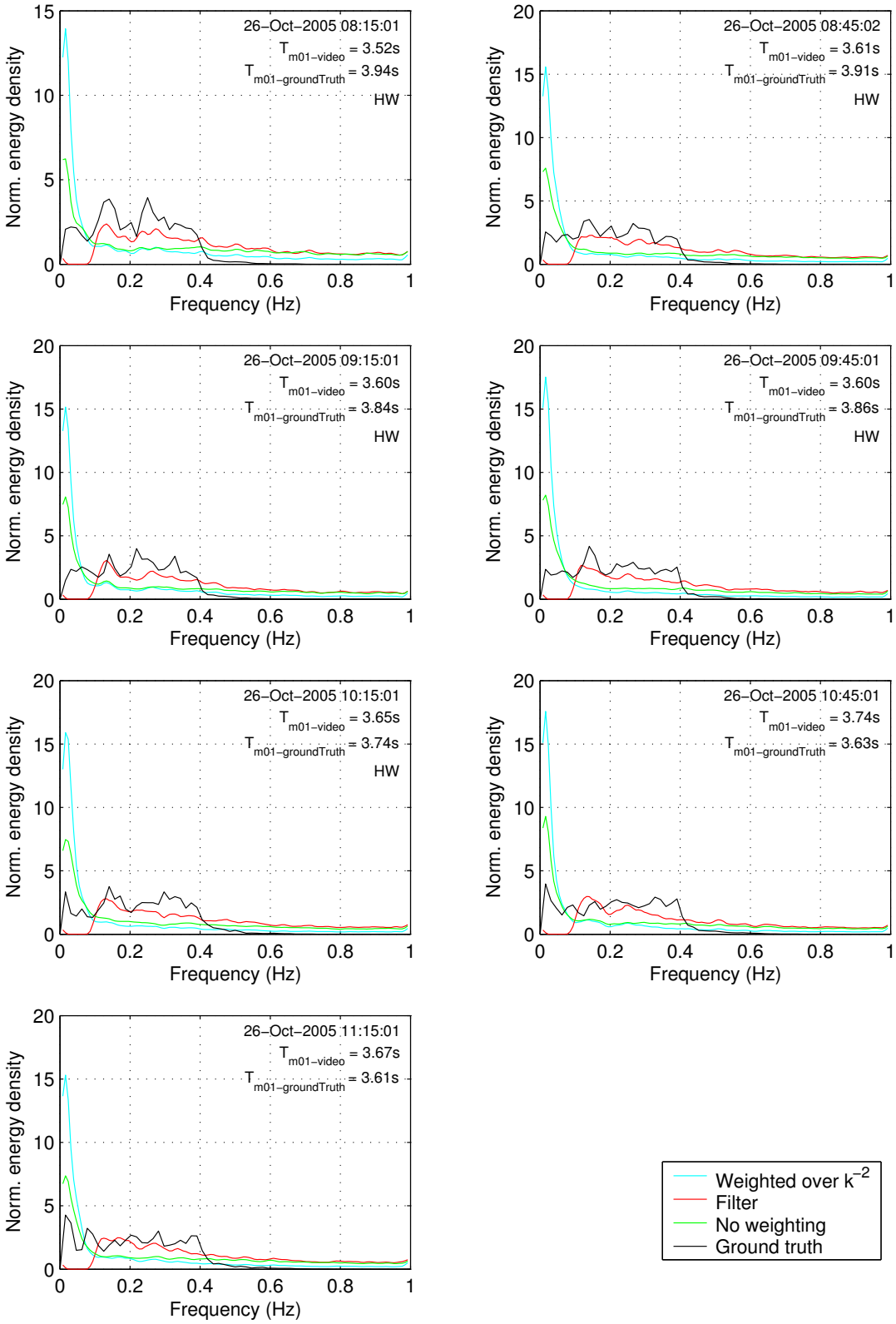
26–Oct–2005 08:15:01
T m01–video = 3.52s
T m01–groundTruth = 3.94s
HW
26–Oct–2005 08:45:02
T m01–video = 3.61s
T m01–groundTruth = 3.91s
HW
26–Oct–2005 09:15:01
T m01–video = 3.60s
T m01–groundTruth = 3.84s
HW
26–Oct–2005 09:45:01
T m01–video = 3.60s
T m01–groundTruth = 3.86s
HW
26–Oct–2005 10:15:01
T m01–video = 3.65s
T m01–groundTruth = 3.74s
HW
26–Oct–2005 10:45:01
T m01–video = 3.74s
T m01–groundTruth = 3.63s
26–Oct–2005 11:15:01
T m01–video = 3.67s
T m01–groundTruth = 3.61s
Norm. energy density
Frequency (Hz)
Weighted over k−2
Filter
No weighting
Ground truth

a–246.37

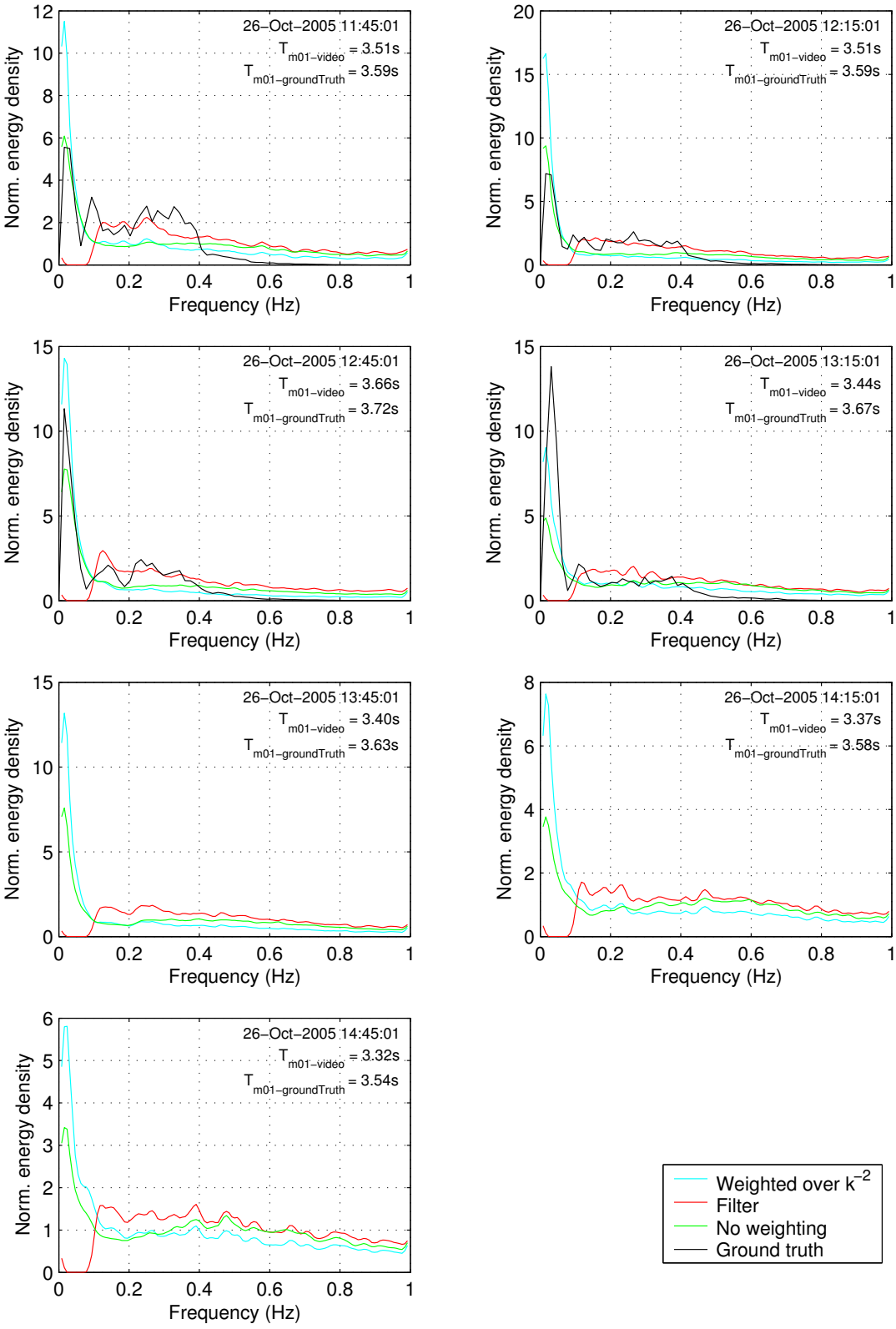
26–Oct–2005 11:45:01
$T_{m01-video}$ = 3.51s
$T_{m01-groundTruth}$ = 3.59s
26–Oct–2005 12:15:01
$T_{m01-video}$ = 3.51s
$T_{m01-groundTruth}$ = 3.59s
26–Oct–2005 12:45:01
$T_{m01-video}$ = 3.66s
$T_{m01-groundTruth}$ = 3.72s
26–Oct–2005 13:15:01
$T_{m01-video}$ = 3.44s
$T_{m01-groundTruth}$ = 3.67s
26–Oct–2005 13:45:01
$T_{m01-video}$ = 3.40s
$T_{m01-groundTruth}$ = 3.63s
26–Oct–2005 14:15:01
$T_{m01-video}$ = 3.37s
$T_{m01-groundTruth}$ = 3.58s
26–Oct–2005 14:45:01
$T_{m01-video}$ = 3.32s
$T_{m01-groundTruth}$ = 3.54s
Norm. energy density
Frequency (Hz)
Weighted over k^{-2}
Filter
No weighting
Ground truth

a–246.37

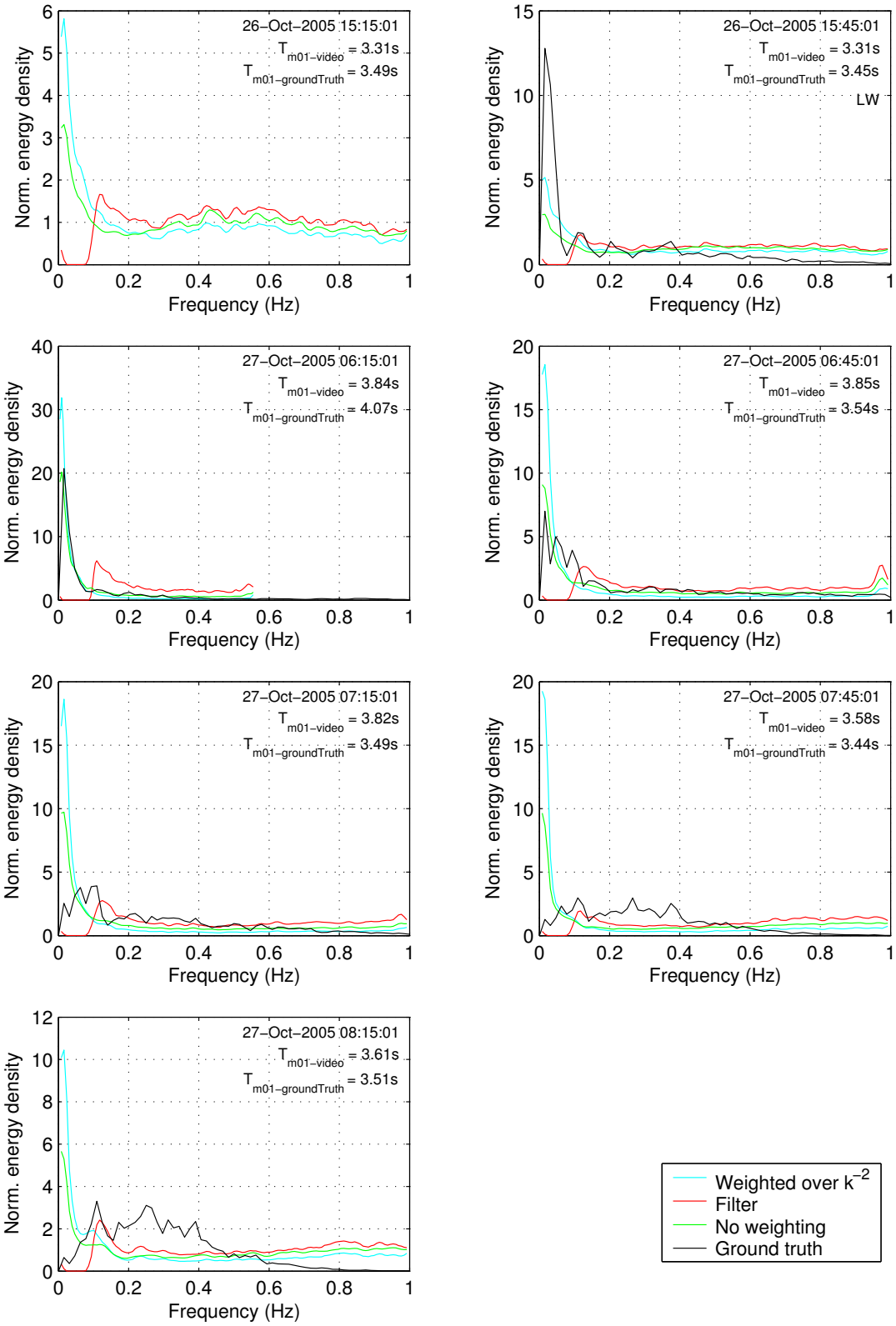
26–Oct–2005 15:15:01
T m01–video = 3.31s
T m01–groundTruth = 3.49s
26–Oct–2005 15:45:01
T m01–video = 3.31s
T m01–groundTruth = 3.45s
LW
27–Oct–2005 06:15:01
T m01–video = 3.84s
T m01–groundTruth = 4.07s
27–Oct–2005 06:45:01
T m01–video = 3.85s
T m01–groundTruth = 3.54s
27–Oct–2005 07:15:01
T m01–video = 3.82s
T m01–groundTruth = 3.49s
27–Oct–2005 07:45:01
T m01–video = 3.58s
T m01–groundTruth = 3.44s
27–Oct–2005 08:15:01
T m01–video = 3.61s
T m01–groundTruth = 3.51s
Norm. energy density
Frequency (Hz)
Weighted over k−2
Filter
No weighting
Ground truth

a–246.37

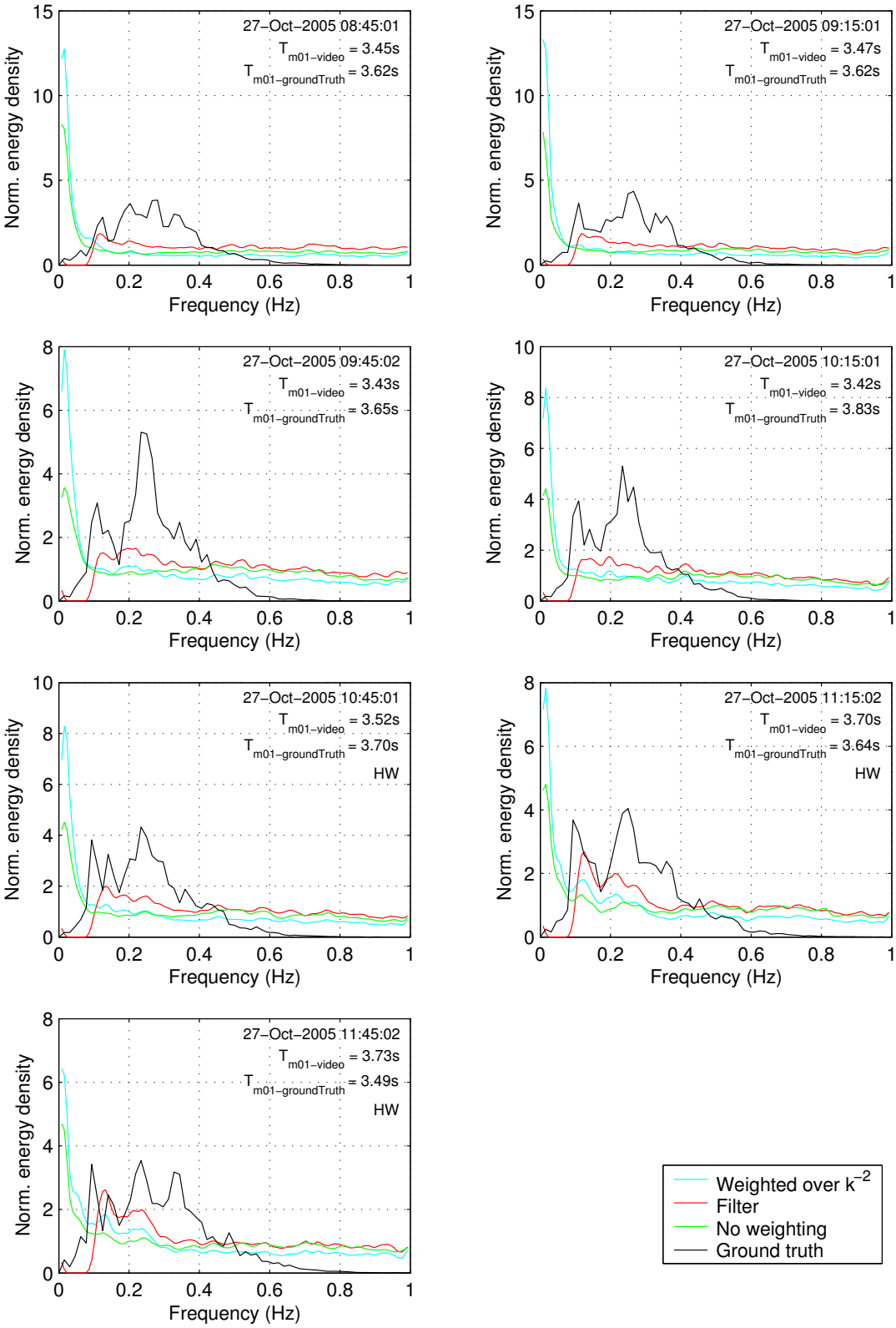
27–Oct–2005 08:45:01
T m01–video = 3.45s
T m01–groundTruth = 3.62s
27–Oct–2005 09:15:01
T m01–video = 3.47s
T m01–groundTruth = 3.62s
27–Oct–2005 09:45:02
T m01–video = 3.43s
T m01–groundTruth = 3.65s
27–Oct–2005 10:15:01
T m01–video = 3.42s
T m01–groundTruth = 3.83s
27–Oct–2005 10:45:01
T m01–video = 3.52s
T m01–groundTruth = 3.70s
HW
27–Oct–2005 11:15:02
T m01–video = 3.70s
T m01–groundTruth = 3.64s
HW
27–Oct–2005 11:45:02
T m01–video = 3.73s
T m01–groundTruth = 3.49s
HW
Norm. energy density
Frequency (Hz)
Weighted over k−2
Filter
No weighting
Ground truth

a–246.37

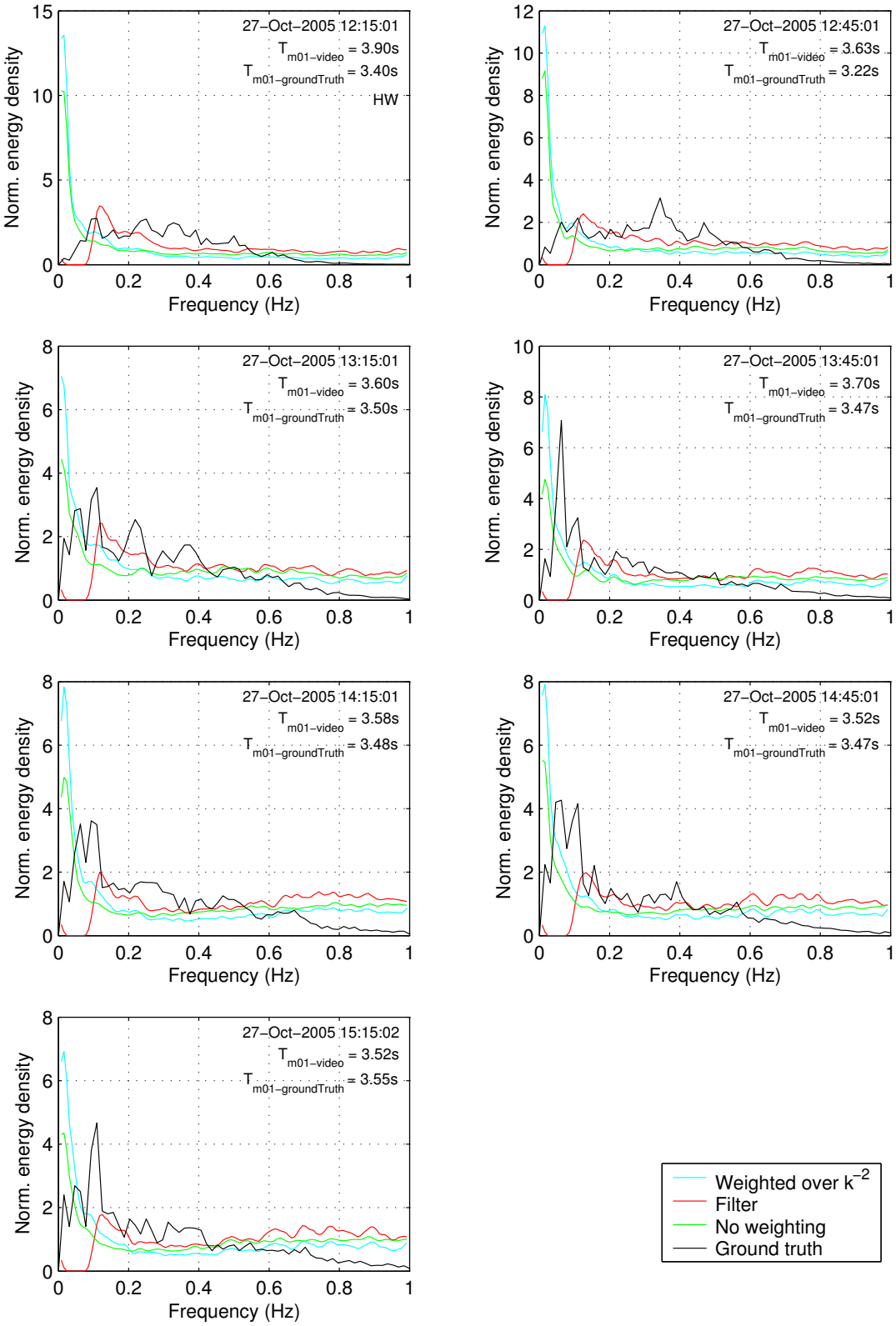
27–Oct–2005 12:15:01
T m01–video = 3.90s
T m01–groundTruth = 3.40s
HW
27–Oct–2005 12:45:01
T m01–video = 3.63s
T m01–groundTruth = 3.22s
27–Oct–2005 13:15:01
T m01–video = 3.60s
T m01–groundTruth = 3.50s
27–Oct–2005 13:45:01
T m01–video = 3.70s
T m01–groundTruth = 3.47s
27–Oct–2005 14:15:01
T m01–video = 3.58s
T m01–groundTruth = 3.48s
27–Oct–2005 14:45:01
T m01–video = 3.52s
T m01–groundTruth = 3.47s
27–Oct–2005 15:15:02
T m01–video = 3.52s
T m01–groundTruth = 3.55s
Norm. energy density
Frequency (Hz)
Weighted over k−2
Filter
No weighting
Ground truth

a–246.37

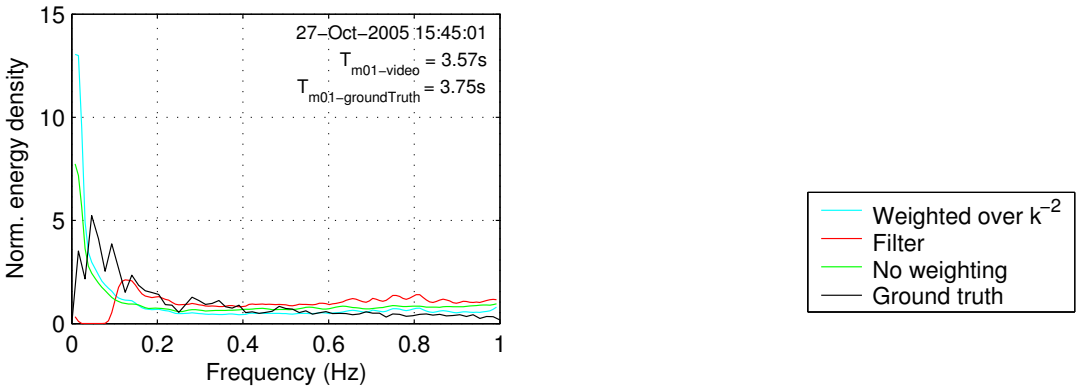
27–Oct–2005 15:45:01
$T_{m01-video}$ = 3.57s
$T_{m01-groundTruth}$ = 3.75s
Norm. energy density
Frequency (Hz)
0
5
10
15
0.2
0.4
0.6
0.8
1
Weighted over k^{-2}
Filter
No weighting
Ground truth

C.2 Directional spectra

a–246.25

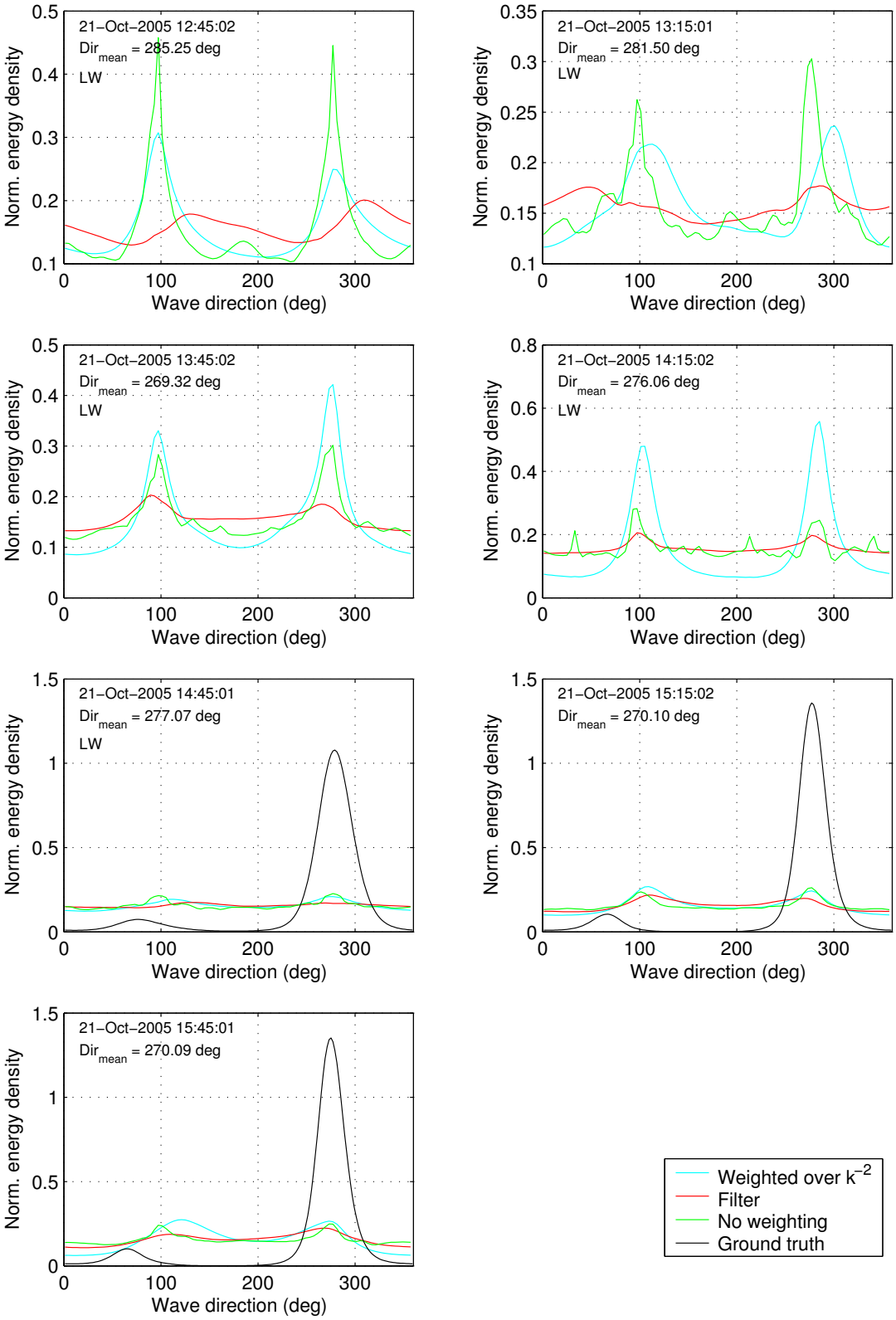

a–246.25

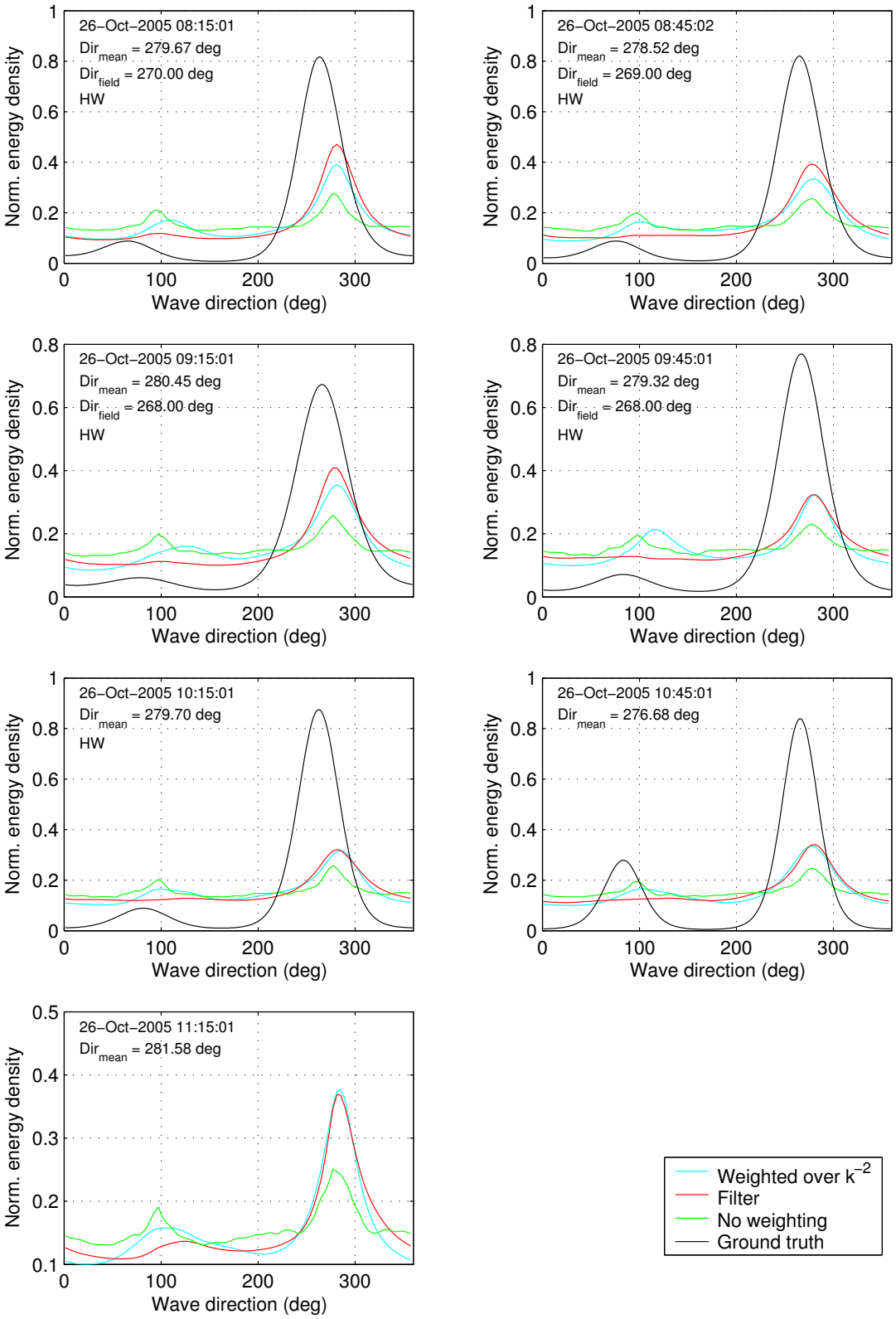
26–Oct–2005 08:15:01
Dir mean = 279.67 deg
Dir field = 270.00 deg
HW
26–Oct–2005 08:45:02
Dir mean = 278.52 deg
Dir field = 269.00 deg
HW
26–Oct–2005 09:15:01
Dir mean = 280.45 deg
Dir field = 268.00 deg
HW
26–Oct–2005 09:45:01
Dir mean = 279.32 deg
Dir field = 268.00 deg
HW
26–Oct–2005 10:15:01
Dir mean = 279.70 deg
HW
26–Oct–2005 10:45:01
Dir mean = 276.68 deg
26–Oct–2005 11:15:01
Dir mean = 281.58 deg
Norm. energy density
Wave direction (deg)
Weighted over k−2
Filter
No weighting
Ground truth

a–246.25

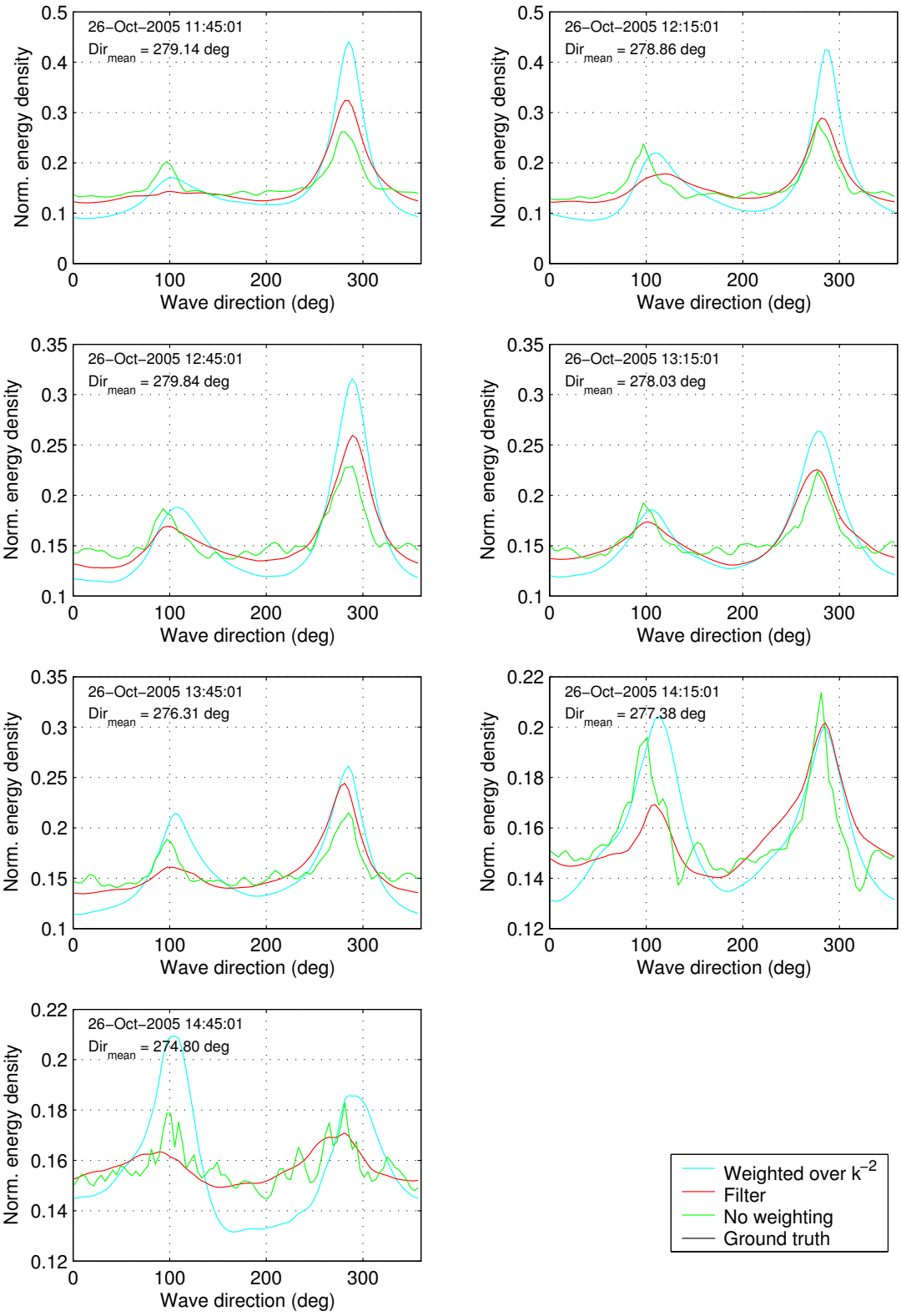
26–Oct–2005 11:45:01
Dir mean = 279.14 deg
26–Oct–2005 12:15:01
Dir mean = 278.86 deg
26–Oct–2005 12:45:01
Dir mean = 279.84 deg
26–Oct–2005 13:15:01
Dir mean = 278.03 deg
26–Oct–2005 13:45:01
Dir mean = 276.31 deg
26–Oct–2005 14:15:01
Dir mean = 277.38 deg
26–Oct–2005 14:45:01
Dir mean = 274.80 deg
Norm. energy density
Wave direction (deg)
Weighted over k−2
Filter
No weighting
Ground truth

a–246.25

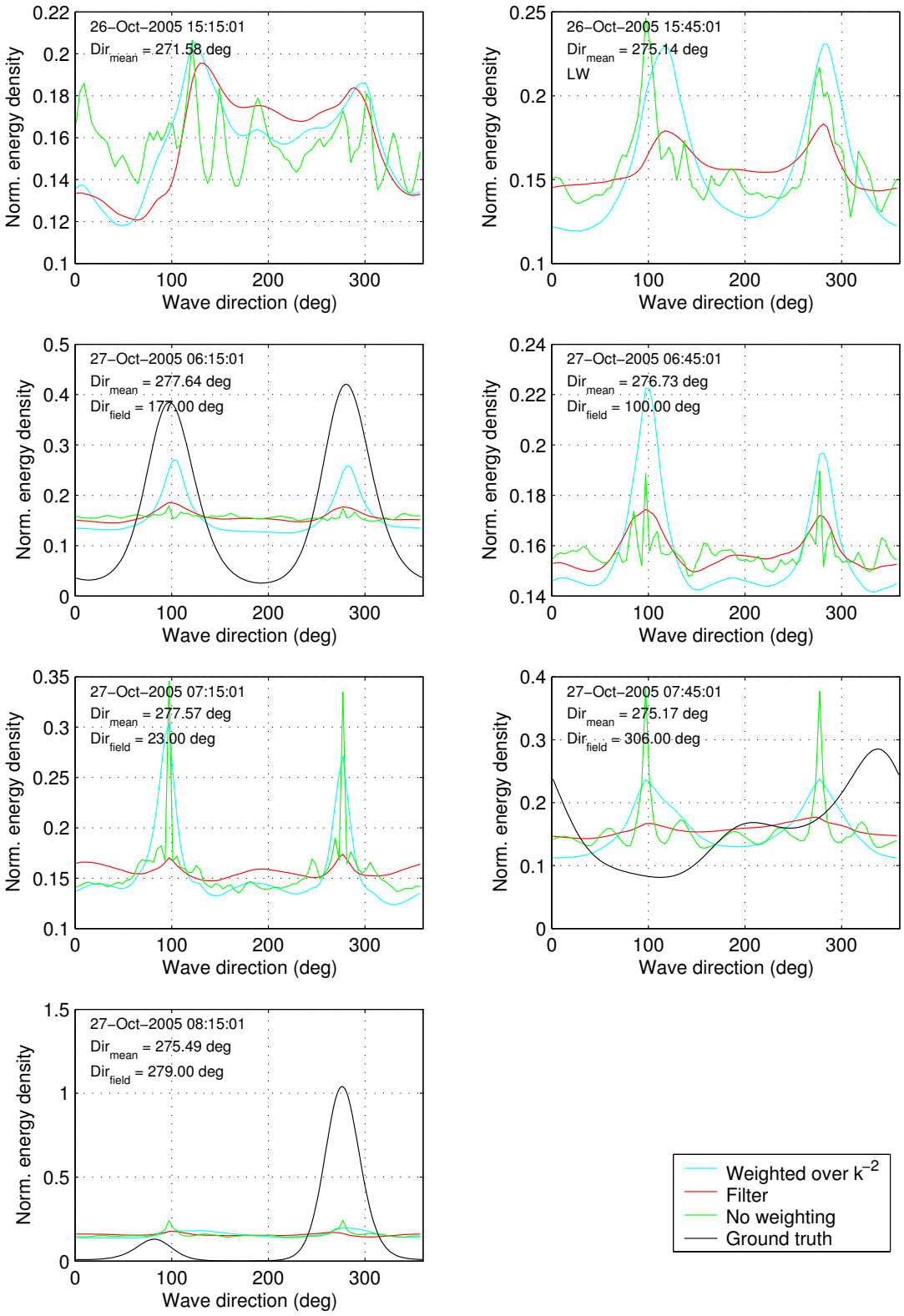
26–Oct–2005 15:15:01
Dir mean = 271.58 deg
26–Oct–2005 15:45:01
Dir mean = 275.14 deg
LW
27–Oct–2005 06:15:01
Dir mean = 277.64 deg
Dir field = 177.00 deg
27–Oct–2005 06:45:01
Dir mean = 276.73 deg
Dir field = 100.00 deg
27–Oct–2005 07:15:01
Dir mean = 277.57 deg
Dir field = 23.00 deg
27–Oct–2005 07:45:01
Dir mean = 275.17 deg
Dir field = 306.00 deg
27–Oct–2005 08:15:01
Dir mean = 275.49 deg
Dir field = 279.00 deg
Norm. energy density
Wave direction (deg)
Weighted over k−2
Filter
No weighting
Ground truth

a–246.25

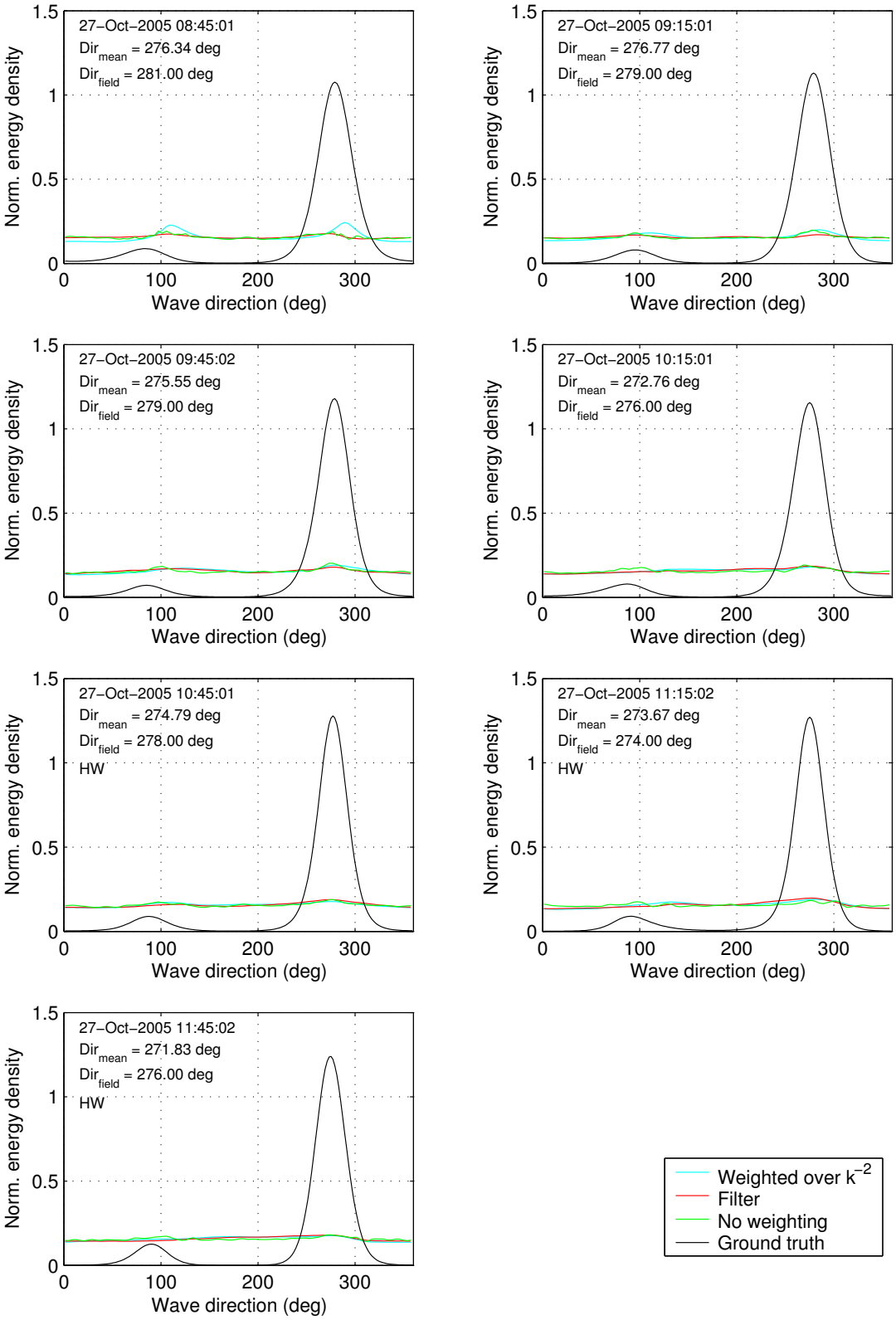
27–Oct–2005 08:45:01
Dir$_{mean}$ = 276.34 deg
Dir$_{field}$ = 281.00 deg
27–Oct–2005 09:15:01
Dir$_{mean}$ = 276.77 deg
Dir$_{field}$ = 279.00 deg
27–Oct–2005 09:45:02
Dir$_{mean}$ = 275.55 deg
Dir$_{field}$ = 279.00 deg
27–Oct–2005 10:15:01
Dir$_{mean}$ = 272.76 deg
Dir$_{field}$ = 276.00 deg
27–Oct–2005 10:45:01
Dir$_{mean}$ = 274.79 deg
Dir$_{field}$ = 278.00 deg
HW
27–Oct–2005 11:15:02
Dir$_{mean}$ = 273.67 deg
Dir$_{field}$ = 274.00 deg
HW
27–Oct–2005 11:45:02
Dir$_{mean}$ = 271.83 deg
Dir$_{field}$ = 276.00 deg
HW
Norm. energy density
Wave direction (deg)
0
0.5
1
1.5
100
200
300
Weighted over k^{-2}
Filter
No weighting
Ground truth

a–246.25

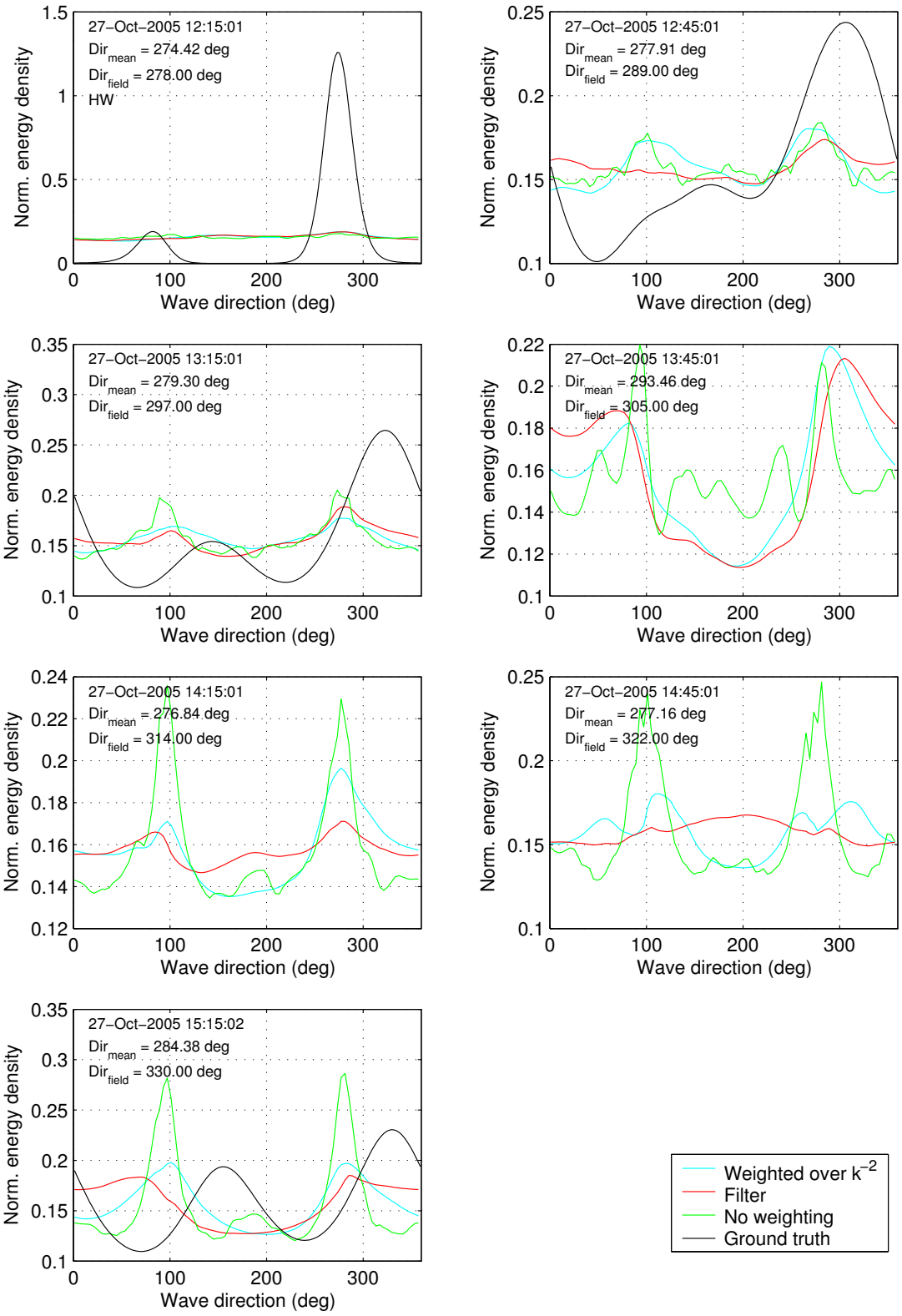
27–Oct–2005 12:15:01
Dir_mean = 274.42 deg
Dir_field = 278.00 deg
HW
27–Oct–2005 12:45:01
Dir_mean = 277.91 deg
Dir_field = 289.00 deg
27–Oct–2005 13:15:01
Dir_mean = 279.30 deg
Dir_field = 297.00 deg
27–Oct–2005 13:45:01
Dir_mean = 293.46 deg
Dir_field = 305.00 deg
27–Oct–2005 14:15:01
Dir_mean = 276.84 deg
Dir_field = 314.00 deg
27–Oct–2005 14:45:01
Dir_mean = 277.16 deg
Dir_field = 322.00 deg
27–Oct–2005 15:15:02
Dir_mean = 284.38 deg
Dir_field = 330.00 deg
Norm. energy density
Wave direction (deg)
Weighted over k^-2
Filter
No weighting
Ground truth

a–246.25

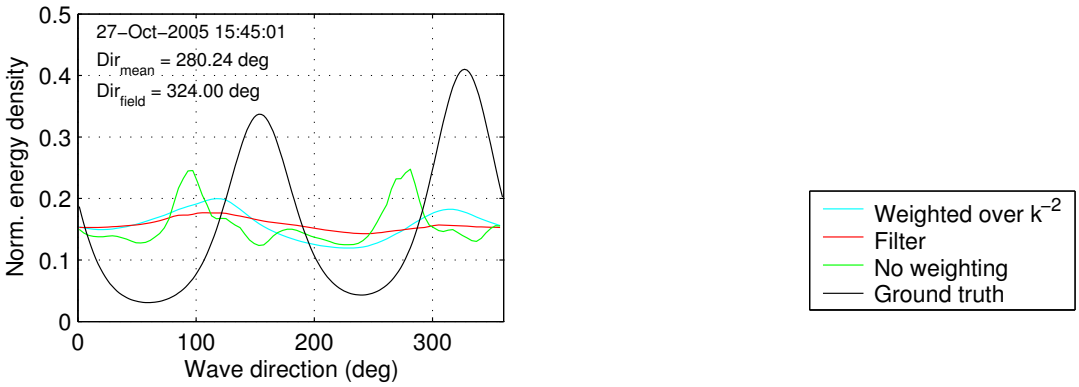
27–Oct–2005 15:45:01
Dir$_{mean}$ = 280.24 deg
Dir$_{field}$ = 324.00 deg
Norm. energy density
0
0.1
0.2
0.3
0.4
0.5
0
100
200
300
Wave direction (deg)
Weighted over k^{-2}
Filter
No weighting
Ground truth

a–246.31

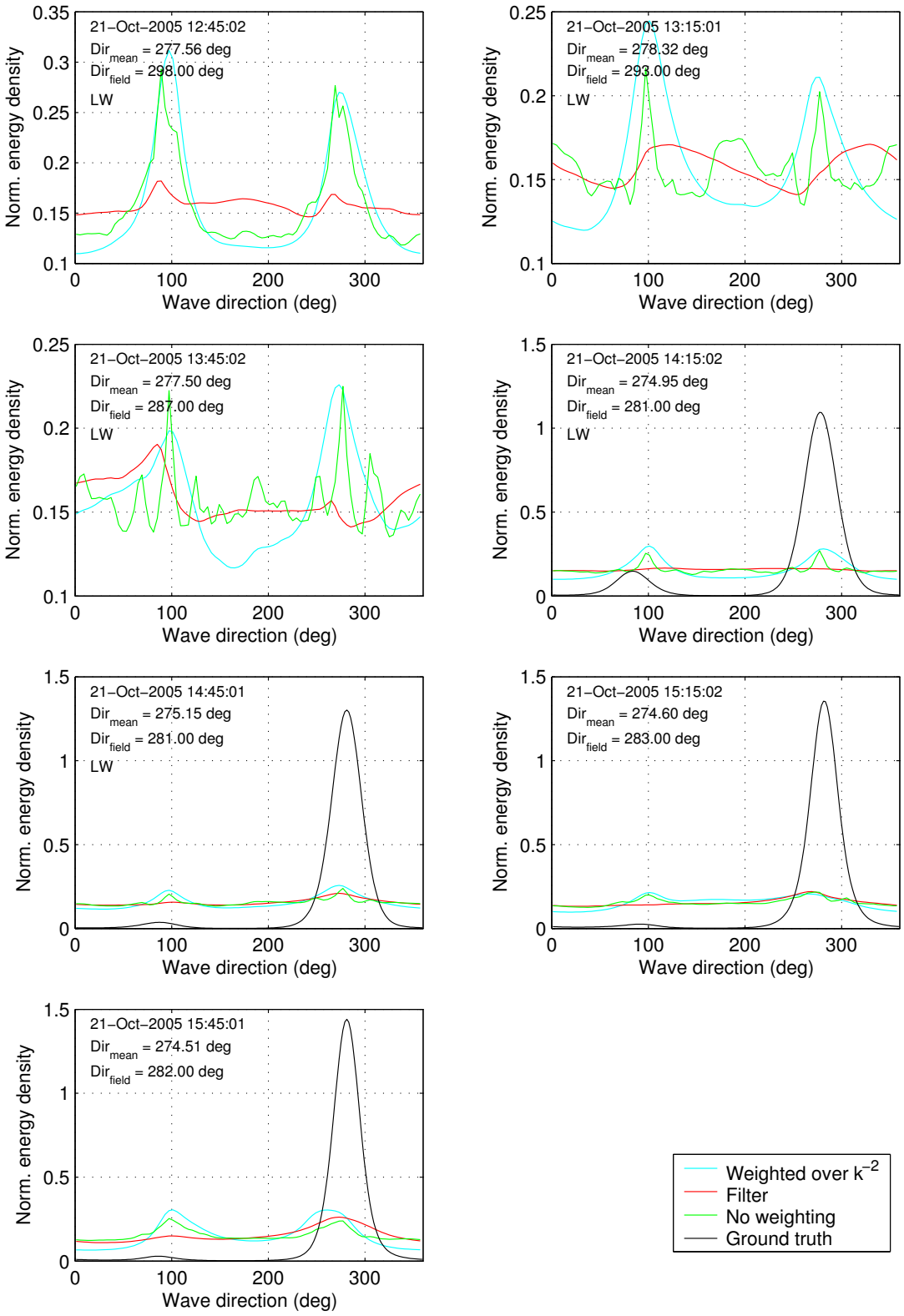
21–Oct–2005 12:45:02
Dir_mean = 277.56 deg
Dir_field = 298.00 deg
LW
21–Oct–2005 13:15:01
Dir_mean = 278.32 deg
Dir_field = 293.00 deg
LW
21–Oct–2005 13:45:02
Dir_mean = 277.50 deg
Dir_field = 287.00 deg
LW
21–Oct–2005 14:15:02
Dir_mean = 274.95 deg
Dir_field = 281.00 deg
LW
21–Oct–2005 14:45:01
Dir_mean = 275.15 deg
Dir_field = 281.00 deg
LW
21–Oct–2005 15:15:02
Dir_mean = 274.60 deg
Dir_field = 283.00 deg
21–Oct–2005 15:45:01
Dir_mean = 274.51 deg
Dir_field = 282.00 deg
Norm. energy density
Wave direction (deg)
Weighted over k^-2
Filter
No weighting
Ground truth

a–246.31

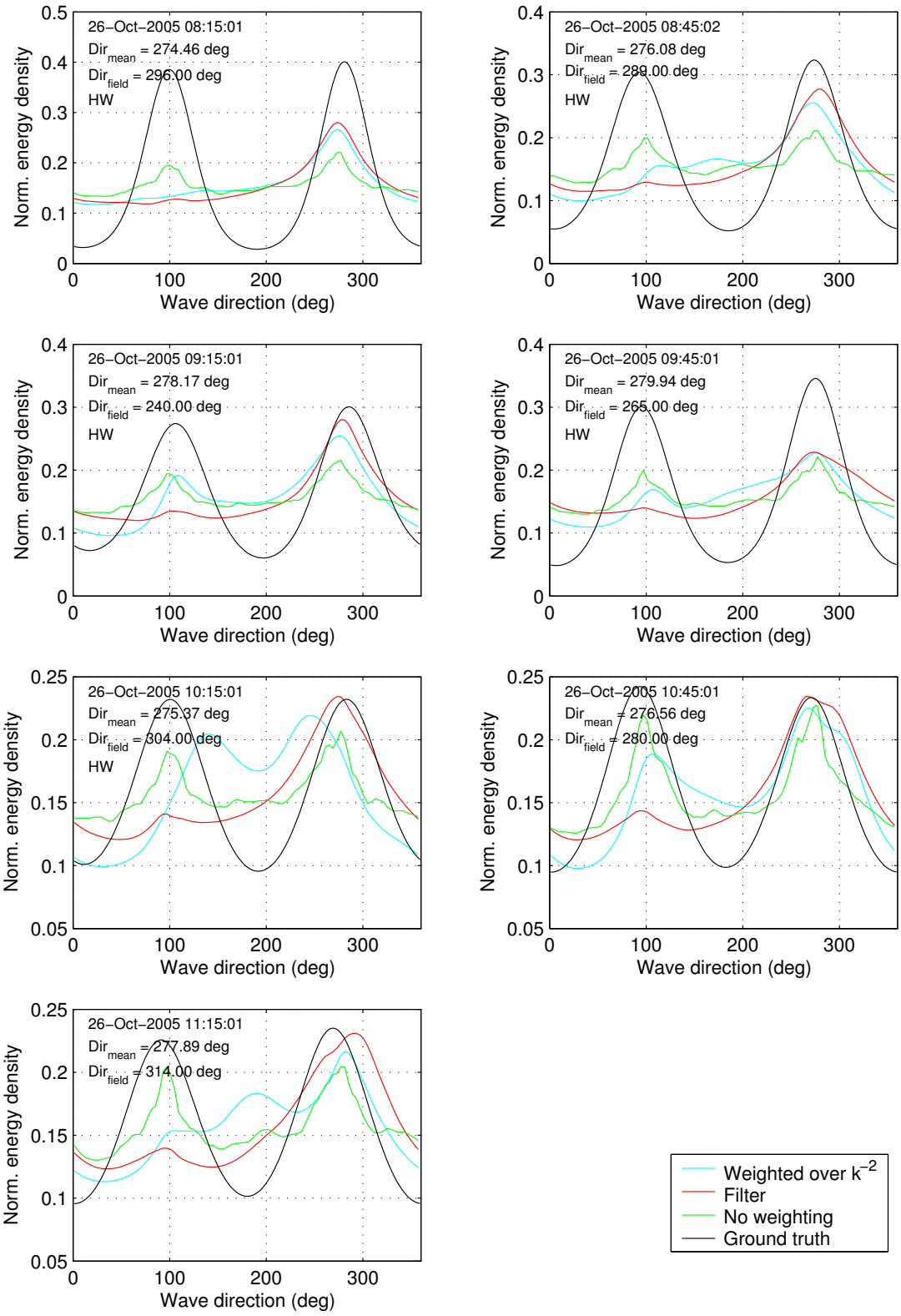
26–Oct–2005 08:15:01
Dir_mean = 274.46 deg
Dir_field = 296.00 deg
HW
26–Oct–2005 08:45:02
Dir_mean = 276.08 deg
Dir_field = 289.00 deg
HW
26–Oct–2005 09:15:01
Dir_mean = 278.17 deg
Dir_field = 240.00 deg
HW
26–Oct–2005 09:45:01
Dir_mean = 279.94 deg
Dir_field = 265.00 deg
HW
26–Oct–2005 10:15:01
Dir_mean = 275.37 deg
Dir_field = 304.00 deg
HW
26–Oct–2005 10:45:01
Dir_mean = 276.56 deg
Dir_field = 280.00 deg
26–Oct–2005 11:15:01
Dir_mean = 277.89 deg
Dir_field = 314.00 deg
Norm. energy density
Wave direction (deg)
Weighted over k^-2
Filter
No weighting
Ground truth

a–246.31

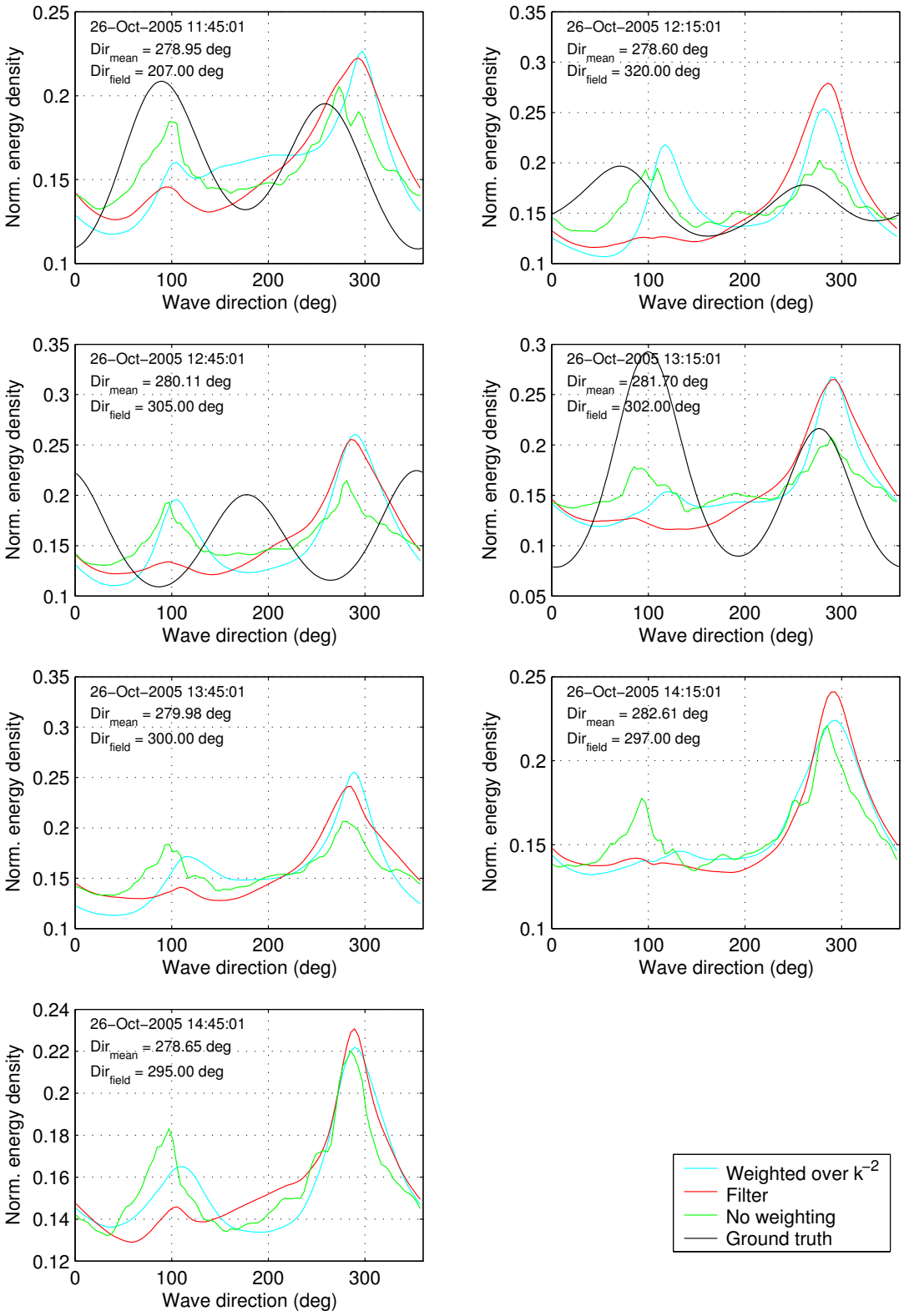
26–Oct–2005 11:45:01
Dir_mean = 278.95 deg
Dir_field = 207.00 deg
26–Oct–2005 12:15:01
Dir_mean = 278.60 deg
Dir_field = 320.00 deg
26–Oct–2005 12:45:01
Dir_mean = 280.11 deg
Dir_field = 305.00 deg
26–Oct–2005 13:15:01
Dir_mean = 281.70 deg
Dir_field = 302.00 deg
26–Oct–2005 13:45:01
Dir_mean = 279.98 deg
Dir_field = 300.00 deg
26–Oct–2005 14:15:01
Dir_mean = 282.61 deg
Dir_field = 297.00 deg
26–Oct–2005 14:45:01
Dir_mean = 278.65 deg
Dir_field = 295.00 deg
Norm. energy density
Wave direction (deg)
Weighted over k^-2
Filter
No weighting
Ground truth

a–246.31

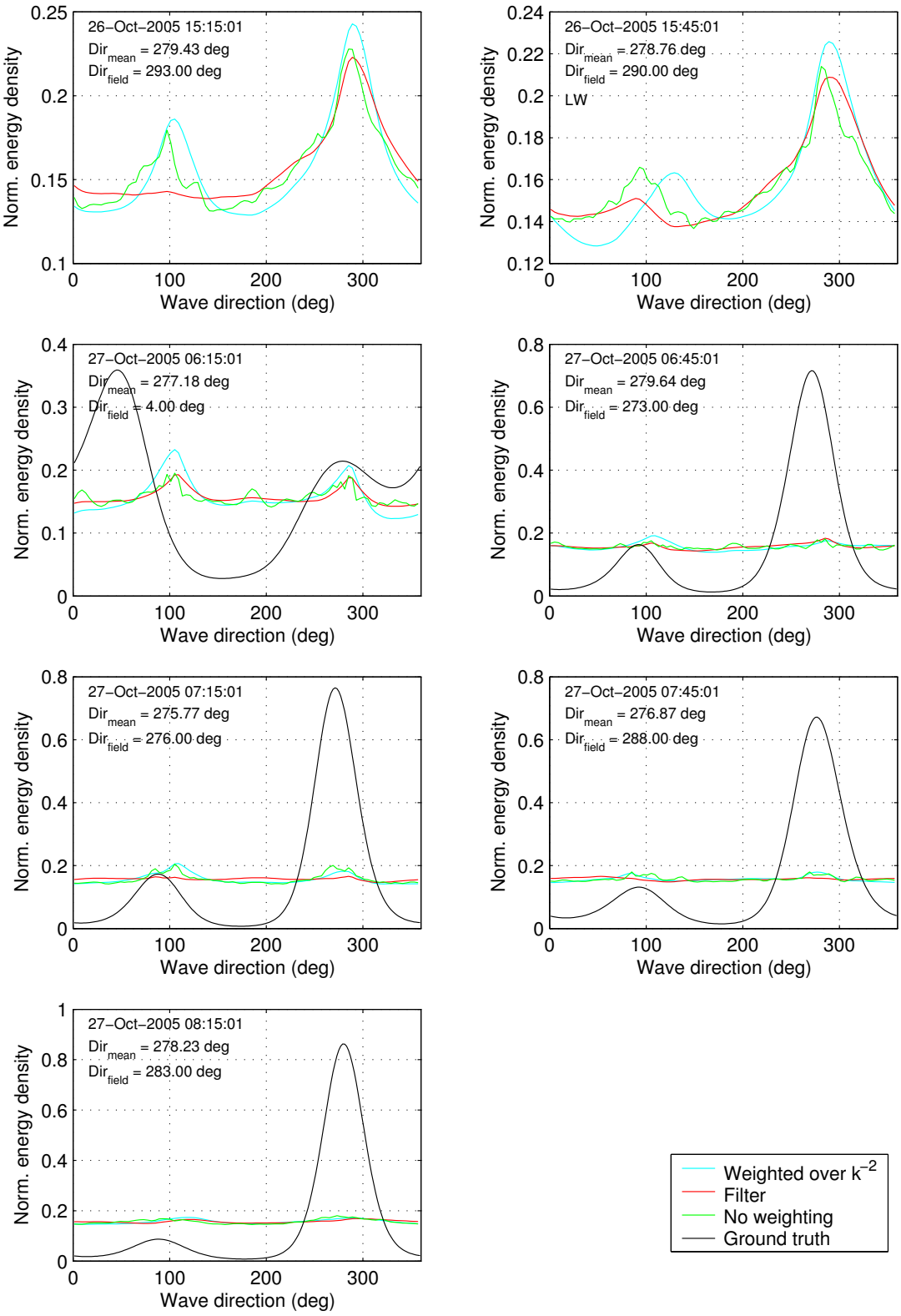
26–Oct–2005 15:15:01
Dir mean = 279.43 deg
Dir field = 293.00 deg
26–Oct–2005 15:45:01
Dir mean = 278.76 deg
Dir field = 290.00 deg
LW
27–Oct–2005 06:15:01
Dir mean = 277.18 deg
Dir field = 4.00 deg
27–Oct–2005 06:45:01
Dir mean = 279.64 deg
Dir field = 273.00 deg
27–Oct–2005 07:15:01
Dir mean = 275.77 deg
Dir field = 276.00 deg
27–Oct–2005 07:45:01
Dir mean = 276.87 deg
Dir field = 288.00 deg
27–Oct–2005 08:15:01
Dir mean = 278.23 deg
Dir field = 283.00 deg
Norm. energy density
Wave direction (deg)
Weighted over k−2
Filter
No weighting
Ground truth

a–246.31

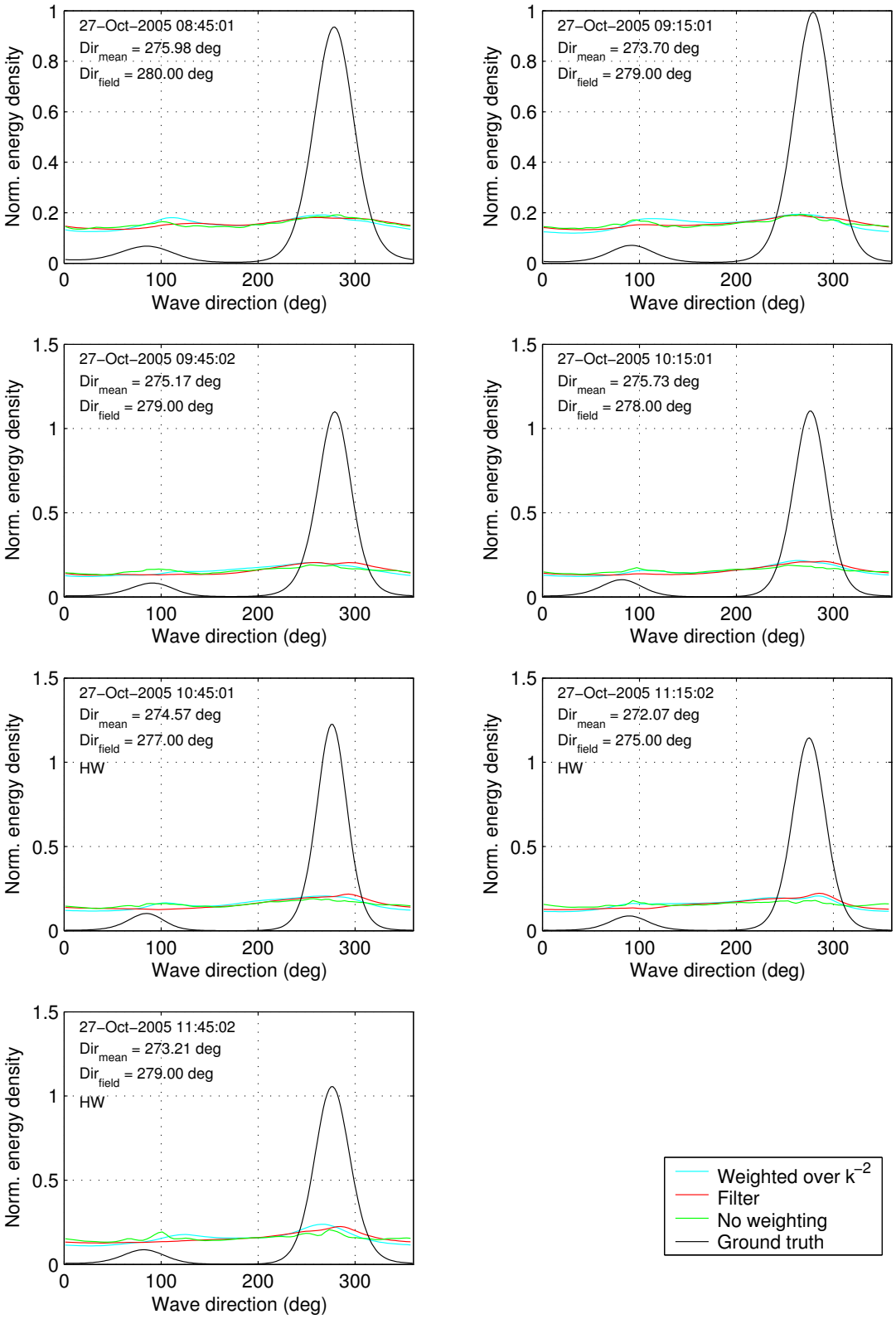
27–Oct–2005 08:45:01
Dir$_{mean}$ = 275.98 deg
Dir$_{field}$ = 280.00 deg
27–Oct–2005 09:15:01
Dir$_{mean}$ = 273.70 deg
Dir$_{field}$ = 279.00 deg
27–Oct–2005 09:45:02
Dir$_{mean}$ = 275.17 deg
Dir$_{field}$ = 279.00 deg
27–Oct–2005 10:15:01
Dir$_{mean}$ = 275.73 deg
Dir$_{field}$ = 278.00 deg
27–Oct–2005 10:45:01
Dir$_{mean}$ = 274.57 deg
Dir$_{field}$ = 277.00 deg
HW
27–Oct–2005 11:15:02
Dir$_{mean}$ = 272.07 deg
Dir$_{field}$ = 275.00 deg
HW
27–Oct–2005 11:45:02
Dir$_{mean}$ = 273.21 deg
Dir$_{field}$ = 279.00 deg
HW
Norm. energy density
Wave direction (deg)
Weighted over k^{-2}
Filter
No weighting
Ground truth

a–246.31

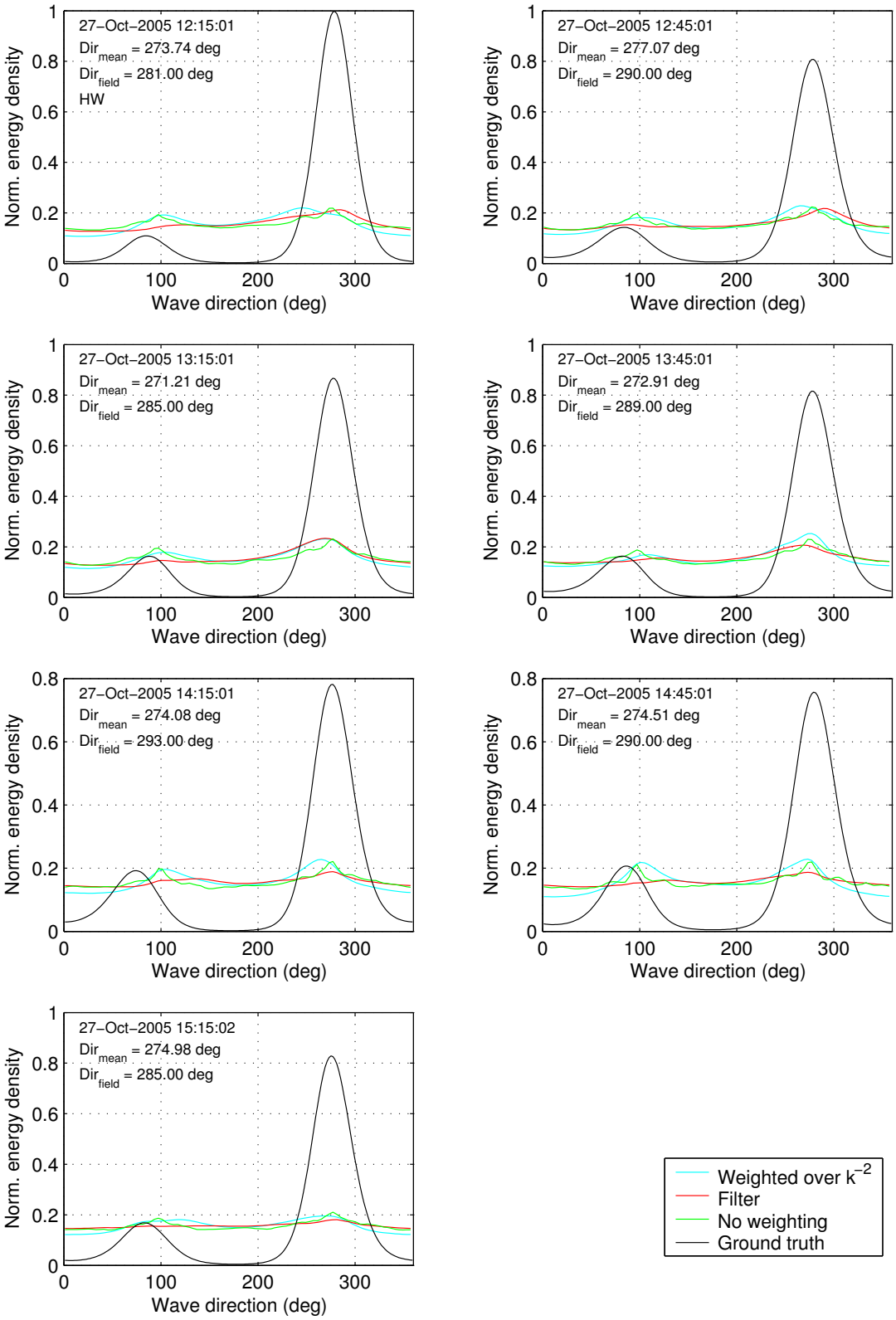
27–Oct–2005 12:15:01
Dir$_{mean}$ = 273.74 deg
Dir$_{field}$ = 281.00 deg
HW
27–Oct–2005 12:45:01
Dir$_{mean}$ = 277.07 deg
Dir$_{field}$ = 290.00 deg
27–Oct–2005 13:15:01
Dir$_{mean}$ = 271.21 deg
Dir$_{field}$ = 285.00 deg
27–Oct–2005 13:45:01
Dir$_{mean}$ = 272.91 deg
Dir$_{field}$ = 289.00 deg
27–Oct–2005 14:15:01
Dir$_{mean}$ = 274.08 deg
Dir$_{field}$ = 293.00 deg
27–Oct–2005 14:45:01
Dir$_{mean}$ = 274.51 deg
Dir$_{field}$ = 290.00 deg
27–Oct–2005 15:15:02
Dir$_{mean}$ = 274.98 deg
Dir$_{field}$ = 285.00 deg
Norm. energy density
Wave direction (deg)
Weighted over k^{-2}
Filter
No weighting
Ground truth

a–246.31

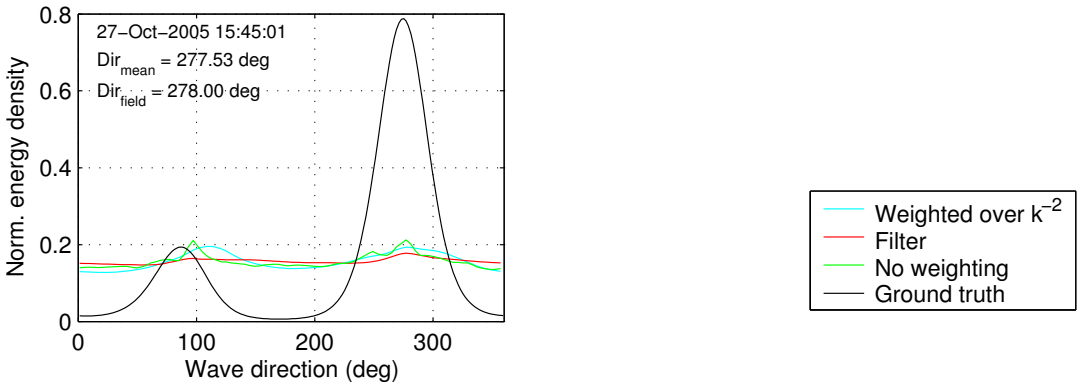
27–Oct–2005 15:45:01
Dir$_{mean}$ = 277.53 deg
Dir$_{field}$ = 278.00 deg
Norm. energy density
0.8
0.6
0.4
0.2
0
0
100
200
300
Wave direction (deg)
Weighted over k^{-2}
Filter
No weighting
Ground truth

a–246.37

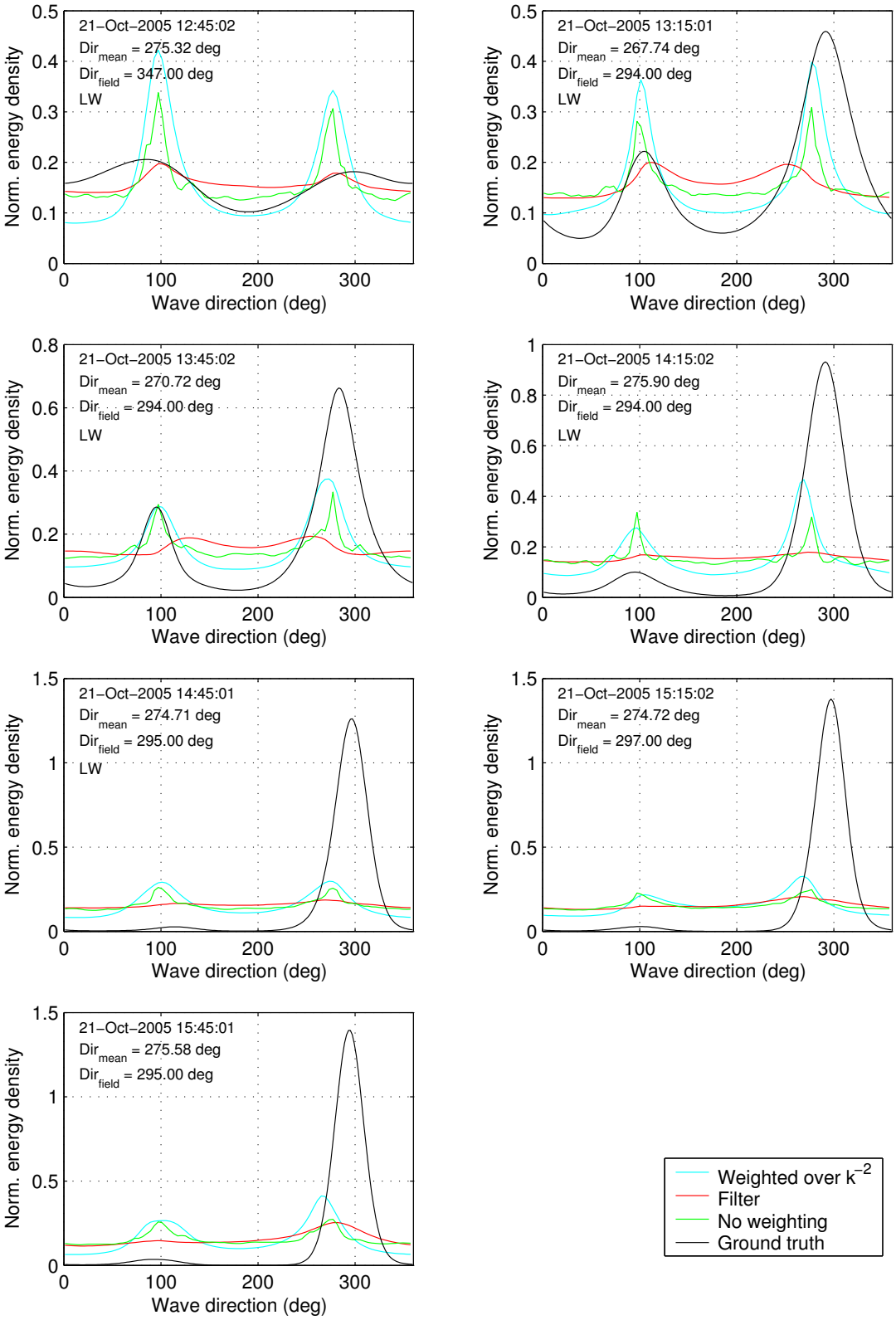
21–Oct–2005 12:45:02
Dir_mean = 275.32 deg
Dir_field = 347.00 deg
LW
21–Oct–2005 13:15:01
Dir_mean = 267.74 deg
Dir_field = 294.00 deg
LW
21–Oct–2005 13:45:02
Dir_mean = 270.72 deg
Dir_field = 294.00 deg
LW
21–Oct–2005 14:15:02
Dir_mean = 275.90 deg
Dir_field = 294.00 deg
LW
21–Oct–2005 14:45:01
Dir_mean = 274.71 deg
Dir_field = 295.00 deg
LW
21–Oct–2005 15:15:02
Dir_mean = 274.72 deg
Dir_field = 297.00 deg
21–Oct–2005 15:45:01
Dir_mean = 275.58 deg
Dir_field = 295.00 deg
Norm. energy density
Wave direction (deg)
Weighted over k^-2
Filter
No weighting
Ground truth

a–246.37

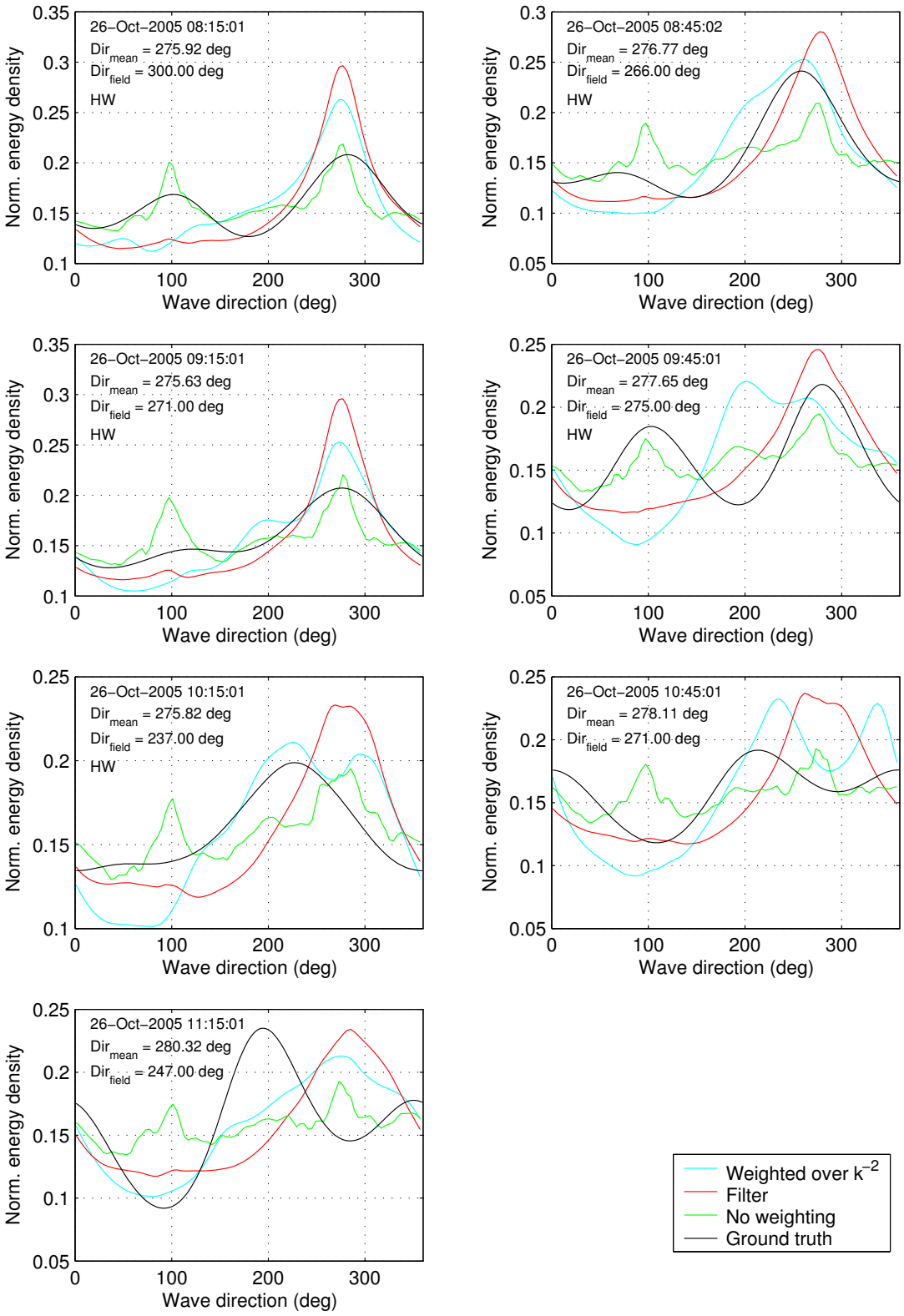
26–Oct–2005 08:15:01
Dir_mean = 275.92 deg
Dir_field = 300.00 deg
HW
26–Oct–2005 08:45:02
Dir_mean = 276.77 deg
Dir_field = 266.00 deg
HW
26–Oct–2005 09:15:01
Dir_mean = 275.63 deg
Dir_field = 271.00 deg
HW
26–Oct–2005 09:45:01
Dir_mean = 277.65 deg
Dir_field = 275.00 deg
HW
26–Oct–2005 10:15:01
Dir_mean = 275.82 deg
Dir_field = 237.00 deg
HW
26–Oct–2005 10:45:01
Dir_mean = 278.11 deg
Dir_field = 271.00 deg
26–Oct–2005 11:15:01
Dir_mean = 280.32 deg
Dir_field = 247.00 deg
Norm. energy density
Wave direction (deg)
Weighted over k^-2
Filter
No weighting
Ground truth

a–246.37

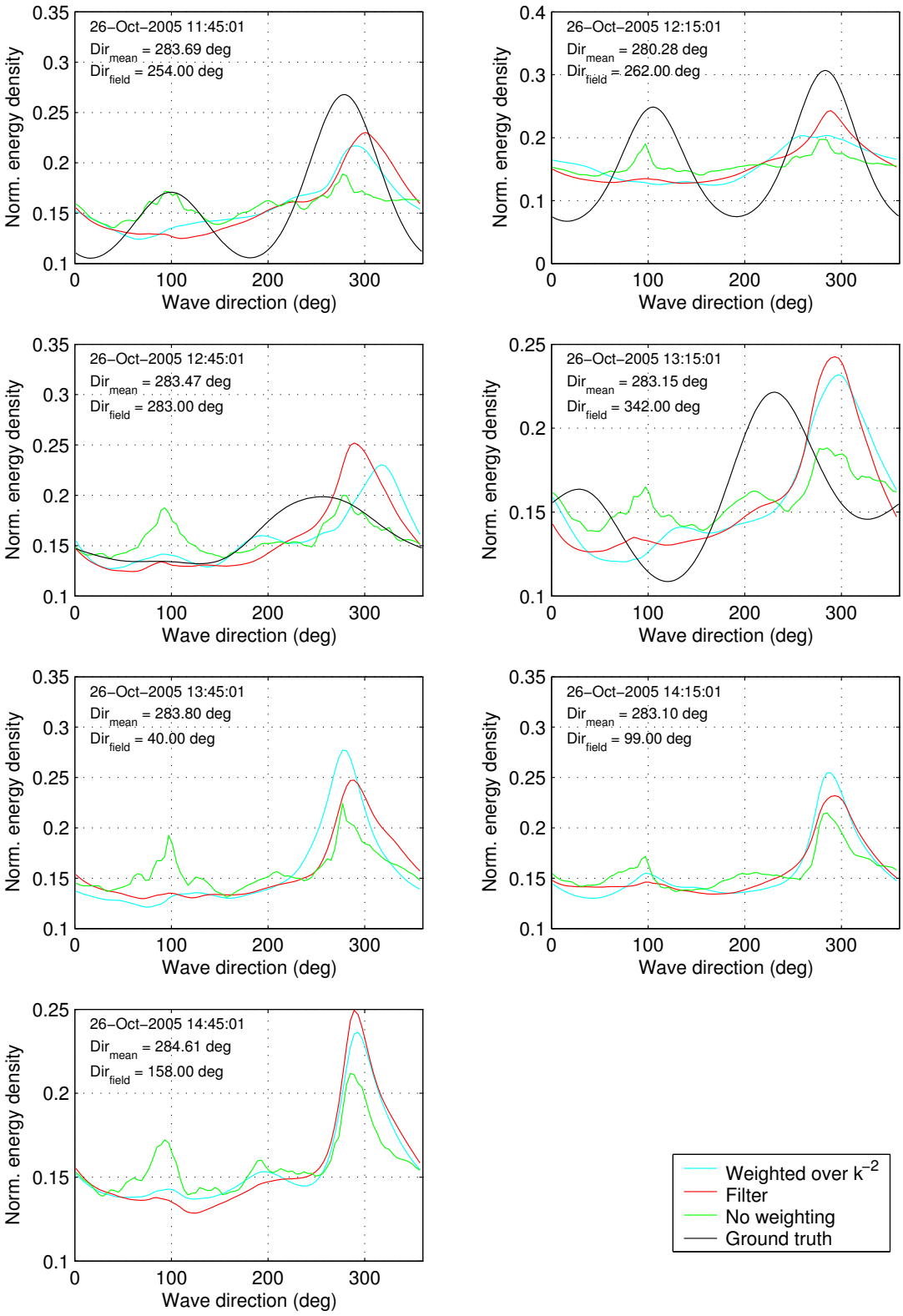
26–Oct–2005 11:45:01
Dir_mean = 283.69 deg
Dir_field = 254.00 deg
26–Oct–2005 12:15:01
Dir_mean = 280.28 deg
Dir_field = 262.00 deg
26–Oct–2005 12:45:01
Dir_mean = 283.47 deg
Dir_field = 283.00 deg
26–Oct–2005 13:15:01
Dir_mean = 283.15 deg
Dir_field = 342.00 deg
26–Oct–2005 13:45:01
Dir_mean = 283.80 deg
Dir_field = 40.00 deg
26–Oct–2005 14:15:01
Dir_mean = 283.10 deg
Dir_field = 99.00 deg
26–Oct–2005 14:45:01
Dir_mean = 284.61 deg
Dir_field = 158.00 deg
Norm. energy density
Wave direction (deg)
Weighted over k^-2
Filter
No weighting
Ground truth

a–246.37

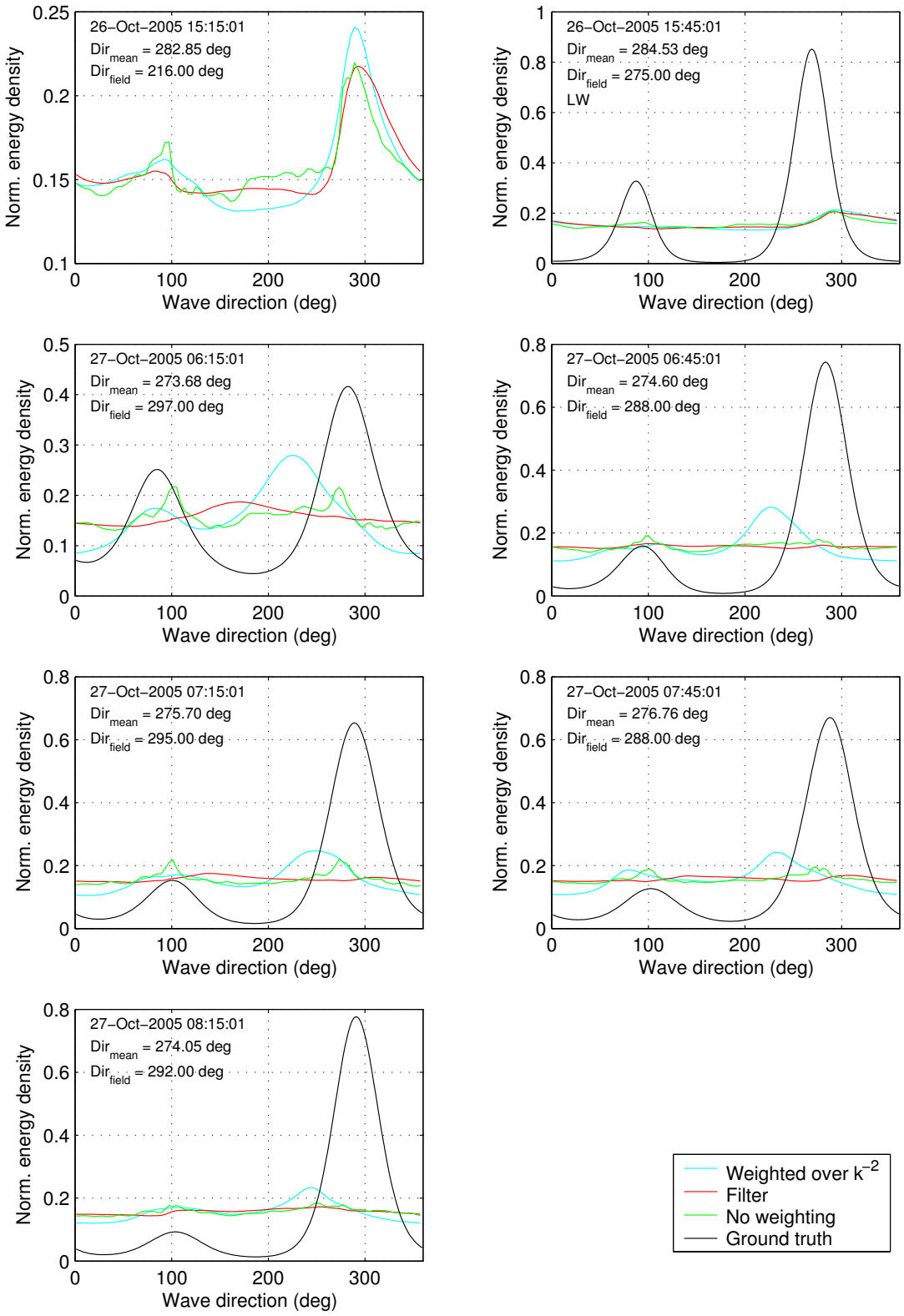
26–Oct–2005 15:15:01
Dir$_{mean}$ = 282.85 deg
Dir$_{field}$ = 216.00 deg
26–Oct–2005 15:45:01
Dir$_{mean}$ = 284.53 deg
Dir$_{field}$ = 275.00 deg
LW
27–Oct–2005 06:15:01
Dir$_{mean}$ = 273.68 deg
Dir$_{field}$ = 297.00 deg
27–Oct–2005 06:45:01
Dir$_{mean}$ = 274.60 deg
Dir$_{field}$ = 288.00 deg
27–Oct–2005 07:15:01
Dir$_{mean}$ = 275.70 deg
Dir$_{field}$ = 295.00 deg
27–Oct–2005 07:45:01
Dir$_{mean}$ = 276.76 deg
Dir$_{field}$ = 288.00 deg
27–Oct–2005 08:15:01
Dir$_{mean}$ = 274.05 deg
Dir$_{field}$ = 292.00 deg
Norm. energy density
Wave direction (deg)
Weighted over k^{-2}
Filter
No weighting
Ground truth

a–246.37

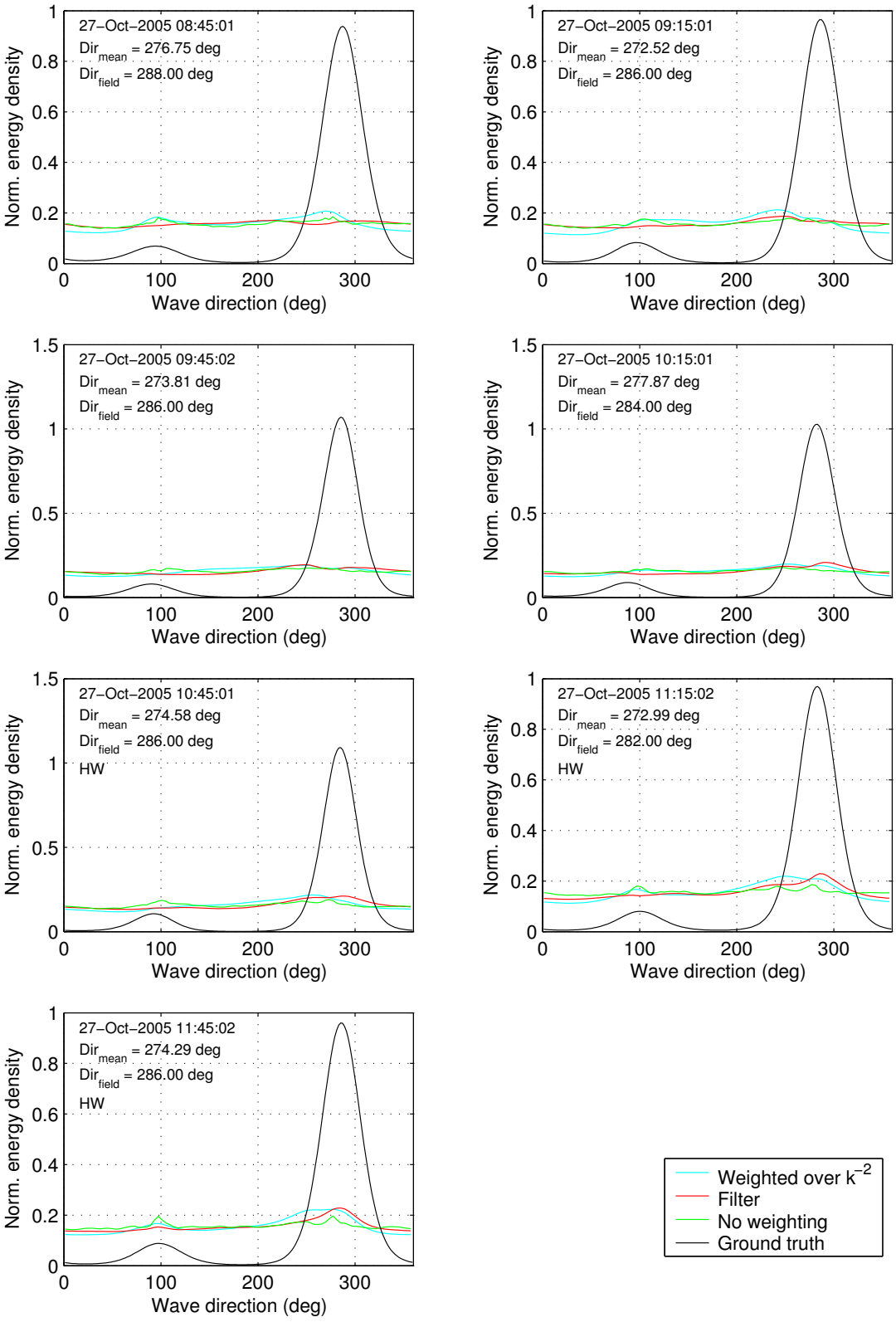
27–Oct–2005 08:45:01
Dir_mean = 276.75 deg
Dir_field = 288.00 deg
27–Oct–2005 09:15:01
Dir_mean = 272.52 deg
Dir_field = 286.00 deg
27–Oct–2005 09:45:02
Dir_mean = 273.81 deg
Dir_field = 286.00 deg
27–Oct–2005 10:15:01
Dir_mean = 277.87 deg
Dir_field = 284.00 deg
27–Oct–2005 10:45:01
Dir_mean = 274.58 deg
Dir_field = 286.00 deg
HW
27–Oct–2005 11:15:02
Dir_mean = 272.99 deg
Dir_field = 282.00 deg
HW
27–Oct–2005 11:45:02
Dir_mean = 274.29 deg
Dir_field = 286.00 deg
HW
Norm. energy density
Wave direction (deg)
Weighted over k^-2
Filter
No weighting
Ground truth

a–246.37

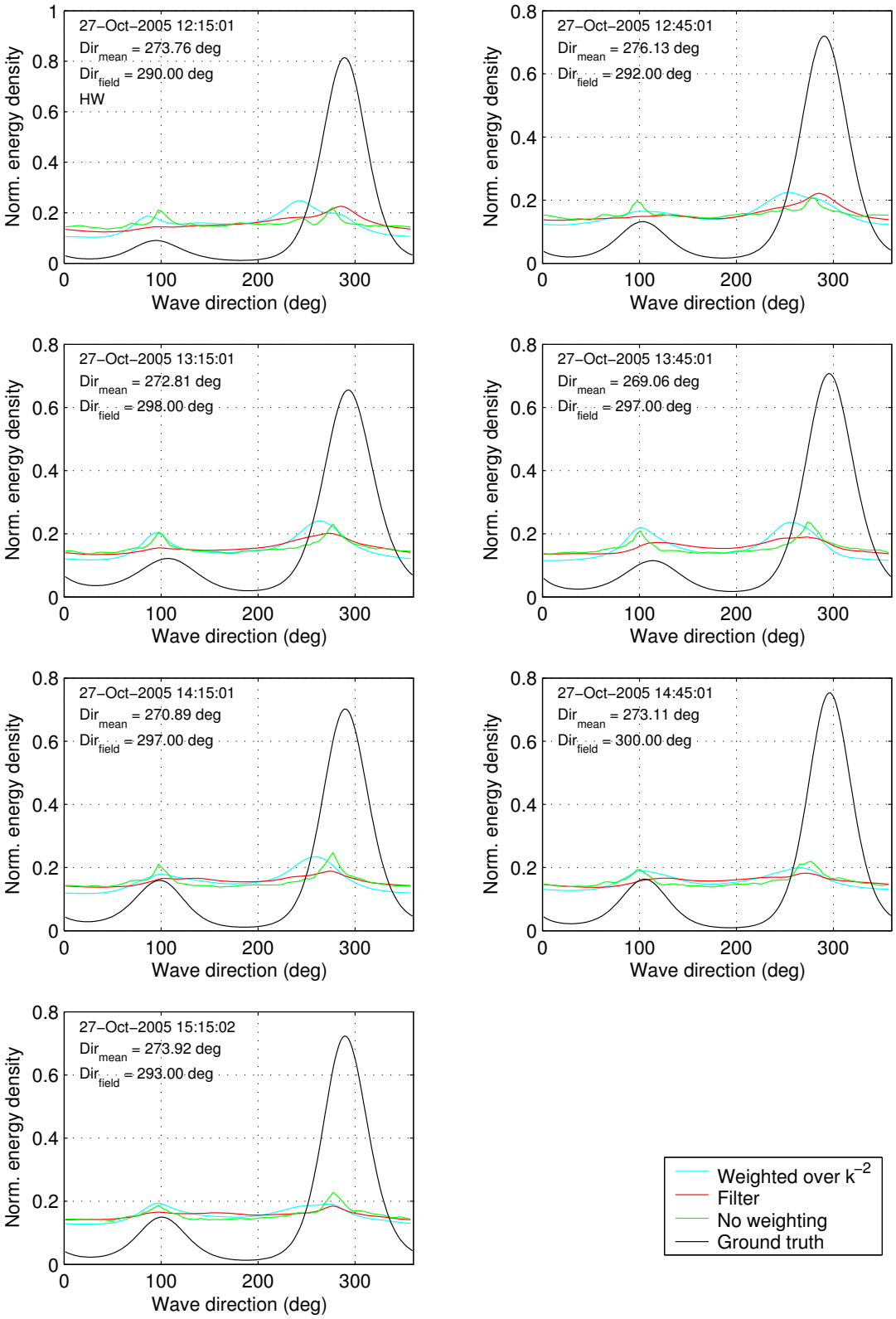
27–Oct–2005 12:15:01
Dir_mean = 273.76 deg
Dir_field = 290.00 deg
HW
27–Oct–2005 12:45:01
Dir_mean = 276.13 deg
Dir_field = 292.00 deg
27–Oct–2005 13:15:01
Dir_mean = 272.81 deg
Dir_field = 298.00 deg
27–Oct–2005 13:45:01
Dir_mean = 269.06 deg
Dir_field = 297.00 deg
27–Oct–2005 14:15:01
Dir_mean = 270.89 deg
Dir_field = 297.00 deg
27–Oct–2005 14:45:01
Dir_mean = 273.11 deg
Dir_field = 300.00 deg
27–Oct–2005 15:15:02
Dir_mean = 273.92 deg
Dir_field = 293.00 deg
Norm. energy density
Wave direction (deg)
Weighted over k^-2
Filter
No weighting
Ground truth

a–246.37

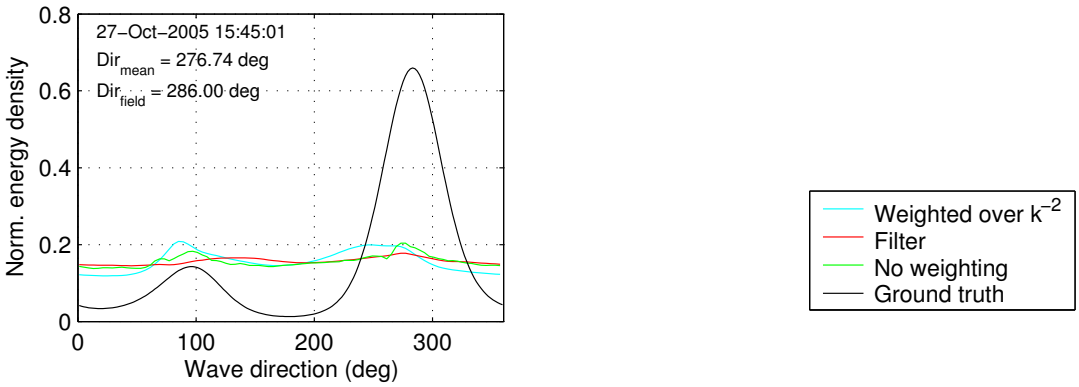
27–Oct–2005 15:45:01
Dir$_{mean}$ = 276.74 deg
Dir$_{field}$ = 286.00 deg
Norm. energy density
0
0.2
0.4
0.6
0.8
0
100
200
300
Wave direction (deg)
Weighted over k^{-2}
Filter
No weighting
Ground truth

D Results wave period and direction

D.1 Intertidal area

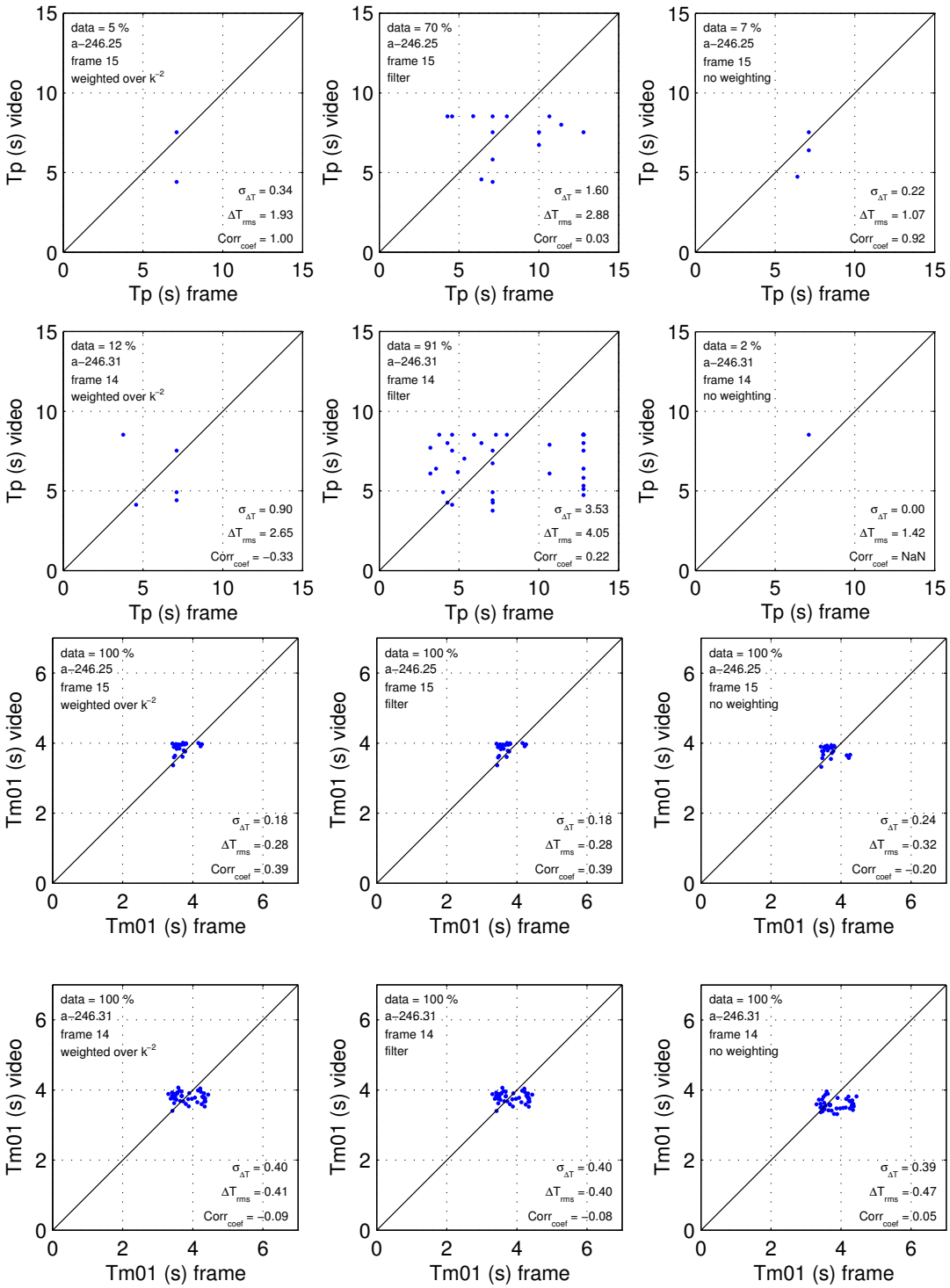

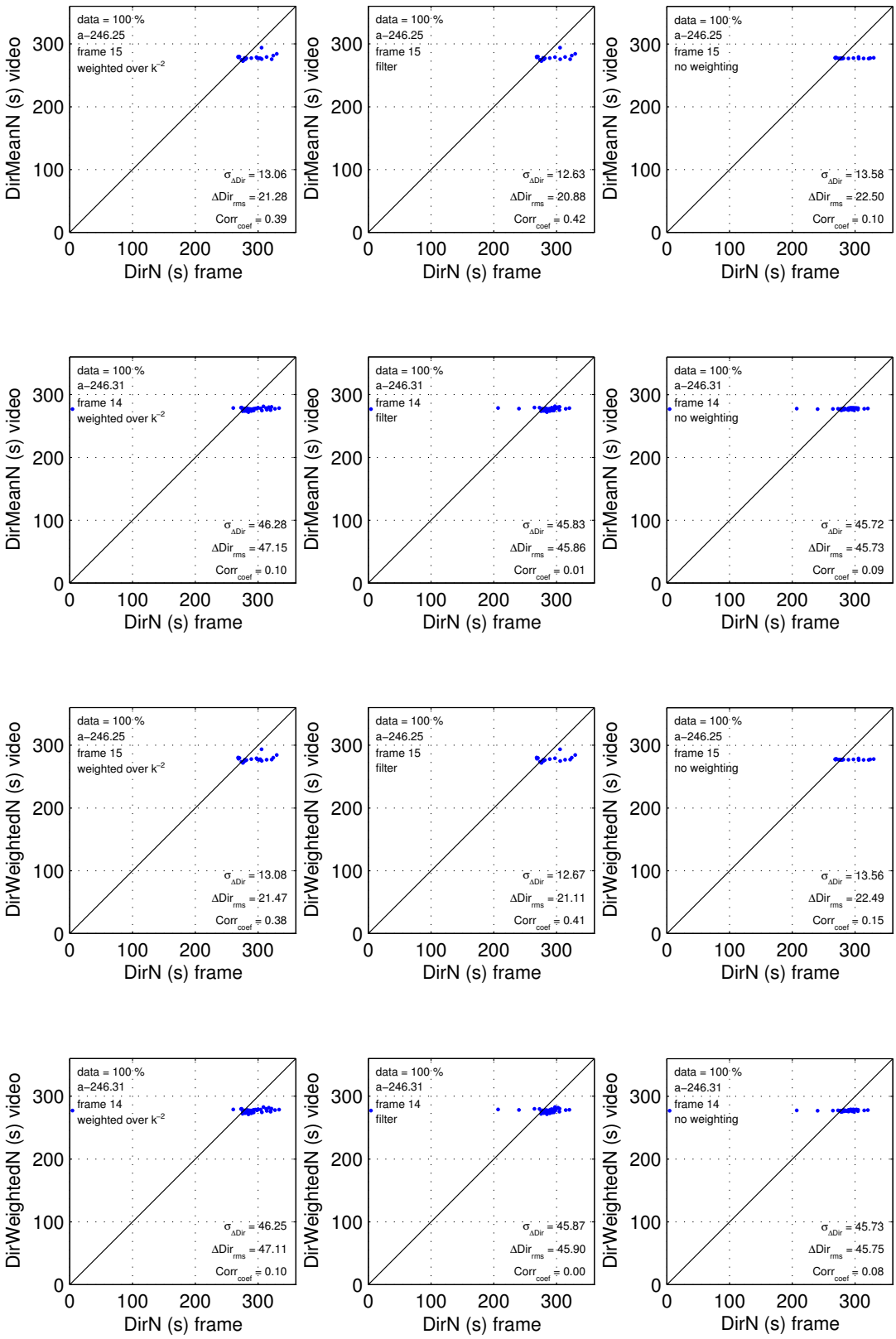
data = 100 %
a–246.25
frame 15
weighted over k^-2
σ_ΔDir = 13.06
ΔDir_rms = 21.28
Corr_coef = 0.39
data = 100 %
a–246.25
frame 15
filter
σ_ΔDir = 12.63
ΔDir_rms = 20.88
Corr_coef = 0.42
data = 100 %
a–246.25
frame 15
no weighting
σ_ΔDir = 13.58
ΔDir_rms = 22.50
Corr_coef = 0.10
data = 100 %
a–246.31
frame 14
weighted over k^-2
σ_ΔDir = 46.28
ΔDir_rms = 47.15
Corr_coef = 0.10
data = 100 %
a–246.31
frame 14
filter
σ_ΔDir = 45.83
ΔDir_rms = 45.86
Corr_coef = 0.01
data = 100 %
a–246.31
frame 14
no weighting
σ_ΔDir = 45.72
ΔDir_rms = 45.73
Corr_coef = 0.09
data = 100 %
a–246.25
frame 15
weighted over k^-2
σ_ΔDir = 13.08
ΔDir_rms = 21.47
Corr_coef = 0.38
data = 100 %
a–246.25
frame 15
filter
σ_ΔDir = 12.67
ΔDir_rms = 21.11
Corr_coef = 0.41
data = 100 %
a–246.25
frame 15
no weighting
σ_ΔDir = 13.56
ΔDir_rms = 22.49
Corr_coef = 0.15
data = 100 %
a–246.31
frame 14
weighted over k^-2
σ_ΔDir = 46.25
ΔDir_rms = 47.11
Corr_coef = 0.10
data = 100 %
a–246.31
frame 14
filter
σ_ΔDir = 45.87
ΔDir_rms = 45.90
Corr_coef = 0.00
data = 100 %
a–246.31
frame 14
no weighting
σ_ΔDir = 45.73
ΔDir_rms = 45.75
Corr_coef = 0.08
DirMeanN (s) video
DirWeightedN (s) video
DirN (s) frame
0
100
200
300

D.2 Shoaling region

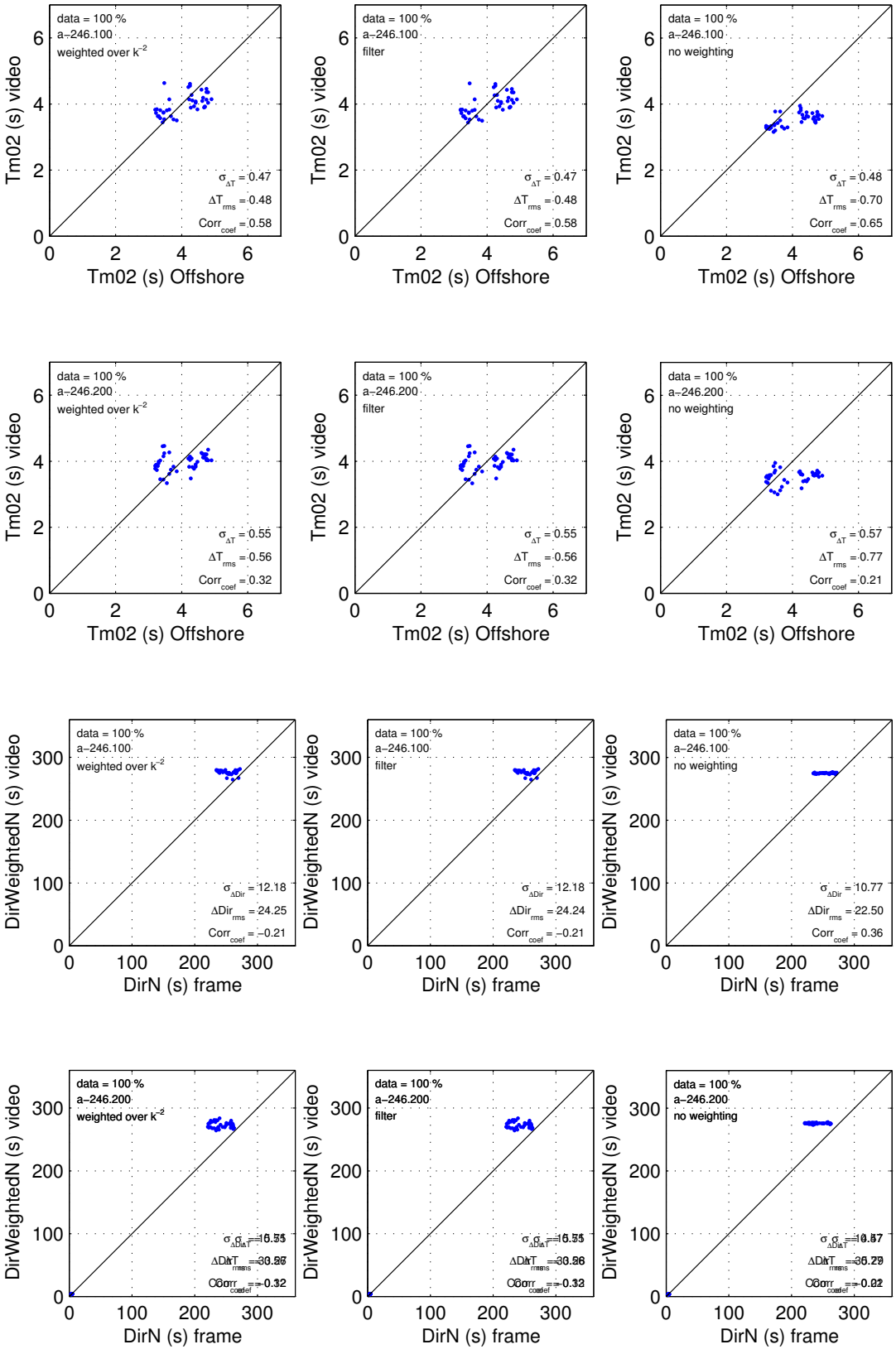

E Time lag and correlation

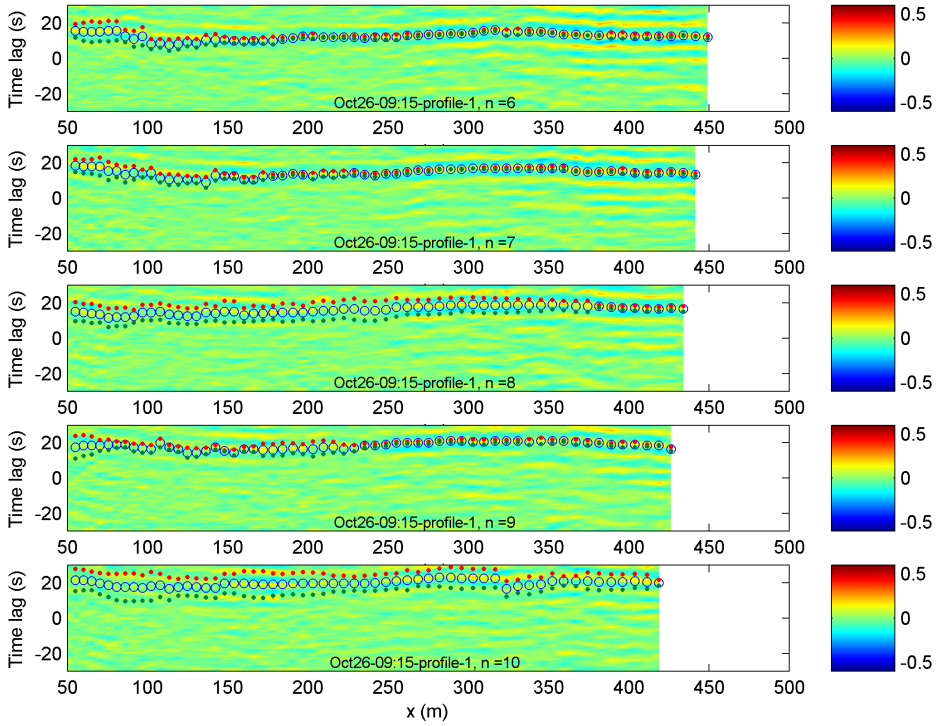

Figure 8-3 Correlation along the cross-shore array from x=50 to x=500 against time lag for pixel intensity time series from for n is one to five. The circles represent the estimated time lag corresponding to the maximum cross-correlation between pixel intensity time series. The red and dark green dots represent the standard deviation of the time lag.

References

Aarninkhof, S. G. J., Morelissen, R. and Cohen, A, B.. 2005. The Argus Runtime Environment, guidelines on installation and use. *manualArgusTools2005.doc*, Version dd. 15-09-05.

Capon, J., 1969. High-resolution frequency-wavenumber spectrum analysis. *Proceedings of the IEEE*, 57, 1408-1418.

Cohen, A. B., Van Dongeren, A., Aarninkhof, S. G. J., Roelvink, J. A. and Wijnberg, K. M., 2006. Nowcasting of coastal evolution through assimilation of remote observations and morphological model. *Poster at AGU Ocean Sciences meeting*, Honolulu (HI), USA.

Herbers, T. H. C., Elgar, S. and Guza, R. T., in press. Infragravity-frequency (0.005-0.05 Hz) motions on the shelf, Part I: Local nonlinear forcing by surface waves. *Journal of Physical Oceanography*.

Holland, K. T., Holman, R. A., Lippmann, T. C. , Stanley, J. and Plant, N., 1997. Practical use of video imagery in nearshore oceanographic field studies. *Journal of Oceanic Engineering* 22, pp. 81-92.

Holman, R. A. and Chickadel, C. C., 2004. Optical remote sensing of the incident wave angle field during NCEX. *Proc. ICCE 2004*, Lisbon.

Holman, R. A., Sallenger, A. H. J., Lippmann, T. C. and Haines, J. W., 1993. The application of video image processing to the study of nearshore processes. *Oceanograpy 6*, 78-85

Holman, R. A., Stanley, J., and Özkan-Haller, T. H., 2003. Applying video sensor networks to nearshore environmental monitoring. *IEEE Pervasive Computing*, 2 (4), 14-21.

Huang, N. E. and Tung, C. C., 1977. The influence of the directional energy distribution on the nonlinear dispersion relation in a random gravity wave field. *Journal of geophysical oceanography 7*, 403-414.

Krogstad., H. E., Lygre, A., 1986. Maximum entropy estimation of the directional distribution in ocean wave spectra. *Journal of physical oceanography*, v. 16, 2052-2060.

Kuik, A. J., Van Vledder, G. Ph., Holthuijsen., L. H., 1988. A method for the routine analysis of pitch-and-roll buoy wave data, *Journal of physical oceanography*, vol. 18, 1020-1033.

Lippmann, T. C., and Holman, R. A., 1991. Phase speed and angle of breaking waves measured with video techniques,.*Proc. Coastal Sediments '91*, New York: ASCE, pp. 542-556.

Longuet-Higgins, M. S., Cartwright, D. E. and Smith, N. D., 1963. Observations of the directional spectrum of sea waves using the motions of a floating buoy. *Ocean Wave Spectra*, proceedings of a conference, Easton, Maryland, pp. 111–136, National Academy of Sciences, Prentice-Hall.

Lynch, D. K. and Livingston, W., 1995. Color and light in nature. *Cambridge Univ. Press*, New York.

Pawka, S, 1983. Island shadows in wave directional spectra. *Journal of Geophysical Research*, 88 (C4), 2579-2591.

Philips, O. M., 1981. The dispersion of short wavelets in the presence of a dominant long wave. *Journal of Fluid Mechanics 107*, 465-485.

Plant, W. J. and Wright., J. W., 1980. Phase speeds of upwind and downwind travelling short gravity waves. *Journal of geophysics*, REs. 85 (C6), 3304-3310.

Stanley, J., Holman, R. A., 2005. Argus pixel toolbox. Coastal imaging lab, Oregon state university.

Stockdon, H. F., and Holman, R. A., 2000. Wave phase speed and nearshore bathymetry. *Journal of geophysical research*, vol. 105 (C9), 22015-22033.

Van Rijn, L. C., Ruessink, B. G., and Mulder, J. P. M., 2002. Coast3D – Egmond; The behaviour of a straight sandy coast on the time scale of storms and seasons. *EC MAST Project* No. MAS3-CT97-0086.